Development of Direct Internal Reforming Solid Oxide Fuel Cell Model and its Applications for Biomass Power Generation

Suranat WONGCHANAPAI

2013

Acknowledgements

First of all, the author would like to express his sincere gratitude and thanks to his supervisor, Professor Yoshida from Kyoto University, who continuously dedicates his time to help and guide him throughout the time he has been in this laboratory.

Secondly, the author would like to convey his deep appreciation to Associate Professor Iwai from Kyoto University, who always contributes and shares his valuable opinions and suggestions about the research to the author. Without him, this dissertation would not have been completed.

A special thanks to Professor Myoung-Hwan Kim from Korea Maritime University for his valuable guidance during the author's first year in the doctoral program.

In particular, the author wishes to thank Mr. Saito, Assistant professor, whom the author learned not only the academics and experiments from, but also an aspect of life in Japan as well as the Japanese language. Special thanks to Mr. Konno and Mr. Kishimoto who have guided the author throughout his year in this laboratory.

Finally, the author wishes to thank his parents Nuch and Tassana Wongchanapai, and his sister Passapoonsri for providing him with the foundation for all his achievements.

Contents

List of tables

List of figures

Chapter 1
Introduction

1.1 Background

Electricity generation through to a sustainable and renewable source of energy is a term becoming increasing prevalent in the energy industry. “Sustainable Energy” means providing for our energy needs without depleting our planet’s natural resources, while “Renewable Energy” means being able to generate energy with resources that are naturally regenerated. So, these two different terms may have a slightly different focus, but in the end they point to the same or similar energy sources. Among sustainable and renewable energies, biomass offers world-wide the largest exploitation potential. Biomass is derived from the carbonaceous materials of various human and natural activities or from byproducts we dispose of every day. Biomass compositions generally are carbon, hydrogen and oxygen. Nitrogen and small quantities of other atoms, including alkali, alkaline earth and heavy metals can also be found. Regardless of biomass materials, biomass utilizing technologies help people living in rural and remote areas become more energy independent. Nevertheless, the advantage of biomass energy in terms of greenhouse gas emissions is that the carbon dioxide that is emitted is almost entirely balanced by the carbon dioxide captured in its own growth.

Biomass is very versatile and completely renewable. It can be converted into biofuels, chemical products and power production. Biomass resource is available locally or even clustered in specific regions, which can be economically transported only within moderate distances to the conversion facilities. Therefore, distributed power generation system is an appropriate choice for end-use application of biomass fuel. The system can provide distributed power generation in areas with locally produced biomass resources. Although biomass accounted for nearly half of all energy consumed from renewable resources [1], most of the use of biomass is in a primitive and inefficient manner leading to adverse condition to human health and environment. Currently, most of the biomass

plants typically rely on conventional technologies such as boiler and steam turbine technology [2]. As a result, such systems tend to have a fairly low overall efficiency owing to the lower heating value of the biomass feedstocks. Therefore, the utilization of biomass in a clean and efficient manner must be studied and introduced for truly sustainable power generation.

Unlike fossil fuel, woody biomass resources, the largest and most economically available biomass source, naturally contain low sulfur content and therefore emit a small amount of sulfur dioxide when combusted. In addition, with this merit, biomass usually allowed to react in the presence of most catalyst without sulfur poisoning problems [3]. Under gasification, a thermo-chemical process, carbon bonds in woody biomass are broken and syngas (synthetic gas) is produced. Furthermore, biomass gasifiers have the potential to be up to twice as efficient as burning biomass in boilers to generate electricity. An alternative method of using biomass for power production is to convert biomass into biogas. Biogas, gaseous fuel, typically refers to a gas produced by anaerobic digestion of organic waste such as manure, sewage, municipal waste, green waste, plant material. Both syngas and biogas are generally used as fuel in conventional heat engines either gas engine or gas turbine. As potential substitutes for heat engines, fuel cells have recently received increased attention in power generation, as they are not subjected to carnot limitation.

Fuel cells are electrochemical conversion devices in which electricity is directly produced by a chemical reaction of fuel and oxidant. As long as the fuel and oxidant are supplied, electricity can be continuously generated. There are various types of fuel cells classified in terms of the materials of electrolyte used in the cells and include Proton Exchange membrane (Polymer) Electrolyte Fuel Cells (PAFCs), Molten Carbonate Fuel Cells (MCFCs), and Solid Oxide Fuel Cells (SOFCs). Depending on the type of electrolyte, operating temperature varies and fuel used is different.

Among fuel cells, high temperature SOFC technology is the most suitable candidate for biomass power conversion owing to its high electricity conversion efficiency, fuel flexibility, tolerance to fuel contaminants, low cost ceramic materials, and its operating temperature close to that in biomass gasification process. The most common SOFC configurations are tubular and planar cells. It is generally accepted that tubular has the advantage in sealing. However, the planar design is superior in terms of efficiency [4] and manufacturing points of view.

In addition, one of the attracting features of SOFC is the direct internal reforming (DIR) of hydrocarbon fuels. The endothermic reforming reaction proceeds on the Ni catalyst in the anode in the direct internal reforming process. It utilizes the waste heat generated by the electrochemical reaction and other irreversible processes to offset the heat requirements of the reforming reaction, resulting in the increase in the performance of the SOFC. It also reduces the amount of the extra air supplied to the cathode channel because the cooling demand is reduced, thus lowering the cost. One drawback is that it may cause excessive temperature gradients to the cell because of the strong endothermic nature of the reforming reaction. However, direct measurements of the temperature distribution in an operating DIR-SOFC are difficult because of the high temperature, narrow channel gaps, and small flow rates. Numerical simulation has become an effective tool to understand the phenomena in a DIR-SOFC system.

Biomass fuelled integrated SOFC system is one of the key energy technologies of the future since it combines the merits of renewable energy sources and highly efficient energy conversion technologies. SOFC operation on biomass-derived syngas has been successfully demonstrated in several experimental studies [5-8] As well as, the feasibility of internal reforming SOFC running on biogas is demonstrated for different SOFC configurations and materials by several experimental studies [9-14]. Also, SOFC based power systems offer excellent power conversion efficiency regardless of the sizes [15]. In this regard, SOFC technology is very attractive for the distributed power generation where units can be configured to meet a particular local power generation demand.

Recently, with improved sealing materials and sealing concepts, small-scale 1-25kW size planar SOFC stacks have been successfully developed by various organizations. In this scale of electricity generation, SOFCs produce the highest electrical efficiency compared to other energy conversion devices. In such small-scale SOFC based system, exhaust fuel and heat of SOFC can be effectively utilized for endothermic gasification process to enhance system performance. This makes an integrated small-scale SOFC-biomass gasification power generation system a promising candidate for residential applications.

Along with the development of SOFC technology, in order to keep pace with rising distributed energy demand with high efficiency potential while also minimizing environmental impact, integration of an SOFC with a gas turbine (GT) for power

generation systems have received increased attention in the past decade. There are SOFC-GT plants from tens to hundreds kW_e output demonstrated experimentally in [16-21], making conceptual SOFC-GT hybrid systems practically feasible. Since biogas is being increasingly regarded as potential renewable energy source for distributed power generation, biogas-fed SOFC-GT system appears as one of the most promising alternatives for distributed power generation. Moreover, extending this hybrid system to combined heat and power (CHP) generation provides heat recovery from exhaust resulting high overall efficiency.

1.2 Scope of the Present Study

In this study, we develop a numerical model of an anode-supported planer DIR-SOFC to clarify suitable operating parameters for co- and counter-flow operations considering both the performance and material constraints. A comparative performance study between co- and counter-flow planar anode-supported DIR-SOFCs is performed under constant fuel and air utilization factors with the distribution of the temperatures, species concentrations, current density, and polarization losses. Since changing inlet temperatures can have either a beneficial or an undesirable impact on efficiency and life span of the cell, effects of the current density and inlet temperatures under co- and counter-flow operations are investigated by energy and exergy methods to clarify the maximum cell performance with lowest risk of thermal failure.

The developed SOFC is further used to determine the optimum performance of an integrated small-scale SOFC-biomass gasification power generation system for safe and efficient system operations as well as economic solution. In this study, the integration of a biomass gasification and 5kW-class SOFC power system is evaluated through numerical simulation. The biomass fuel considered in this work is represented by ash-free typical wood fuel formula of $CH_{1.4}O_{0.59}N_{0.0017}$ [22]. A sensitivity analysis was carried out to achieve a better understanding of the influence of key parameters e.g. steam to biomass ratio (STBR), SOFC inlet stream temperatures, fuel utilization factor (U_f) and anode off-gas recycle ratio (AGR) on the performance of key system components. By performing energy and exergy analysis, the causes of exergy losses were revealed to identify the areas of improvement of the combined system. Since SOFC stack is accounted for the most expensive part of the initial investment cost, the number of cells required for SOFC stack is also taken into consideration as well.

This study also presents sensitivity analysis preformed to develop the understanding of the influence of key operating parameters of the direct-biogas SOFC-micro gas turbine (MGT) hybrid CHP system with an electrical power output of 200 kW_e through numerical simulation. By performing energy and exergy analysis, the causes of exergy losses were revealed to identify the areas of improvement of the combined system while adhering to material thermal constraints. The attention was paid to the influence of air-steam mixtures as reforming agents to the direct internally reformed SOFC stack as well as to the SOFC-MGT hybrid CHP plant. The other key operating parameters considered in this study are fuel utilization factor (U_f), turbine inlet temperature (TIT) and compression ratio. The influence of variations in operating parameters on the plant performance are evaluated through not only the overall system and SOFC efficiencies but also the thermal energy to electric power ratio (TER) and the power ratio between MGT and SOFC (P_{MGT}/P_{SOFC}). Due to the fact that SOFC stack is accounted for the most expensive part of the initial investment cost, the required number of cells for SOFC stack is also taken into consideration as well.

Chapter 2
Literature Review

2.1 Biomass Materials

The term “biomass” refers to organic matter that has stored energy through the process of photosynthesis. It exists in one form as plants and may be transferred through the food chain to animals’ bodies and their wastes, all of which can be converted for everyday human use through processes such as combustion, which releases the carbon dioxide stored in the plant material. Many of the biomass fuels used today come in the form of wood products, dried vegetation, crop residues, and aquatic plants. Biomass has become one of the most commonly used renewable sources of energy in the last two decades, second only to hydropower in the generation of electricity. It is such a widely utilized source of energy, probably due to its low cost and indigenous nature, that it accounts for almost 15% of the world’s total energy supply and as much as 35% in developing countries, mostly for cooking and heating.

Biomass is defined as all materials that are derived, directly or indirectly, from contemporary photosynthesis reactions illustrated in Fig. 2-1. Photosynthesis is a process used by plants and other organisms to convert the light energy captured from the sun into chemical energy in the form of glucose ($C_6H_{12}O_6$). Biomass includes all vegetal matter and their derivatives (see in Fig. 2-2): wood, garbage, waste, landfill gases, and alcohol fuels. Biomass is considered a renewable energy source as long as it is based on sustainable utilization. If consumed at the same rate as new biomass is grown, there is no net atmospheric CO_2 emission connected to the consumption of biomass materials. Compared to fossil fuels, biomass is more evenly dispersed over the earth’s surface and is thus suitable for distributed local energy production. Energy production from biomass is also in general regarded cleaner than fossil fuels in terms of environmental pollution [23-24]. In addition, some biomass materials, typically waste materials and non-woody biomass materials may contain significant amounts of heavy

metals, sulphur and chlorine. During combustion or gasifiication these species may follow the gas stream or end up in the ash fraction. Thus, if the biomass conversion technology is not carefully designed, the energy production may cause significant emissions of pollutants and toxic species. A detailed knowledge of the composition of the raw biomass material is therefore needed. In addition, it is important to know where the different species end up during the thermal processing, i.e. in which stream fraction (e.g. gas stream, bottom ash, fly ash, deposition). Furthermore, the speciation may be important for end-use applications, e.g. fuel cells.

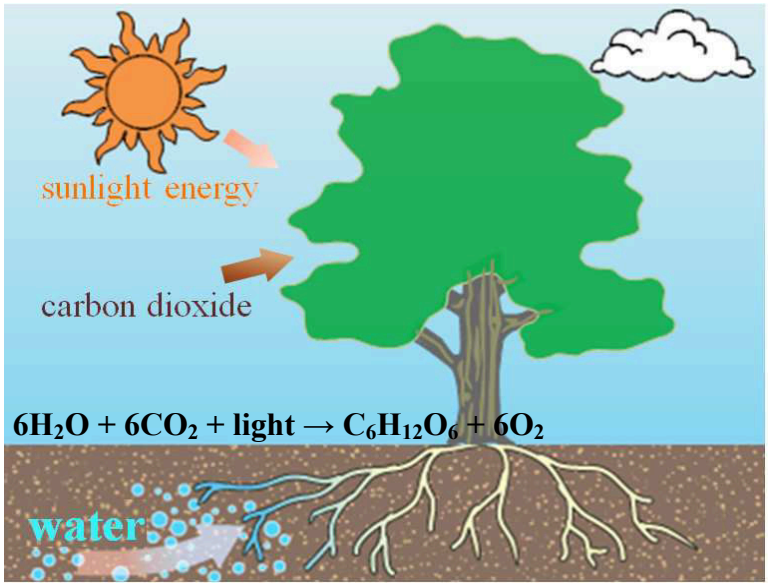

Fig. 2-1: Photosynthesis.

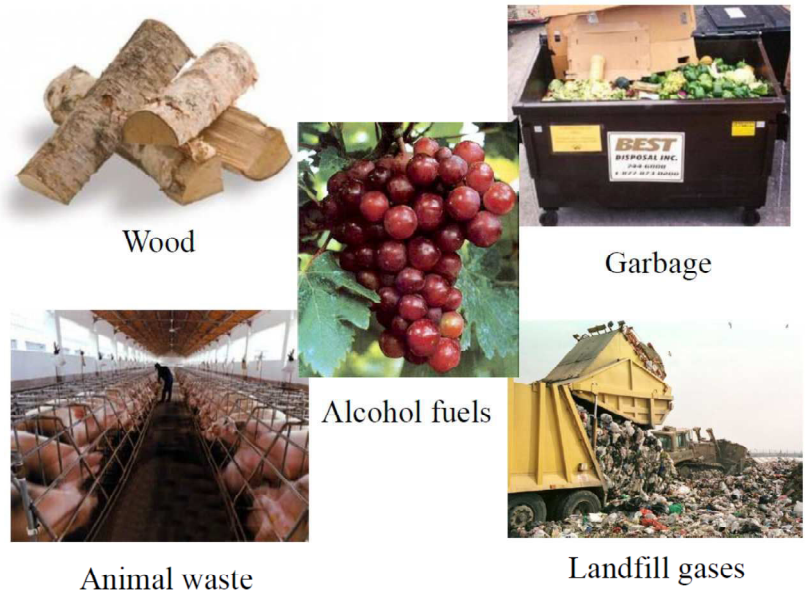

Fig. 2-2: Biomass sources.

2.2 Biomass Conversion Techniques

Energy is stored in biomass materials as chemical energy. To be able to utilize this energy, a conversion technique must be applied. By direct combustion, the chemical energy is converted to heat. This heat can be used for heating purposes or for power production in e.g. a steam turbine. It is also possible to convert biomass materials to gases, liquids or carbon rich solids which can be used for heat and power production in a subsequent process such as combustion engines, gas turbines or fuel cells. Thus, there are several possibilities for production of heat, electrical power or a combination of the two from biomass materials. There are three different types of conversion techniques:

1. Biochemical conversion
2. Physical/chemical conversion
3. Thermochemical conversion

The biochemical conversion method comprises anaerobic digestion to produce methane-enriched gas and fermentation to produce ethanol. Physical conversions include mechanical extraction which is normally connected to the production of bio-diesel. These methods are not in the scope of this work and will therefore not be further presented here. The focus here is on the thermochemical conversion technique, especially gasification. In the following these are briefly presented.

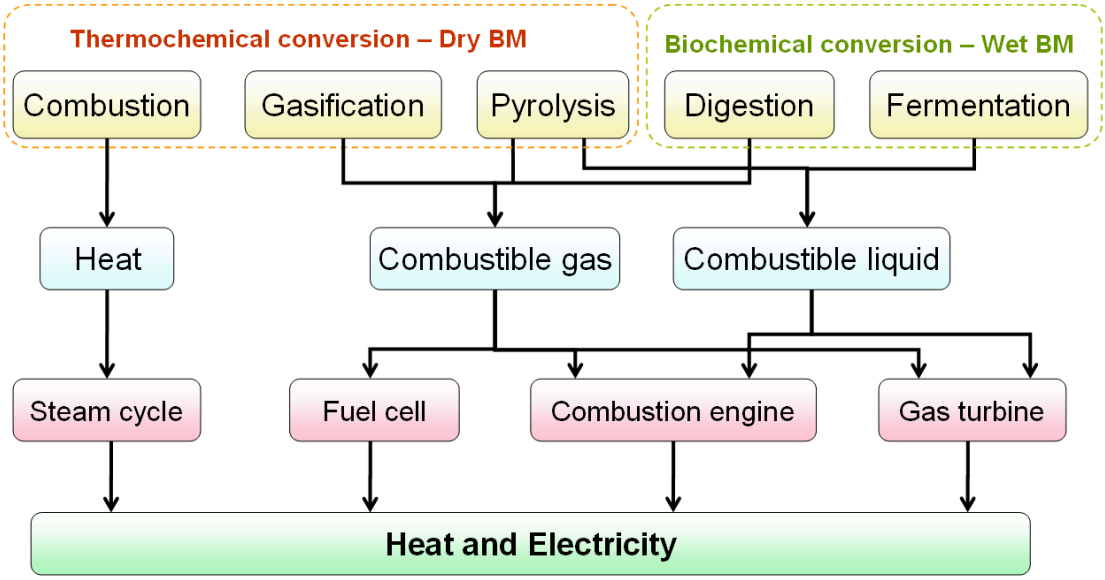

Fig. 2-3: Ways from biomass to electricity.

2.2.1 Combustion

The use of biomass for energy offers considerable flexibility of fuel supply. Biomass may be utilized directly by combustion or converted to a wide range of solid, liquid, and gaseous fuels, some of which may be used as substitutes for fossil fuels.

Combustion can ideally be defined as a complete oxidation of the fuel. The combustion process produces hot gases at temperature around 1073–1273K. Thus, the chemical energy stored in the biomass may be converted into heat for direct heating purposes or mechanical energy in various process equipment e.g. stoves, furnaces, boilers, stirling engines and steam turbines. However, biomass combustion may produce significant emissions of components caused by incomplete combustion (CO, UHC(unburned hydrocarbons), particles/tars, dioxins) and NO_x components. Consequently, if the biomass combustion is not carefully designed, it can pose severe epidemiological consequences to human health.

2.2.2 Pyrolysis

Pyrolysis can be defined as thermal degradation in the absence of an externally supplied oxidizing agent. The pyrolysis products are mainly tar and carbonaceous charcoal, and low molecular weight gases. In addition, CO and CO_2 can be formed in considerable quantities, especially from oxygen-rich fuels, such as biomass. Fuel type, temperature, pressure, heating rate and reaction time are all variables that affect the amounts and properties of the products formed.

However, a low devolatilization rate can be observed in the temperature range of 673–773K. This is caused by lignin decomposition, which occurs throughout the whole temperature range, but the main area of weight loss occurs at higher temperatures. This means that the lignin is mainly responsible for the flat tailing section that can be observed for all the wood species at higher temperatures. In addition, birch, having the highest hemicellulose and lowest lignin content, yields the lowest char residue. The pyrolysis products can be used in a variety of ways. The char can be upgraded to activated carbon, used in the metallurgical industry, as domestic cooking fuel or for barbecuing. Pyrolysis gas can be used for heat production or power generation, or synthesized to produce methanol or ammonia. The tarry liquid, pyrolysis oil or bio-oil can be upgraded to high-grade hydrocarbon liquid fuel for combustion engines (e.g.

transportation), or used directly for electricity production or heating purposes.

2.2.3 Gasification

Biomass gasification is a thermochemical conversion process in the presence of an externally supplied oxidizing agent where fuel is converted into a gas mixture called synthetic gas or "syngas", mainly consisting of carbon monoxide, carbon dioxide, hydrogen, methane, water vapor, nitrogen, but also contaminants. The composition of the product gas depends mainly on the fuel, gasifier type, and gasification agent.

Woody biomass such as residues from forestry operations or herbaceous biomass typically has moisture content ranging from 15% to over 60% at the point of harvest. Higher levels of moisture in the feedstock cause more energy requirement for evaporation in the gasifiers, hence the reaction temperature decreases, which results in poorer product gas with higher levels of tar. Due to this fact, forced drying of the biomass in general becomes necessary in such systems; which can represent the highest capital cost in the pretreatment section. In these driers, the medium needed to dry the solid may be selected as pure vapor or a mixture of vapor and non-condensable gas or combustion products [25].

Air, oxygen, steam or a combination of these may be used as gasification agents. Partial oxidation with air yields high N_2 content in the product gas (i.e. ~50%). For this case, the heating value of gas is around 5 MJ/m^3. In the case of partial oxidation with oxygen, heating value of gas around 11 MJ/m^3 without any significant N_2 content achieved. However, providing and using oxygen is costly. On the other hand, gasification with steam gives higher heating value of gas around 17 MJ/m^3, but at the expense of lower overall efficiency [25].

There are various gasifier types for different purposes with each of them having advantages and disadvantages, which are listed in Table 2-1. A survey has revealed the percentage of the commercially offered gasifiers as follows [26]: 75% downdraft, 20% fluid bed (including circulating fluid bed), 2.5% updraft, and 2.5% other types. According to Brigwater [26], the following selection may be done according to the scale of the application: downdraft-fixed bed for small scale, bubbling fluidized bed for medium scale, and circulating fluidized bed for large scale.

Table 2-1: Advantages and disadvantages of main biomass gasification reactor types.

Reactor type	*Advantages*	*Disadvantages*
Downdraft-fixed bed	Very simple and robust Low particulates and tar High exit gas temperature Moderate cost	Lower moisture level tolerability Scale-up limitations Feed size limitations
Updraft-fixed bed	Simple and reliable Higher moisture level tolerability Low cost High thermal efficiency and carbon conversion	Very dirty product gas with high levels of tars Scale-up limitations Intolerant to high portions of fines in feed Low exit gas temperature
Bubbling fluid bed	Good temperature control Good scale-up potential Greater tolerance to particle size range Large scale applications	High particulates and moderate tar Limited turn-down capability Some carbon loss with ash Higher particle loading
Circulating fluid bed	Good temperature control Good scale-up potential Greater tolerance to particle size range Large scale applications	High cost at low capacity High particulates and moderate tar Higher particle loading Difficulties with in-bed catalytic processing
Entrained flow	Simple design Good scale-up potential Potential for low tar	Costly feed preparation Carbon loss with ash Limitations with particle size
Twin fluid bed	Good temperature control Greater tolerance to particle size range Large scale applications	High tar levels Difficult to scale-up High cost

Taken from [26-27].

2.2.4 Anaerobic Digestion

Anaerobic digestion is a series of processes in which microorganisms break down biodegradable material in the absence of oxygen. It is used for industrial or domestic purposes to manage waste and/or to release energy. In the absence of oxygen, organic matter such as animal manures, organic wastes and green energy crops (e.g. grass) can be converted by anaerobic digestion process into biogas (a 50%-75% methane-enriched gas with CO_2 and small amount of hydrogen sulphide and ammonia). Anaerobic digestion is also the basic process for landfill gas production from municipal green waste. The composition of biogas varies depending upon the origin of the anaerobic digestion process (see in Table 2-2). It has significantly potential, but it is characterized by relatively small plant size. Anaerobic digestion is increasingly used in small-size, rural and of grid applications at the domestic and farm-scale. In modern landfills, methane production ranges between 50 to 100 kg per tone of municipal solid waste (MSW). Nevertheless, the product gas from anaerobic digestion of biomass needs extensive gas cleanup process due to high levels of contaminants in the gas.

Table 2-2: Approximate Biogas Composition in Anaerobic Digestion.

Typical Biogas	
Composition	vol%
CH_4	50-75
CO_2	25-50
H_2S	0-3
H_2	0-1
O_2	0-2
N_2	1-10

2.3 Gas Cleaning System

The basic cleanup system design strategy should be based on required cleanliness goals (determined by the application) and nature of the contaminants. If a biomass derived gas is to be used in a burner application, no cleanup will be needed. However, if the fuel gas will be fed to a fuel cell, the gas must be cleaned and conditioned before it is fed to the application.

The major impurities of biomass fuel produced during biomass conversion process such as gasification or anaerobic digestion are particulate, alkali compounds, tars, nitrogen and sulfur containing compounds [28]. Sulfur compounds such as hydrogen sulphide (H_2S) in fuel gas are undesirable as they can cause catalyst poisoning or degradation and pollutants in exhaust gases.

The primary types of system for particulate removal include cyclone filters, barrier filters, electrostatic filters, and wet scrubbers [28]. Cyclone filters also remove condensed tars and alkali material from the gas stream, although the vaporized forms of those constituent remain in the gas stream. Barrier filters include a range of porous material that allows gases to penetrate but prevent the passage of particulates. These filters efficiently remove small-diameter particulates in the range of 0.5 to 100 μm in diameter in gas streams. Barrier filters are effective for removing dry particulates but are less suitable for wet or sticky contaminants such as tars. In electrostatic filters, the product gas flows past high voltage electrodes that impart an electric charge to particulates, and then collected as the gas stream passes collector plates of the opposite polarity. The electrically charged particulates migrate to the collector plate and deposit on the surface. Particulates are removed from the scrubber plates by either wet or dry methods. Wet scrubbers use liquid sprays, usually water, to remove particulates. Most biomass gasification systems that currently use wet scrubbers do so primarily as a means to remove tars rather than particulates from the gas stream. Removing the particulates separately can prevent condensation of the sticky tars on the particulate surface, and that can prevent fouling and plugging of filter surface. The alkali will remain as a vapor in the gas until it condenses to form small particulates or can condense on surface such as other particulates or other system surface. Alkali vapor can be removed by cooling the hot product gas below 873 K to allow for condensation of the material into solid particulates and then physically be removed through filter. Alternatively, the use of alkali traps may be effective at removing alkali from hot gas stream. Method to remove tars from biomass derived gas fall into one of the three categories: physical removal, thermal conversion and catalytic destruction. Physical removal of tars is simply similar to the technologies used in particulates removal. Tar destruction can be accomplished with temperature above 1473 K or use catalysts at moderate temperature between 1023 and 1172 K [28]. In addition, the technology of sulfur removal is commercially available and has been used successfully in coal gasification process for decades.

2.4 Solid Oxide Fuel Cell (SOFC)

Fuel cells are inherently clean and efficient, providing solutions to the shortage of energy and environment degradation. There are various types of fuel cells in terms of the materials for electrolyte used in the cell e.g. Protron Exchange Membrane (Polymer) Electrolyte Fuel Cell (PEFC), Alkaline Fuel Cell (AFC), Phosphoric Acid Fuel Cell (PAFC), Molten Carbonate Fuel Cell (MCFC), and Solid Oxide Fuel Cell (SOFC). Depending on the type of electrolyte, operating temperature varies and fuel to be used is different. The AFC, PAFC and PEFC are low temperature fuel cells operating at 353 to 573 K where as MCFC and SOFC works at high temperature environment from 873 to 1273 K.

One of the major benefits of high-temperature fuel cells is their ability to use other fuels than hydrogen. This simplifies system design, because a heated reformer and hydrogen cleanup is avoided, but it also increases the overall electrical efficiency. The presence of methane in the fuel cell feed enables waste heat from the fuel cell to be upgraded to chemical energy via endothermic reforming of the fuel. SOFCs are potentially the most useful for stationary power generation in terms of their-high power density and their ability to operate with a variety of fuels. The opportunities for application of high and intermediate temperature SOFCs range from large scale distributed power generation to small-scale heat and power.

2.4.1 SOFC materials

The electrolyte of SOFC is a solid, nonporous ceramic, usually Y_2O_3-stabilized ZrO_2 (YSZ). The SOFC operates at 873 to 1273 K where the ceramic electrolyte becomes conductive to oxygen ions (O^{2-}) but nonconductive to electrons. In 1899, Nernst discovered the solid oxide electrolyte when using stabilized zirconia in making filaments for electric glowers [29]. Nernst is the first scientist describing zirconia (ZrO_2) as an oxygen ion conductor. Until lately, SOFCs have all been developed based on an electrolyte of zirconia stabilized with the addition of a small percentage of yttria (Y_2O_3). The range of the operating temperature of the SOFCs is the highest operating temperature range of all fuel cells, which presents both challenges for the construction of durable SOFC, and advantages. The high operating temperature permits rapid kinetics and allows production of high quality heat as by-product suitable for co-generation. SOFC cathodes are now made primarily from electronically conducting oxides or mixed electronically conducting and ion-conducting ceramics.

Nickel can be used as anode material since nickel metal plays the dual role of hydrogen oxidation catalyst and electric current conductor. Additionally, nickel is also an excellent catalyst for cracking of hydrocarbons, e.g. in situ reforming of methane. However, the thermal expansion of nickel is considerably higher than that of the yttria-stabilized zirconia (YSZ) conventionally used for the electrolyte. Another problem with nickel is that it can sinter at the cell operating temperature, causing decreasing porosity and reduction of the TPB [29]. While, strontium-doped lanthanum manganite (LSM) is the most widely used material for the cathode.

Composite electrodes made of a binary mixture of electronically and ionically conducting particles are more and more widely used in state-of-the-art SOFCs since they are superior to electrically conducting electrodes. Common composite electrodes are nickel/yttria stabilized zirconia (Ni/YSZ) and Sr-doped $LaMnO_3$/yttria stabilized zirconia (LSM/YSZ) for anode and cathode, respectively. The use of composite anode leads to the reduction of mismatching of the thermal expansion: the thermal expansion coefficient of YSZ is closer to that of Ni–YSZ mixture than to that of pure Ni [30]. This also allows better anode–electrolyte adhesion; prevention of nickel sintering: the presence of YSZ particles between Ni particles in the Ni–YSZ mixture prevents agglomeration of the metal particles. LSM is a poor ionic conductor and so the electrochemically active reaction is limited to the triple phase boundary (TPB). LSM operates well as cathode at high temperature and its performance rapidly drops as the temperature is below 1073 K. Nevertheless, these problems can be alleviated by using composite cathode of LSM/YSZ.

The interconnect transports electrons between the electrochemically active sites (TPBs) and the external circuit. In a typical SOFC, the interconnect is in direct contact with both the anode and cathode and both the fuel and air. There are two types of materials for state-of-the-art SOFC interconnects, namely ceramic and metallic, with different features. The ceramic lanthanum chromite is the most common material for SOFC interconnects working at high temperatures (1173–1273 K) since it is stable in oxidizing environments at the cathode. Metallic interconnects have a better electrical conductivity compared to ceramic ones, but are not stable in oxidizing conditions. Therefore, they are mainly suitable for lower temperatures [31]. Oxidation resistant alloys based on Cr or Ni are suitable for intermediate-high temperatures (1073–1173 K).

2.4.2 Principle of DIR-SOFC

In typical SOFC, the reforming step is done after the desulphurization using an external unit (see in Fig. 2-4). This type of design is known as external reforming (ER), and is convenient for large-scale stationary systems with combined heat and power generation.

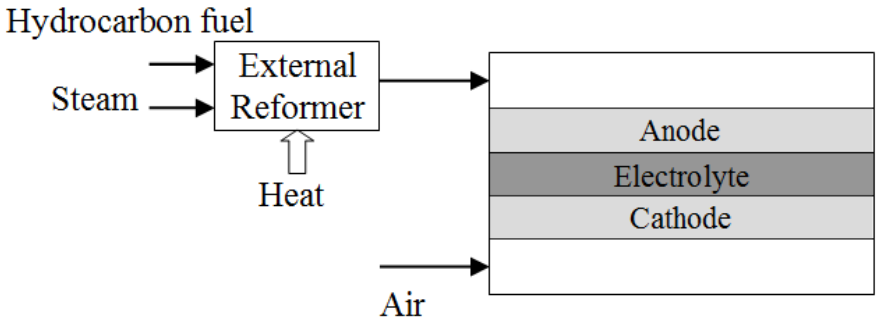

Fig. 2-4: Schematic of an ER-SOFC.

For small-scale application and particularly for portable systems, however, the complexity and size of the overall system can reduce by eliminating the external reformer and reforming the fuels inside the stack. This type of design is known as internal reforming and uses the waste heat generated by electrochemical oxidation and other non-reversible processes to offset the heat requirements of reforming reactions. Internal reforming SOFCs (IR-SOFCs) can be divided into two operating modes, i.e. indirect internal reforming (IIR) (see in Fig. 2-5) and direct internal reforming (DIR) (see in Fig. 2-6). With the advent of better DIR catalysts for high temperature operation of SOFC the DIR is almost universally adopted in successful fuel cell systems. The SOFC model in this study is based direct internal reforming type. Therefore, only direct internal reforming SOFC will be further described later in this section.

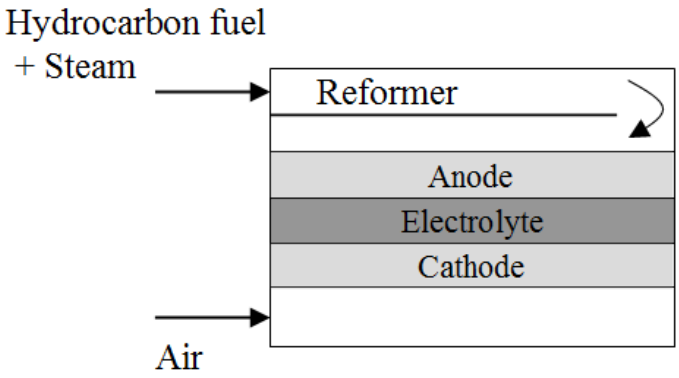

Fig. 2.5: Schematic of an IIR-SOFC.

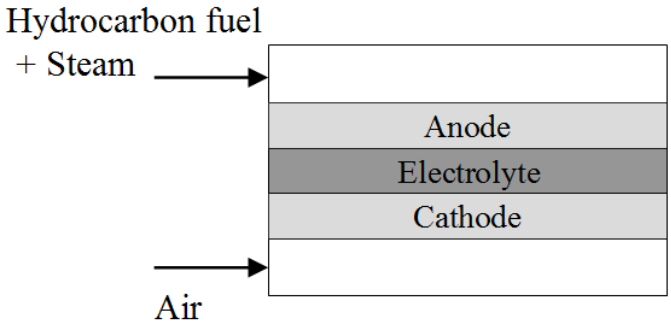

Fig. 2-6: Schematic of a DIR-SOFC.

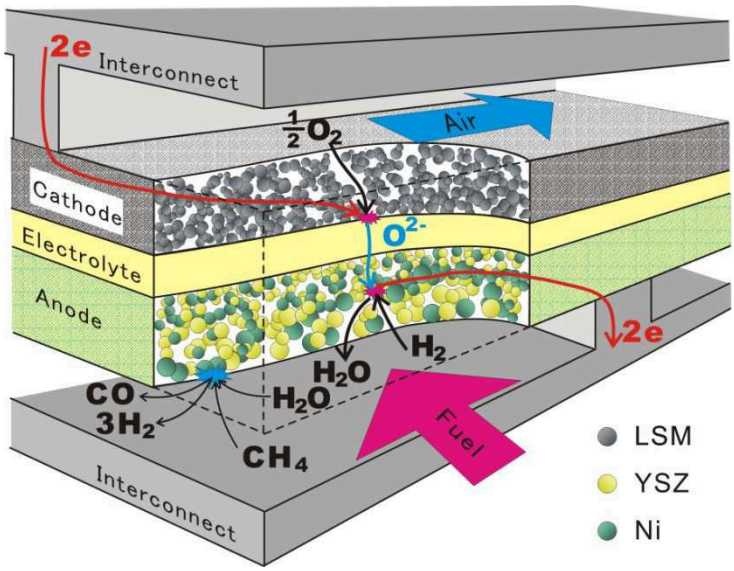

Fig. 2-7: Principles of electrical generation in DIR-SOFC.

There are numerous chemical reactions that should be taken into account that may occur in the fuel channel. For natural gas or syngas fueled SOFCs, usually the gas entering the anode channel is pre-reformed and usually is found that at least CH_4,H_2,CO,H_2O, and CO_2 are usually present. Figure 2-7 illustrates a cross-flow channel contains a layer of fuel gas, a layer of oxidant gas and a layer of anode-electrolyte-cathode (AEC) sandwiched by two interconnectors. The fuel and air flow in two mutually perpendicular directions, respectively. At the anode, the methane-steam gas is reformed inside to generate H_2 and CO for the electrochemical reactions. At the cathode, combining with electrons, O_2 decomposes into O^{2-}due to the function of the catalyst. When an O^{2-} passes through the electrolyte, it reacts with H_2 and CO to form H_2O and CO_2, respectively. The released electrons are output to drive the external load, and return to the cathode. The reforming and electrochemical reactions are given as follows.

Steam reforming reaction: $CH_4 + H_2O \leftrightarrow CO + 3H_2$ (2-7)

The stream reforming reaction is often assumed to have fast kinetics and modeled during local equilibrium assumption. It is also reported that at the present of Ni-based catalyst in 1173K environment, the steam reforming reaction of methane proceeds as fast as 42 times faster than that of electrochemical reaction of hydrogen [32].

Water-gas shift reaction: $CO + H_2O \leftrightarrow CO_2 + H_2$ (2-8)

In the present of CO and steam, the water-gas shift reaction becomes very important in controlling the concentration of hydrogen in the reaction sites.

Electrochemical reactions

Oxygen is reduced at the three-phase boundaries in the cathode catalyst layer generating oxygen ions.

Cathode :

Oxygen : $\frac{1}{2}O_2 + e^- \rightarrow O^{2-}$ (2-9)

When the hydrogen and carbon monoxide generated by the reforming process participate in the electrochemical reactions in the SOFC are reacted with oxygen ions generated by the reduction reaction of oxygen.

Anode :

Hydrogen : $H_2 + O^{2-} \rightarrow H_2O + 2e^-$ (2-10)

Carbon monoxide : $CO + O^{2-} \rightarrow CO_2 + 2e^-$ (2-11)

2.5 Energy and Exergy Concept

Exergy is defined as the maximum amount of work which can be obtained from a system or a flow of matter when it is brought reversibly to equilibrium with the reference environment. To further explain this point, Table 2-3 illustrates the difference between energy and exergy. Exergy analysis is based on second law of thermodynamics

and the concept of irreversible entropy production. The exergy consumption during a process is proportional to the entropy production due to irreversibility. It is a useful tool for furthering the goal of more efficient energy use, as it enables the determination of the location, type and true magnitude of energy wastes and losses in a system. In the exergy analysis, three forms of exergy transfer are usually considered, i.e., exergy transfer with work interaction, heat interaction and mass interaction. Other forms of exergy transfer include friction, momentum, potential interaction, etc. Moreover, in conducting exergy analysis, two forms of equilibrium are considered, the environmental state (restricted dead state) and the dead (unrestricted) state. The environmental state is a restricted equilibrium where the conditions of mechanical (P) and thermal (T) are satisfied. The dead state is an unrestricted equilibrium where the conditions of mechanical (P), thermal (T) and chemical potential (μ) are satisfied.

Table 2-3: Comparison of energy and exergy.

Energy	**Exergy**
Dependent on properties of only a matter or energy flow, and independent of environment properties	Dependent on properties of both a matter or energy flow and the environment
Has values different from zero when in equilibrium with the environment (including being equal to mc^2 in accordance with Einstein's equation)	Equal to zero when in the dead state by virtue of being in complete equilibrium with the environment
Conserved for all processes, based on the first law of thermodynamics	Conserved for reversible processes and not conserved for real processes (where it is partly or completely destroyed due to irreversibilities), based on the second law of thermodynamics
Can be neither destroyed nor produced	Can be neither destroyed nor produced in a reversible process, but is always destroyed (consumed) in an irreversible process
Appears in many forms (e.g., kinetic energy, potential energy, work, heat) and is measured in that form	Appears in many forms (e.g., kinetic exergy, potential exergy, work, thermal exergy), and is measured on the basis of work or ability to produce work
A measure of quantity only	A measure of quantity and quality

2.5.1 Control-Volume Analysis

Consider the steady-state control volume shown in Fig. 2-8 Each species of the fluid enters the control volume with properties such as temperature (T), pressure (P), partial enthalpy (h_i), partial entropy (s_i), chemical potentials (μ_i) and leaves at the environment state (T_0, P_0, $h_{i,00}$, $s_{i,00}$, $\mu_{i,00}$).

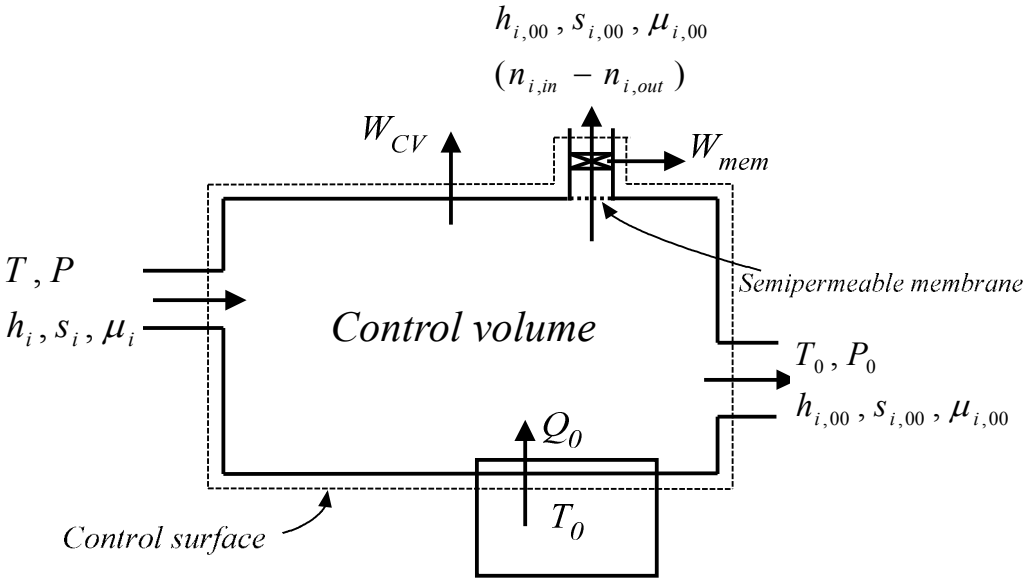

Fig. 2-8: Scheme diagram for work potential of the process.

The energy equation for the control volume in Fig. 2-8 is described as follows:

$$Q_0 + W = \sum_i (n_i h_i)_{out} - \sum_i (n_i h_i)_{in} + \sum_i (n_{i,in} - n_{i,out}) h_{i,00} \qquad (2\text{-}12)$$

The entropy balance in terms of partial molar entropy value s_i under reversible conditions is

$$\sum_i (n_i s_i)_{out} - \sum_i (n_i s_i)_{in} + \sum_i (n_{i,in} - n_{i,out}) s_{i,00} - \frac{Q_0}{T_0} = 0 \qquad (2\text{-}13)$$

By eliminating Q_0 between the two equations, rearranging, and recognizing that $h_{i,00} - T_0 s_{i,00} \equiv g_{i,00} = \mu_{i,00}$, we find that

$$W_{rev} = \sum_i n_i (h_i - T_0 s_{i,} - \mu_{i,00})_{out} - \sum_i n_i (h_i - T_0 s_{i,} - \mu_{i,00})_{in} \qquad (2\text{-}14)$$

The stream availability of a fluid, Ex_{total}, is defined as the maximum work output which can be obtained as the fluid is changed reversibly from the given state to a dead state

($h_{i,0}$, $s_{i,0}$, $\mu_{i,0}$). Hence Ex_{total} is defined by the negative of W_{rev}.

$$Ex_{total} = n_{total}\left(ex_{ph} + ex_{ch}\right) \tag{2-15}$$

$$ex_{ph} = \sum_i x_i\left[\left(h_i - h_{i,0}\right) - T_0\left(s_i - s_{i,0}\right)\right] \tag{2-16}$$

$$ex_{ch} \equiv \sum_i x_i\left(\mu_{i,0} - \mu_{i,00}\right) \tag{2-17}$$

2.5.2 Exergy Transfer associated with material streams

Physical exergy

Physical exergy is the work obtainable by taking the substance through reversible processes from its initial state temperature T and pressure P, to the state determined by the temperature T_0 and the pressure P_0 of the environment. It can be calculated with

$$Ex_{ph} = \sum_i n_i\left[\left(h_i - h_{i,0}\right) - T_0\left(s_i - s_{i,0}\right)\right] \tag{2-18}$$

where h is the specific enthalpy and s the specific entropy.

In all the range of temperature and pressure considered, the Dalton's law (ideal mixtures) is adopted. For all the substances, a temperature-dependent specific heat model is adopted:

$$c_{p,i} = R(a + bT + cT^2 + dT^3 + eT^4) \tag{2-19}$$

The coefficients of Eq.(2-19) are presented in Table 2-4.

Table 2-4: Specific heat capacity constants.

Specific heat capacity constants					
	a	$b\times10^3$	$c\times10^6$	$d\times10^9$	$e\times10^{12}$
H_2O	4.070	-1.108	4.152	-2.964	0.807
CO	3.710	-1.619	3.692	-2.032	0.240
H_2	3.057	2.677	-5.81	5.521	-1.812
O_2	3.626	-1.878	7.056	-6.764	2.156
N_2	3.675	-1.208	2.324	-0.632	-0.226
CO_2	2.401	8.735	-6.607	2.002	0.000
CH_4	3.826	-3.979	24.558	-22.733	6.963

Chemical exergy

Chemical exergy is equal to the maximum amount of work obtainable when the substance under consideration is brought from the environmental state (see in Table 2-5), defined by the parameters T_0 and P_0, to the reference state by processes involving heat transfer and exchange of substances only with the environment. The chemical exergy for mixtures can be calculated as follows:

$$Ex_{ch} = \left(\sum_i n_i\right)(\mu_0 - \mu_{00}) = \left(\sum_i n_i\right)\left(\sum_i x_i ex_{ch,i} + R \cdot T_0 \sum_i x_i \ln(x_i)\right) \quad (2\text{-}20)$$

where x_i represents the molar fraction of gas species i and R is the universal gas constant.

By considering environmental state in Table 2-5, as ideal gas mixture, chemical exergy can be calculated as listed in Table 2-6.

Table 2-5: A reference-environment model.

Temperature	T_0 = 298.15 K
Pressure	P_0 = 1 atm
Composition	Atmospheric air saturated with H_2O at T_0 and P_0 having the following composition:

Air constituents	Molar fraction ($x_{i,00}$)
N_2	0.7567
O_2	0.2035
Ar	0.0303
CO_2	0.0091
H_2O	0.0003
H_2	0.0001

Taken from [33].

Table 2-6: Base chemical exergy values of selected species.

Species	Specific chemical exergy ($\mu_{t,0} - \mu_{t,00}$) (kJ mol^{-1})
Carbon (graphite) (C)	410.535
Carbon dioxide (CO_2)	$2.478907 \ln x + 20.108$
Carbon monoxide (CO)	$2.478907 \ln x + 275.224$
Hydrogen (H_2)	$2.478907 \ln x + 235.153$
Methane (CH_4)	$2.478907 \ln x + 830.212$
Nitrogen (N_2)	$2.478907 \ln x + 0.693$
Oxygen (O_2)	$2.478907 \ln x + 3.948$
Water (H_2O)	$2.478907 \ln x + 8.595$
Water (H_2O) (*liquid*)	0.045

Taken from [33].

Chapter 3
Numerical modeling

3.1 DIR-SOFC model

The fuel cell mathematical model discusses here the thermodynamic aspect and the associated electrochemical processes of the cell operation. A planar SOFC consists of two electrodes sandwiched around a hard ceramic electrolyte such as Zirconia. Hydrogen and carbon monoxide is the fuel gas fed into the anode of the fuel cell and oxygen enters the cell through the cathode. The electrode surface will allow oxygen ions to leave the electrolyte and react with the fuel, which when oxidized releases electrons (e^-). The reaction of the oxygen ion with the fuel creates an oxygen concentration gradient across the electrolyte, which attracts oxygen ions from the airside, or cathode, to fuel side, or anode.

Computational domain

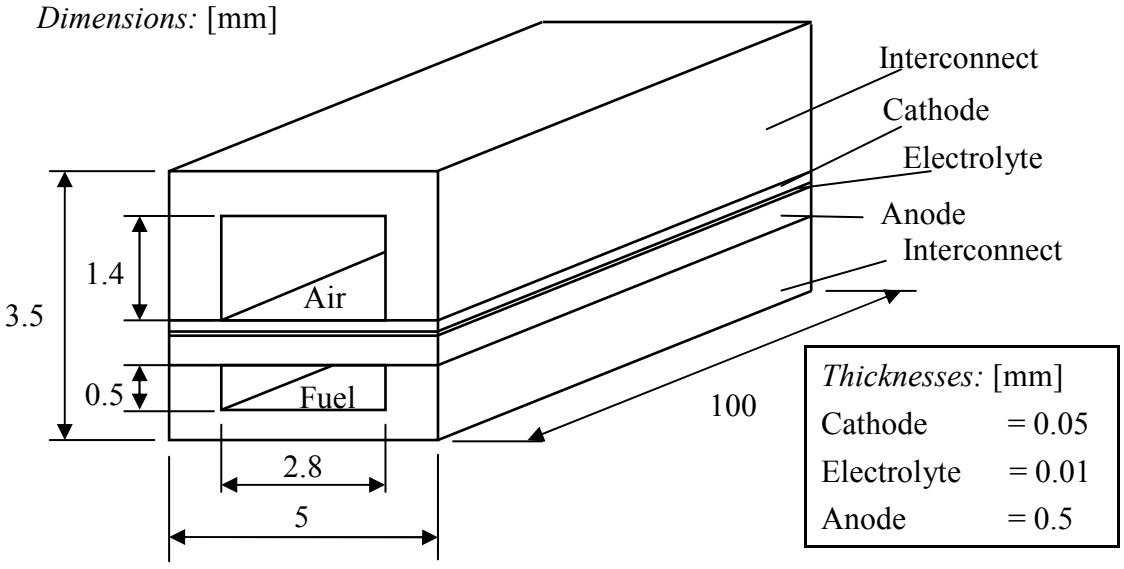

Fig. 3-1: Schematic of one channel region and its geometries.

In a practical planer SOFC system, a number of cells are stacked in series. When the number of the stacked cells is sufficiently large, most of the cells located in the core of the stack are similarly surrounded by other cells and are therefore operated in a similar situation to each other. Attention is therefore focused in this study to a single cell in such a situation in a stack assuming that it represents the entire stack characteristics. In other words, we assume an ideal thermal insulation of the system and the cells in the stack are identical. As shown in Fig. 3-1, a planar SOFC of co- and counter-flow types was modeled with the pair of two channels under a steady-state condition; the SOFC is composed of the fuel and air channels, the solid structure (anode, electrolyte and cathode) and interconnection.

3.1.1 The electrochemical model

The electrochemical reaction is considered to be attributed to only hydrogen; the electrochemical fuel value of CO is readily exchanged for hydrogen by the rapid shift reaction assuming chemical equilibrium [15],[34]. In other words, CO is considered to take part only in the shift reaction. Whereas the open-circuit voltage (V_{OC}) of an internal reforming SOFC is calculated according to the electrochemical oxidation of H_2, the species' consumption and production is determined collectively from the reforming reactions. The DIR-SOFC model developed in this work incorporates steam reforming, dry reforming and partial oxidation reactions due to the presence of H_2O, CO_2 and O_2 in the anode. The model is capable of capturing the distribution of the local temperatures, species concentrations, current density, and polarization losses in streamwise direction.

Steam reforming: $$CH_4 + H_2O \rightarrow CO + 3H_2 \quad (3\text{-}1)$$

Dry reforming: $$CH_4 + CO_2 \rightarrow 2CO + 2H_2 \quad (3\text{-}2)$$

Since steam and dry reforming reactions are intensively endothermic, it is necessary to supply high temperature inlet streams to SOFC stack; thus reducing the overall efficiency. This problem can be overcome by applying an exothermic partial oxidation reaction which utilizes air as the reforming agent.

Partial oxidation: $$CH_4 + \frac{1}{2}O_2 \rightarrow CO + 2H_2 \quad (3\text{-}3)$$

Nevertheless, when fuel gas and oxidant are mixed, the nature of the partial oxidation of methane has been a matter of debate for a long time. Hibino [35-36] and Buergler [37]

have suggested that, fuel in nickel anode channel, the partial oxidation of methane takes place via a two-step mechanisms. In the first step of the mechanism, full oxidation of methane takes place producing CO_2 and H_2O; followed by the second step where synthesis gas is produced through steam reforming of unreacted methane while water-gas shift reaction is at equilibrium. Full oxidation of CH_4 in the oxygen-rich zone yields CO_2 and H_2O.

Methane full oxidation: $$CH_4 + 2O_2 \rightarrow CO_2 + 2H_2O \quad (3\text{-}4)$$

Dry reforming reaction Eq. (3-2) is not explicitly included, but is implicitly considered through the water-gas-shift reaction Eq. (3-5). As mentioned above, the water-gas-shift reaction is always assumed to be at equilibrium in this study. The water-gas-shift reaction converts CO into H_2.

Water-gas shift reaction: $$CO + H_2O \leftrightarrow CO_2 + H_2 \quad (3\text{-}5)$$

The respective reaction rate equation for full oxidation of CH_4 [38] described in Eq. (3-4) on supported Ni catalysts is given as follows:

$$r_{FOX} = \frac{k_a p_{CH_4} p_{O_2}}{\left(1 + K^{OX}_{CH_4} p_{CH_4} + K^{OX}_{O_2} p_{O_2}\right)^2} + \frac{k_b p_{CH_4} p_{O_2}}{\left(1 + K^{OX}_{CH_4} p_{CH_4} + K^{OX}_{O_2} p_{O_2}\right)} \quad (3\text{-}6)$$

where p_i is the partial pressure of species *i* in gas mixture.
The Arrhenius reaction rate for species *i* in combustion reaction k_i is expressed as:

$$k_i = A(k_k)\exp\left(\frac{E_k}{R \cdot T}\right) \quad (3\text{-}7)$$

The adsorption constant for species *i* in combustion reaction K_i^{OX} is expressed as:

$$K_i^{OX} = A(K_i)\exp\left(\frac{\Delta H_{k,i}}{R \cdot T}\right) \quad (3\text{-}8)$$

Table 3-1: Calculation based parameters for the reaction rate constants in Eq. (3-7) and the adsorption constants in Eq. (3-8).

	$A(k_k)$	E_k (kJ mol^{-1})		$A(K_i)$	ΔH_k (kJ mol^{-1})
k_a (kmol kg$_{cat}^{-1}$ bar^{-2} h^{-1})	2.92×10^6	86.0	$K^{OX}_{CH_4}$ (bar^{-1})	1.26×10^{-7}	-27.3
k_b (kmol kg$_{cat}^{-1}$ bar^{-2} h^{-1})	2.46×10^6	86.0	$K^{OX}_{O_2}$ (bar^{-1})	7.87×10^{-7}	-92.8

Taken from [38]

The reaction rate of the steam reforming reaction Eq.(3-1) can be expressed as[39]:

$$r_{SR} = k_{\mathrm{CH_4}}\left(1 - \frac{p_{\mathrm{CO}}\, p_{\mathrm{H_2}}^2}{p_{\mathrm{CH_4}}\, p_{\mathrm{H_2O}}\, K_{eq,SR}}\right) p_{\mathrm{CH_4}} \exp\left(\frac{-E_{\mathrm{CH_4}}}{R \cdot T}\right) \qquad (3\text{-}9)$$

where $E_{\mathrm{CH_4}}$ (= 82 kJ mol^{-1}) is the activation energy of the reaction and $k_{\mathrm{CH_4}}$ (= 4274 mol m^{-2} bar^{-1} s^{-1}) is the pre-exponential factor.

The equilibrium constant for the water-gas-shift reaction and the steam reforming reaction can be described as follows [40]:

$$K_{p,shift} = \exp\left(-0.2935 Z^3 + 0.6351 Z^2 + 4.1788 Z + 0.3619\right) \qquad (3\text{-}10)$$

$$K_{eq,SR} = 1.0267 \times 10^{10} \exp\left(-0.2513 Z^4 + 0.3665 Z^3 + 0.5810 Z^2 - 27.134 Z + 3.2770\right) \qquad (3\text{-}11)$$

where $Z = \frac{1000}{T} - 1$.

Mass balances are formulated for each species on the basis of the relationship between the local current and the change in the concentrations. In this study, the oxidation of hydrogen is the only electrochemical reaction.

Overall cell reaction:

$$\mathrm{H_2} + \frac{1}{2}\mathrm{O_2} \rightarrow \mathrm{H_2O} \qquad (3\text{-}12)$$

The open-circuit voltage (V_{OC}), is described by the Nernst equation as a function of operating temperature (T) and partial pressure (p).

$$V_{OC} = \frac{\Delta G^0}{2F} + \frac{R \cdot T}{2F} \cdot \ln\left(\frac{p_{\mathrm{H_2}}\, p_{\mathrm{O_2}}{}^{1/2}}{p_{\mathrm{H_2O}}}\right) \qquad (3\text{-}13)$$

This function is calculated taking into account the ideal gas mixture model and the empirical correlations for specific heats. Although the open circuit reversible voltage decreases when temperature increases, the real voltage shows the opposite trend since polarizations must be taken into account. Thus, when electrons flow through the internal and external SOFC circuit some losses must be taken into account, decreasing cell voltage. These losses are mainly due to: (i) concentration polarization, V_{conc}; (ii) circuits ohmic polarization, V_{omh}; (iii) activation polarization, V_{act}. In this simulation, polarizations due to fuel and electrons crossover through electrolyte are neglected. Consequently, the overall cell voltage is calculated as follows.

Concentration polarization

The concentration polarization is the result of the finite gas diffusion processes that govern movement of gasses into and out of the electrochemical reaction. The rate of mass transport of gases is described by Fick's first law. Therefore, the maximum rate of gas diffusion (which is directly related to the maximum current density that can be obtained) is found when concentration of fuel at the electrochemically active area is assumed to be zero. The potential difference between operation where current is flowing and not flowing is the concentration polarization and is equal to:

$$V_{conc,an} = \frac{R \cdot T}{2F} \ln\left(\frac{p_{H_2O,TPB} p_{H_2}}{p_{H_2O} p_{H_2,TPB}} \right) \tag{3-14}$$

$$V_{conc,ca} = \frac{R \cdot T}{4F} \ln\left(\frac{p_{O_2}}{p_{O_2,TPB}} \right) \tag{3-15}$$

$$p_{H_2,TPB} = p_{H_2,an} - i_c \frac{R \cdot T \cdot \delta_{an}}{2F \cdot D_{H_2O,eff}} \tag{3-16}$$

$$p_{H_2O,TPB} = p_{H_2O,an} + i_c \frac{R \cdot T \cdot \delta_{an}}{2F \cdot D_{H_2,eff}} \tag{3-17}$$

$$p_{O_2,TPB} = P_{air} - \left(P_{air} - p_{O_2,ca}\right) \exp\left(i_c \frac{R \cdot T \cdot \delta_{ca}}{4F \cdot P_{air} \cdot D_{O_2,eff}} \right) \tag{3-18}$$

In the equations, i_c is current density, P represents total pressure, and $D_{i,eff}$ represents the effective diffusivities of the species i at anode and cathode. To evaluate the effective diffusivities, combined ordinary and Knudsen diffusion [41] has been used:

$$\frac{1}{D_{i,eff}} = \left(\frac{\varepsilon_p}{\tau} \right) \left(\frac{1}{D_{im}} + \frac{1}{D_{ik}} \right) \tag{3-19}$$

where ε_p and τ are the porosity and tortuosity of electrode materials, respectively, shown in Table 3-2. Diffusivity of species i in multicomponent gas mixture, D_{im} can be estimated by Wilke [42]:

$$D_{im} = \frac{1 - x_i}{\sum_{j \neq i} \left(x_j / D_{ij} \right)} \tag{3-20}$$

where x_i is the molar fraction of gas species i. For prediction of the binary diffusivity of

the gas mixture composed of species i and j (D_{ij}), the Fuller-Schettler-Giddings formula [41] is adopted in this study.

$$D_{ij} = \frac{0.1013T^{1.75}\left(\frac{1}{M_i}+\frac{1}{M_j}\right)^{0.5}}{P\left[\left(\sum \upsilon_i\right)^{1/3}+\left(\sum \upsilon_j\right)^{1/3}\right]^2} \tag{3-21}$$

where M_i is molecular weight of species i; $\Sigma\upsilon_i$ represents diffusion volume of species i, which values can be found in [41] ,Knudsen diffusion (D_{ik}) can be expressed as:

$$D_{ik} = 48.5 d_{pore}\left(\frac{T}{M_i}\right)^{0.5} \tag{3-22}$$

where d_{pore} is pore diameter.

Table 3-2: Calculation based parameters for diffusion polarization.

Parameter	Value
Electrode porosity (ε_p) (-)	0.48
Electrode tortuosity (τ) (-)	5.4
Pore diameter (d_{pore}) (μm)	1.0

Taken from [43]

Activation polarization

Chemical reactions, including electrochemical reactions, involve energy barriers which must be overcome by the reacting species. This energy barrier is called the 'activation energy' and results in activation or charge-transfer polarization, which is due to the transfer of charges between the electronic and the ionic conductors taking place at the three-phase boundary layer of both electrodes. The activation polarization may be regarded as the extra potential necessary to overcome the energy barrier of the rate-determining step of the reaction to a value such that the electrode reaction proceeds at a desired rate. Activation polarization (V_{act}) is normally expressed by the well known Butler Volmer equation:

$$i_c = i_o\left\{\exp\left(\beta\frac{n_e\cdot F\cdot V_{act}}{R\cdot T}\right)-\exp\left[-(1-\beta)\frac{n_e\cdot F\cdot V_{act}}{R\cdot T}\right]\right\} \tag{3-23}$$

where i_c is current density and the parameters n_e and β in Eq. (3-23) were set equal to 2 and 0.5, respectively [44].

The activation overpotential can be expressed as:

$$V_{act} = \frac{2R \cdot T}{n_e F} \sinh^{-1}\left(\frac{i_c}{2i_0}\right) \tag{3-24}$$

where i_0 is the exchange current density. Eqs. (3-25) and (3-26) are used to evaluate the values of the exchange current density for the anode and the cathode, respectively.

$$i_{0,an} = \gamma_{an}\left(\frac{R \cdot T}{2F}\right)\exp\left(-\frac{E_{act,an}}{R \cdot T}\right) \tag{3-25}$$

$$i_{0,cat} = \gamma_{cat}\left(\frac{R \cdot T}{2F}\right)\exp\left(-\frac{E_{act,cat}}{R \cdot T}\right) \tag{3-26}$$

Table 3-3: Calculation based parameters for activation polarization in Eqs.(3-25) and (3-26).

Parameter	Value
Pre-exponential factor for anode (γ_{an}) (A m^{-2})	6.54×10^{11}
Activation Energy for anode ($E_{act,an}$) (J mol^{-1})	140,000
Pre-exponential factor for cathode (γ_{cat}) (A m^{-2})	2.35×10^{11}
Activation Energy for cathode ($E_{act,cat}$) (J mol^{-1})	137,000

Taken from [34],[45]

Ohmic polarization

The ohmic losses in SOFC are due to: (i) the electrons flow through the anode, cathode and interconnections; (ii) the ionic flow through the electrolyte. The resistivity of the electrolyte material (ρ_i) strongly depends on the temperature [46]. Ceramic electrolyte used in SOFC usually shows moderate ion conductivity only at high temperature and this is the reason for the high operating temperature of SOFC. The resistance of the component *i* can be expressed as follows:

$$R_i = \rho_i \frac{\delta_i}{A_i} \qquad (\Omega) \tag{3-27}$$

Specific resistivity: $\rho_i = A_i \exp\left(\frac{-B_i}{T_{solid}}\right) \qquad (\Omega\, m)$

Table 3-4: Specific resistivity for the model.

Component	Material	Specific resistivity (ρ_j) ($\Omega\ m$)
Electrolyte	YSZ	$2.94\times10^{-5}\exp(10350/T)$ [a]
Anode	Ni/YSZ cermet	$2.98\times10^{-5}\exp(-1392/T)$ [a]
Cathode	LSM-YSZ	$8.114\times10^{-5}\exp(600/T)$ [a]
Interconnector	Doped $LaCrO_3$	0.0003215[b]

Taken from [a][47] [b][4]

3.1.2 The thermal model

As presented in Fig. 3-2, the one channel region is discretized into 90 control volumes of uniform size (Δx) in the *x*-direction. Each control volume contains three temperatures corresponding to air and fuel streams, T_{fuel} and T_{air}, and temperature of the cell or the solid part (PEN and interconnect are lumped together), T_{solid}, respectively. The mass and heat balances of each control volume are analyzed and solved by finite difference method. Fig. 3-2 also shows that the fuel always flows in the *x*-direction while air flows either in the *x*-direction (co-flow operation) or in the negative *x*-direction (counter-flow operation).

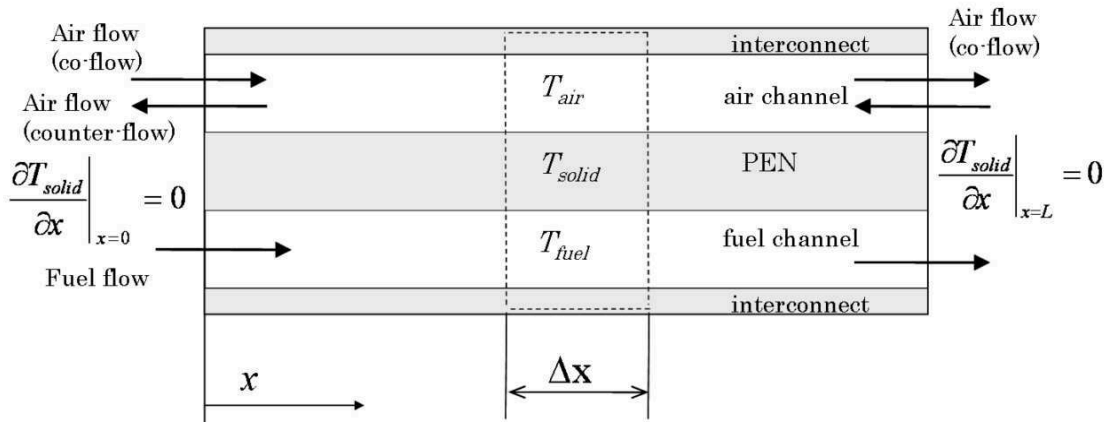

Fig. 3-2: Discretized domain for co- and counter-flow configuration.

The heat generation and heat transfer processes considered in the model are the heat release and absorption arising from the electrochemical reaction, the electrical resistance, convective heat transfer between the solid phase and gas streams and the conductive heat transfer in solid part. At an elevated temperature, heat transfer by thermal radiation can become important. However it is reported in literature [48-51] that unlike planar electrolyte-supported SOFC or tubular SOFC, the effect of radiation heat

transfer on temperature profiles is insignificant in planar anode-supported SOFC and can be negligible. As we only discuss the anode-supported planer SOFC in this study, we neglected the effects of thermal radiation.

At the air channel

Since no heat generation occurs in the airside, the energy conservation equation in air channel is given by:

$$0 = \rho_{air} C_{P,air} \Delta x A_{c,air} u_{air} \frac{\partial T_{air}}{\partial x} - h_{air} A_{s,air} (T_{solid} - T_{air}) \qquad (3\text{-}28)$$

where ρ_{air} is the density of gas mixture in air channel and $C_{P,air}$ is the specific heat capacity of gas mixture in air channel. The heat transfer coefficient h_{air} is given by the Nusselt expression:

$$h = \frac{Nu \cdot \lambda}{d_h} \qquad (3\text{-}29)$$

where d_h is the channel hydraulic diameter. The values of Nusselt number and thermal conductivity are set referring literature [52-53] and are summarized in Tables 3-5 and 3-6.

Table 3-5: Nusselt number.

	Air side	Fuel side
Nu	4.0	6.2

Taken from [52]

Table 3-6: Thermal conductivity.

	Anode	Cathode	Electrolyte
λ (W $m^{-1}K^{-1}$)	11.	6	2.7

Taken from [53]

At fuel cell

The energy balance of the solid part describes steady heat conduction in a quasi-homogeneous structure. For the solid part of the cell, the energy balance equation is given by:

$$Q_{source,solid} = \lambda_{solid} A_{c,solid} \Delta x \frac{\partial^2 T_{solid}}{\partial x^2} + h_{air} A_{s,air} (T_{solid} - T_{air}) + h_{fuel} A_{s,fuel} (T_{solid} - T_{fuel}) \quad (3\text{-}30)$$

The heat conduction coefficient of solid structure, λ_{solid} and the h_{air}, h_{fuel} are the convective heat transfer coefficiencies of air and fuel channel given above tables are used in the formula. $A_{s,air}$ and $A_{s,fuel}$ are the area of convection on air side and fuel side and Δx is the length of discretized control volume. The heat generation in solid structure ($Q_{source,solid}$) is caused by the effect of electrochemical reaction, steam methane reforming reaction and the ohmic loss, and is given by Eq. (3-31), where ΔH is the change in enthalpy of each reaction.

$$\begin{aligned} Q_{source,solid} = &-\left(3r_{SR} + r_{shift} + \Delta n_{H_2}\right) T_{solid} \Delta S_{H_2} - r_{SR} \Delta H_{SR} \\ &- r_{FOX} \Delta H_{FOX} + I \cdot V_{ohm} \end{aligned} \quad (3\text{-}31)$$

At fuel channel

Heat generation occurs from steam reforming and shift reactions. The governing energy equation for the fuel channel is:

$$0 = \rho_{fuel} C_{P,fuel} \Delta x A_{c,fuel} u_{fuel} \frac{\partial T_{fuel}}{\partial x} - h_{fuel} A_{s,fuel} (T_{solid} - T_{fuel}) - Q_{source,fuel} \quad (3\text{-}32)$$

The heat generation ($Q_{source,fuel}$) in the fuel channel is expressed as follows:

$$Q_{source,fuel} = -\left(r_{shift} + \Delta n_{CO}\right) \Delta H_{shift} \quad (3.33)$$

Boundary conditions for heat transfer equation:

$$\left.\frac{\partial T_{solid}}{\partial x}\right|_{x=0} = 0 \quad (3\text{-}34)$$

$$\left.\frac{\partial T_{solid}}{\partial x}\right|_{x=l} = 0 \quad (3\text{-}35)$$

3.1.3 SOFC model validation

To reveal performance limits and defects, numerical modeling has become a valuable tool for design and analysis. For a reliable discussion, it is essential to validate the numerical results. Because the detailed information on experimental results for

direct-internal-reforming SOFCs can rarely be found in literature, in this study, the model verification was achieved by comparing the numerical results with the actual case studies and simulation results by Ho et al. [54]. The electrochemical model used in this study was validated by comparing the numerical results with the experimental data of Zhao and Virkar [55]. The operating parameters and cell geometries are summarized in Table 3-7. As shown in Fig. 3-3, the predicted results fairly agree with the experimental counterparts. In particular, a good agreement is achieved when the operating temperature is relatively high at 1073 K. It corresponds to the temperature range of the numerical simulations discussed in the following chapter; consequently, the numerical model reliability can be established. The thermal model was also verified comparing the predicted results with the CFD-based simulation results of Ho et al. for the planar anode-supported SOFC with direct CH_4 reformation [54]. The channel geometries and operating conditions are illustrated in Table 3-8. In spite of the rather simple modeling of the present study compared to the CFD-based 2-D model by Ho et al., the performance predicted by the present 1-D model agrees reasonably well with the results of Ho et al. [54] as summarized in Table 3-9. Present results show slightly higher temperature deviations compared to those predicted by Ho et al. for co-flow operation and lower temperature deviations for counter-flow operation. This discrepancy between the two simulations is likely ascribed to the different model for the activation overpotential as well as the material properties taken from different sources.

Table 3-7: Operating parameters and SOFC channel geometries used in electrochemical model validation [55].

Parameters		Value
Button cell geometries		
Anode thickness (μm)		1000
Cathode thickness (μm)		20
Electrolyte thickness (μm)		8
Fuel/air stream inlet pressure (bar)		1.013
Cell mean temperature (K)		873-1073
Inlet gas composition	Fuel:	97% H_2 and 3% H_2O
	Air:	21% O_2 and 79% N_2

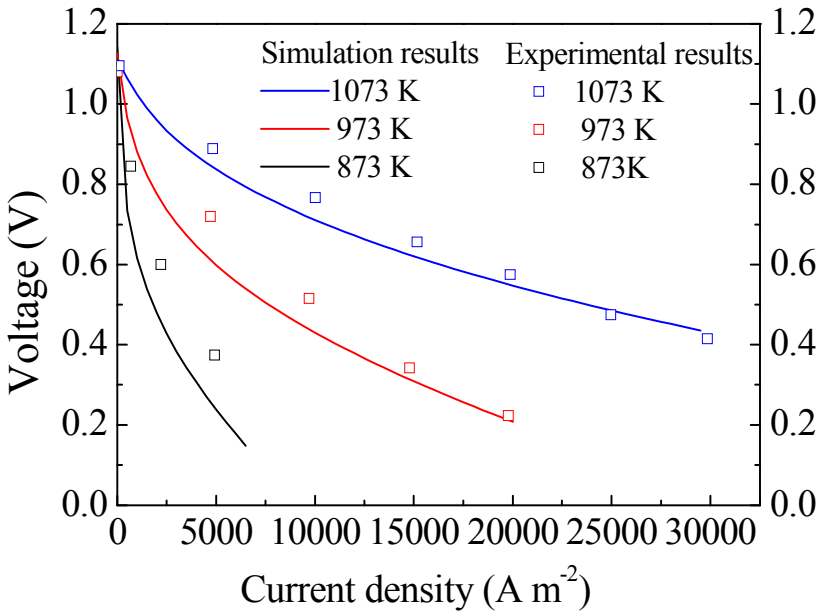

Fig. 3-3: Comparison of the simulation results with experimental data by Zhao et al. [55].

Table 3-8: Operating parameters and SOFC channel geometries used in model validation [54].

Parameters		Value
Cell length (mm)		100
Cell width (mm)		1
Air channel height (mm)		1
Fuel channel height (mm)		0.6
Anode thickness (μm)		630
Cathode thickness (μm)		50
Electrolyte thickness (μm)		20
Fuel inlet pressure (bar)		1.013
Air inlet pressure (bar)		1.013
Fuel utilization factor U_f (-)		0.85
Air utilization factor U_a (-)		0.3
Fuel inlet temperature (K)		1073
Air inlet temperature (K)		1073
Inlet gas composition	Fuel:	17.07% CH_4, 2.40% CO, 4.91% CO_2, 26.86% H_2 and 48.75% H_2O
	Air:	21% O_2 and 79% N_2

Table 3-9: Model validation results.

Parameter	Co-flow		Counter-flow	
	Ho et al.	Present	Ho et al.	Present
Voltage (V)	0.70	0.69	0.70	0.73
Power density (W A^{-2})	3850	3819	5320	5747
Current density (i_{ave}) (A m^{-2})				
Average	5500	5498	7600	7888
Maximum	6350	7500	12400	12600
Minimum	4000	3400	3500	3216
Cell temperature (T_{solid}) (K)				
Maximum	1155	1184	1260	1160
Minimum	1020	1013	1090	1076

3.2 Biomass gasifier model

In this study, a steady-state equilibrium model was developed to predict the product gas from the biomass gasification with mixed air-steam. To produce high quality syngas rich in H_2, the amount of steam as oxidizing agent was varied, while the relatively small amount of air is tuned to sustain the operating temperature to the desired point by partial oxidation. Generally, at sufficiently high gasifying temperatures, tar production can be negligibly eliminated from gasification products. Since the model does not take into account tars formation in the gasifier, biomass gasifier operate at 1073 K under near ambient pressure, and syngas outgoing temperature of 1073 K is assumed.

The carbon-hydrogen-oxygen (C-H-O) ternary diagrams have been constructed as shown in Fig. 3-4. The biomass fuel considered in this work is represented by ash-free typical wood fuel formula of $CH_{1.4}O_{0.59}N_{0.0017}$. In ternary C-H-O diagram, the solid line presents, the so-called carbon deposition boundary. Since the biomass fuel is located in the carbon deposition region, oxygen, steam are used as gasifying agent to bring down chemical equilibrium below carbon deposition boundary lines. Figure 3-4 shows that the increase of steam as oxidizing agent (STBR increases) in this study minimizes the risk for carbon deposition.

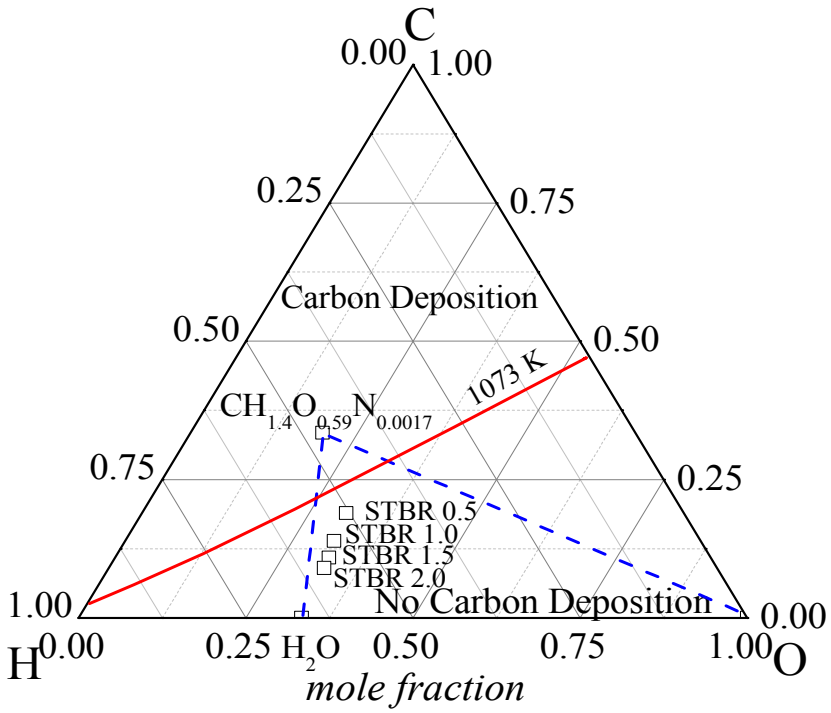

Fig. 3-4: C-H-O ternary diagram with carbon deposition boundary at 1073 K, 1 atm.

Gasification is a partial-oxidation process for the conversion of carbonaceous feedstocks to combustible gas mixtures consisting primarily of carbon monoxide (CO), hydrogen (H_2), and methane (CH_4). The global gasification reaction for $CH_aO_bN_c$ can be written as follows:

$$\mathrm{CH_aO_bN_c} + m\mathrm{H_2O} + \lambda\mathrm{O_2} + 3.76\lambda\mathrm{N_2} \leftrightarrow n_1\mathrm{H_2} + n_2\mathrm{CO} + n_3\mathrm{CH_4} + n_4\mathrm{CO_2} + n_5\mathrm{H_2O} + n_6\mathrm{N_2} \tag{3-36}$$

where m is number of moles of water vapor which can be calculated using the following relation:

$$m = \frac{M_{biomass} m_{biomass,moisture}}{18\left(1 - m_{biomass,moisture}\right)} \tag{3-37}$$

where $M_{biomass}$ is molecular mass of biomass and $m_{biomass,moisture}$ is the mass flow rate of the moisture in biomass.

Gasification process consists of two stages. In the first stage, pyrolysis releases the volatile components of the organic compounds and results in char. In the second stage, the carbon in the char is reacted with steam, air, or pure oxygen. It is reported that the gas compositions is dominated by the water–gas shift reaction at the higher temperature

>1023 K in biomass gasification process [56].

Water-gas shift reaction: $\mathrm{CO} + \mathrm{H_2O} \leftrightarrow \mathrm{CO_2} + \mathrm{H_2}$ (3-5)

Methane is formed through the following exothermic reaction.

Carbon hydrogenation reaction: $\mathrm{C} + 2\mathrm{H_2} \leftrightarrow \mathrm{CH_4}$ (3-38)

The above two reactions are the major reactions that occur in gasification process [57-58]. The equilibrium constant for water-gas shift and carbon hydrogenation reactions are:

$$K_1 = \frac{P_{\mathrm{CO_2}} P_{\mathrm{H_2}}}{P_{\mathrm{CO}} P_{\mathrm{H_2O}}} = \frac{n_4 n_1}{n_2 n_5} \tag{3-39}$$

$$K_{p,shift} = \exp\left(-0.2935Z^3 + 0.6351Z^2 + 4.1788Z + 0.3619\right) \tag{3-10}$$

where $Z = \frac{1000}{T} - 1$.

$$K_2 = \frac{P_{\mathrm{CH_4}}}{\left(P_{\mathrm{H_2}}\right)^2} = \frac{n_3}{n_1^2} n_{tot} \tag{3-40}$$

The equilibrium constant is determined by Gibbs free energy as a function of temperature as follows:

$$K(T) = \exp\left(\frac{-\Delta G^0}{R \cdot T}\right) \tag{3-41}$$

The main operating parameters are steam to biomass ratio (STBR) and equivalence ratio (ER). They refer to the amount of gasifying agents affecting the performances of gasifier.

The steam to biomass ratio (STBR) can be defined as:

$$\mathrm{STBR} = \frac{m_{steam} + m_{biomass,moisture}}{m_{biomass,d.b.}} \tag{3-42}$$

Here, m_{steam} is the mass flow rate of the steam and $m_{biomass,d.b.}$ is the mass flow rate of the dry biomass.

The equivalence ratio (ER) can be defined as:

$$\mathrm{ER} = \frac{m_{air}}{m_{air,stoic}} \tag{3-43}$$

Here, m_{air} is the mass flow rate of air and $m_{air,stoic}$ is the mass flow rate of air required for stoichiometric combustion.

3.2.1 Gasifier model validation

In order to evaluate the above models, simulation results are compared with experimental and numerical results from literature. The simulations were preformed by setting the same conditions as the experiments of Altatani et al. [59] and Zainal et al. [60]. The results are compared in Table 3-10. A good agreement exists between this model and the two models in the literature indicating that the equilibrium model predicts reasonably well the producer gas for a gasifier.

Table 3-10: The comparison between model predictions and measurements for two biomass gasification processes.

	Altatani et al.		Present	Zainal et al.		Present
	Experiment	model	model	Experiment	model	model
H_2 (vol%, d.b.)	14.00	20.06	18.70	15.23	21.06	19.82
CO (vol%, d.b.)	20.14	19.70	21.87	23.04	19.61	23.42
CH_4 (vol %,d.b.)	2.31	0.00	0.22	1.58	0.64	0.29
CO_2 (vol %,d.b.)	12.06	10.15	10.51	16.42	12.01	12.66
N_2 (vol %, d.b.)	50.79	50.10	47.30	42.31	46.68	43.80
HHV (MJ Nm^{-3})	5.28	5.04	5.31	5.49	5.42	5.60

3.3 Lumped Model in the MGT system

All of the temperatures, current densities, and molar fractions of the chemical species distribute non-uniformly along the fuel cell stack. Therefore, in this study, a one-dimensional model is applied to SOFC. But, the MGT generally adopts a one-stage radial type compressor/turbine engine. Therefore, it is enough to analyze the performance of the MGT by a lumped model, which considers each component as a control volume. The MGT is composed of several parts: compressor, burner, recuperator, turbine, etc. Air supplied by the atmosphere is compressed by the

compressor, driven by the turbine and heated in the recuperator by the hot gas stream of the turbine exhaust. High temperature and high pressure air then enters the SOFC and electrochemically reacts with fuel (methane). The unutilized fuel from the SOFC is burnt completely in the burner. The equipment schematic and *Ts* diagram for a simple gas-turbine cycle are shown in Fig. 3-5. In this study, modeling of each component of the MGT was carried out as follows.

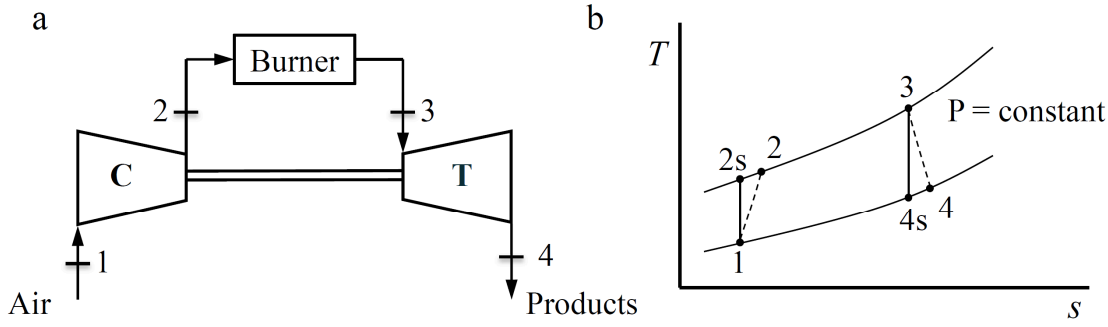

Fig. 3-5: (a) Schematic of equipment; (b) *Ts* diagram for a simple gas-turbine cycle with irreversible compressor, turbine and burner.

3.3.1 Compressor and turbine

The actual gas turbine cycle differs from the ideal Brayton cycle. Some pressure drop during the heat addition and rejection processes is unavoidable. The outlet conditions from a compressor and turbine are basically calculated assuming an isentropic path. In fact, isentropic process is unrealistic and has two options for incorporating the irreversibility and heat losses of a process; isentropic and polytropic efficiencies [61]. The isentropic efficiency simply relates the actual outlet enthalpy (or temperature) to that expected from the isentropic process. In case of multi-stage compressor/turbine engine, the polytropic efficiency is more appropriate because each stage experiences different isentropic path. Therefore, in this study, the isentropic efficiency is enough to analyze the performance of the compressor and turbine because the concerned MGT is composed of one-stage centrifugal compressor and radial turbine, where the approximation holds when kinetic-energy changes is negligible. The isentropic efficiencies of the compressor and turbine are as follows.

Compressor

$$\eta_c = \frac{h_{2s} - h_1}{h_2 - h_1} \quad \left(or \quad \frac{T_{2s} - T_1}{T_2 - T_1} \right) \tag{3-44}$$

As can be seen in Fig. 3-5, subscript 1 and 2 are the inlet and outlet of a compressor, respectively. And, subscript c and s mean a compressor and the position after an isentropic path, respectively. If the specific heat at constant pressure is be calculated based on (2-19), the following (3-45) can be obtained from (3-44).

$$\eta_c = \frac{T_{2s} - T_1}{T_2 - T_1} = \frac{T_1}{T_2 - T_1}\left(\frac{T_{2s}}{T_1} - 1 \right) = \frac{T_1}{T_2 - T_1}\left[\left(\frac{P_2}{P_1} \right)^{\frac{\gamma - 1}{\gamma}} - 1 \right] \tag{3-45}$$

where γ is the ratio of specific heats.

Turbine

$$\eta_t = \frac{h_3 - h_4}{h_3 - h_{4s}} \quad \left(or \quad \frac{T_3 - T_4}{T_3 - T_{4s}} \right) \tag{3-46}$$

$$\eta_t = \frac{T_3 - T_4}{T_3 - T_{4s}} = \frac{T_3 - T_4}{T_4}\left[\frac{1}{1 - \left(\frac{P_4}{P_3} \right)^{\frac{\gamma - 1}{\gamma}}} \right] \tag{3-47}$$

In Fig. 3-5, subscript 3 and 4 are the inlet and outlet of a turbine, respectively. And, subscript t means a turbine.

3.3.2 Burner

The remainder of combusted fuel gas from the SOFC enters the burner where the hydrogen and carbon monoxide react with the oxygen from the spent air gas. The combusted gas preheats the incoming air, which goes through the combustor within the injection tube, and then operates the turbine. In comparison with general gas turbine engines, the necessity of temperature rise through the burner is relatively decreased because of the SOFC. Composition of the combustion product is calculated on the basis of stoichiometric combustion of hydrogen, carbon monoxide (and methane if remains),

as follows:

Hydrogen oxidation: $$H_2 + \frac{1}{2}O_2 \rightarrow H_2O \quad (3\text{-}48a)$$

Carbon monoxide oxidation: $$CO + \frac{1}{2}O_2 \rightarrow CO_2 \quad (3\text{-}48b)$$

Methane oxidation: $$CH_4 + 2O_2 \rightarrow CO_2 + 2H_2O \quad (3\text{-}48c)$$

The combustion process is assumed to be adiabatic with no work transfer. No change in total enthalpy must occur. Energy balance equation can be described as follows:

$$\sum_i (n_i h_i)_2 = \sum_i (n_i h_i)_3 \quad (3\text{-}49)$$

3.3.3 Heat exchanger

A regenerative gas turbine engine usually adopts a compact and high-efficiency heat exchanger that can be a recuperator (where the hot and cold streams exchange heat through a separating wall) or regenerator. In this study the system is equipped with a counter-flow type. The SOFC air and fuel streams are preheated by the cathode and anode off-gas, in order to avoid thermal stresses caused by large temperature difference between the inlet and the exit. This permits a fuel input to the combustor for a given power output of the engine. The transferred heat can be calculated with the effectiveness of the recuperator. According to Kays and London (1984) [62] the effectiveness (ε) is defined as:

$$\varepsilon = \frac{Q}{Q_{\max}} = \frac{C_c(T_{c,out} - T_{c,in})}{C_{\min}(T_{h,in} - T_{c,in})} = \frac{C_h(T_{h,in} - T_{h,out})}{C_{\min}(T_{h,in} - T_{c,in})} \quad (3\text{-}50)$$

where Q and Q_{max} are the actual heat transfer rate for a heat exchanger and the maximum possible heat transfer rate, respectively. C_c and C_h mean the hot and cold fluid heat capacity rates, respectively. C_{min} is equal to C_c or C_h, whichever is smaller, maximum possible heat transfer rate, respectively.

3.4 System parameters and efficiencies

Since the fuel and oxygen in air are not completely consumed by electrochemical reactions in anode and cathode compartments of the SOFC stack, the excess fuel and air flow rates can be determined by the fuel utilization factor (U_f) and the air utilization factor (U_a), key parameters investigated in this study. The fuel and air utilization factors are defined here as the ratio of fuel and oxygen consumed by the electrochemical reaction to fuel and oxygen in anode and cathode inlets, respectively.

$$U_f = 1 - \frac{\left(n_{\mathrm{H_2,SOFC}} + n_{\mathrm{CO,SOFC}} + 4n_{\mathrm{CH_4,SOFC}}\right)_{an,out}}{\left(n_{\mathrm{H_2,SOFC}} + n_{\mathrm{CO,SOFC}} + 4n_{\mathrm{CH_4,SOFC}}\right)_{an,in}} \tag{3-51}$$

$$U_a = 1 - \frac{\left(n_{\mathrm{O_2,SOFC}}\right)_{cat,\,out}}{\left(n_{\mathrm{O_2,SOFC}}\right)_{cat,\,in}} \tag{3-52}$$

Anode off-gas recycle ratio (AGR) is a system concept where anode off-gas is recirculated to the anode inlet to provide water vapor and heat to the anode feed gas. The amount of AGR is defined on a molar basis as:

$$\mathrm{AGR} = \frac{n_{recycle}}{n_{anode-off}} \tag{3-53}$$

The thermal energy to electric power ratio (TER) or heat-to-power ratio of CHP plant indicates the proportion of useful thermal energy to the electricity generation. It can be determined as:

$$\mathrm{TER} = \frac{Q_{useful}}{P_{\mathrm{SOFC}} + P_{\mathrm{MGT}}} \tag{3-54}$$

In energy conversion processes, the efficiencies can be defined in many ways. In this study we defined two kinds of efficiencies: energetic efficiency or fuel efficiency and rational efficiency for steady state processes by Kotas [63].

Energetic efficiency (η)

$$\eta = \frac{Energy\,in\,product\,outputs}{Energy\,in\,inputs} = 1 - \frac{Energy\,loss}{Energy\,in\,inputs}$$

In any system, energetic efficiency is defined as the ratio between energy in product outputs to the energy in the fuel inputs. It can be applied to SOFC as follows:

$$\eta_{\mathrm{SOFC}} = \frac{P_{\mathrm{SOFC}}}{\sum_{\mathrm{CH_4,CO,H_2}} \left(m_{fuel}\mathrm{LHV}\right)_{in}} \times 100\% \tag{3-55}$$

The energetic efficiency of a gasification process, generally known as the cold gas efficiency ($\eta_{cold\ gas}$), is the ratio between the chemical energy content in the produced syngas compared to the chemical energy in the original biomass fuel. The equation can be expressed as:

$$\eta_{cold\ gas} = \frac{m_{syn}\mathrm{LHV}_{syn}}{m_{biomass}\mathrm{LHV}_{biomass} + Q_{consumed}} \times 100\% \tag{3-56}$$

The system electrical efficiency for power generation system is defined as:

$$\eta_{ele,sys} = \frac{P_{\mathrm{SOFC}} + P_{\mathrm{MGT}}}{\left(m_{fuel}\mathrm{LHV}_{fuel}\right)_{in}} \times 100\% \tag{3-57}$$

The system CHP efficiency for cogeneration system is defined as:

$$\eta_{\mathrm{CHP}} = \frac{P_{\mathrm{SOFC}} + P_{\mathrm{MGT}} + Q_{useful}}{\left(m_{fuel}\mathrm{LHV}_{fuel}\right)} \times 100\% \tag{3-58}$$

Rational efficiency (ψ)

To give a realistic indicator of the system efficiency by taking exergy of the working fluid at the outlet that is obviously useful in the next component, the rational efficiency or rational exergetic efficiency is applied. The rational efficiency is one form of exergetic efficiencies initially defined by Kotas [63] as a ratio of the desired exergy output to the exergy consumed. The rational efficiency is to evaluate the maximum work that the system can achieve, in this study, we defined as:

$$\psi = \frac{Exergy\ in\ product\ outputs}{Exergy\ consumed}$$

The SOFC rational efficiency (ψ_{SOFC}) is the ratio of the produced electricity exergy to the exergy comsumed by SOFC. The equation can be expressed as:

$$\psi_{\mathrm{SOFC}} = \frac{P_{\mathrm{SOFC}}}{\sum\left(Ex_{fuel} + Ex_{air}\right)_{in} - \sum\left(Ex_{fuel} - Ex_{air}\right)_{out}} \times 100\% \tag{3-59}$$

The gasifier rational efficiency ($\psi_{gasifier}$) is the ratio of the exergy of produced syngas to

the sum of exergy associated with heat, biomass and gasifying agents entering the gasifier. The equation can be expressed as:

$$\psi_{gasifier} = \frac{Ex_{syn}}{Ex_{biomass} + Ex_{\dot{Q}_{consumed}}^{T_{gas}} + Ex_{air} + Ex_{steam}} \times 100\% \quad (3\text{-}60)$$

The system rational efficiency (ψ_{sys}) is the ratio of the produced electricity exergy to the exergy consumed by the system. The equation can be expressed as:

$$\psi_{sys} = \frac{P_{\mathrm{SOFC}}}{Ex_{fuel} - Ex_{exhaust}} \times 100\% \quad (3\text{-}61)$$

The rational efficiency can be applied to CHP system as follows:

$$\psi_{\mathrm{CHP}} = \frac{P_{\mathrm{SOFC}} + P_{\mathrm{MGT}} + Ex_{Q}^{T}}{Ex_{fuel,sys} - Ex_{exhaust}} \times 100\% \quad (3\text{-}62)$$

3.5 Calculation procedure

The SOFC and its applications to power generation system developed in this study are composed of two major modules, the SOFC and SOFC-based power systems. Figure 3-6 shows the computational flowchart of one-dimensional SOFC modeling capable of co- and counter-flow analyses. To facilitate direct and sensible comparisons of fuel cell performance, the SOFC modeling was constructed based on the prescribed values of average current density and fuel and air utilization factors. The distribution of the temperatures and species concentrations are solved iteratively by using finite volume method until convergence is obtained, before the local current density is integrated and re-corrected with the prescribed average current density.

The calculation procedure of the two SOFC-based power systems in this study, “solid oxide fuel cell-biomass gasification power generation system” and “solid oxide fuel cell-micro gas turbine (SOFC-MGT) hybrid combined heat and power (CHP) system”, are illustrated in Fig. 3-7. As the system power outputs are fixed for the performance evaluation of the two system studies, the amount of fuel inputs are varied to match with the desired power outputs while the calculations of SOFC and system components are solved iteratively until convergence is obtained. Exergy analyses are then carried out for evaluating the energetic and rational efficiencies of the two SOFC-based power systems.

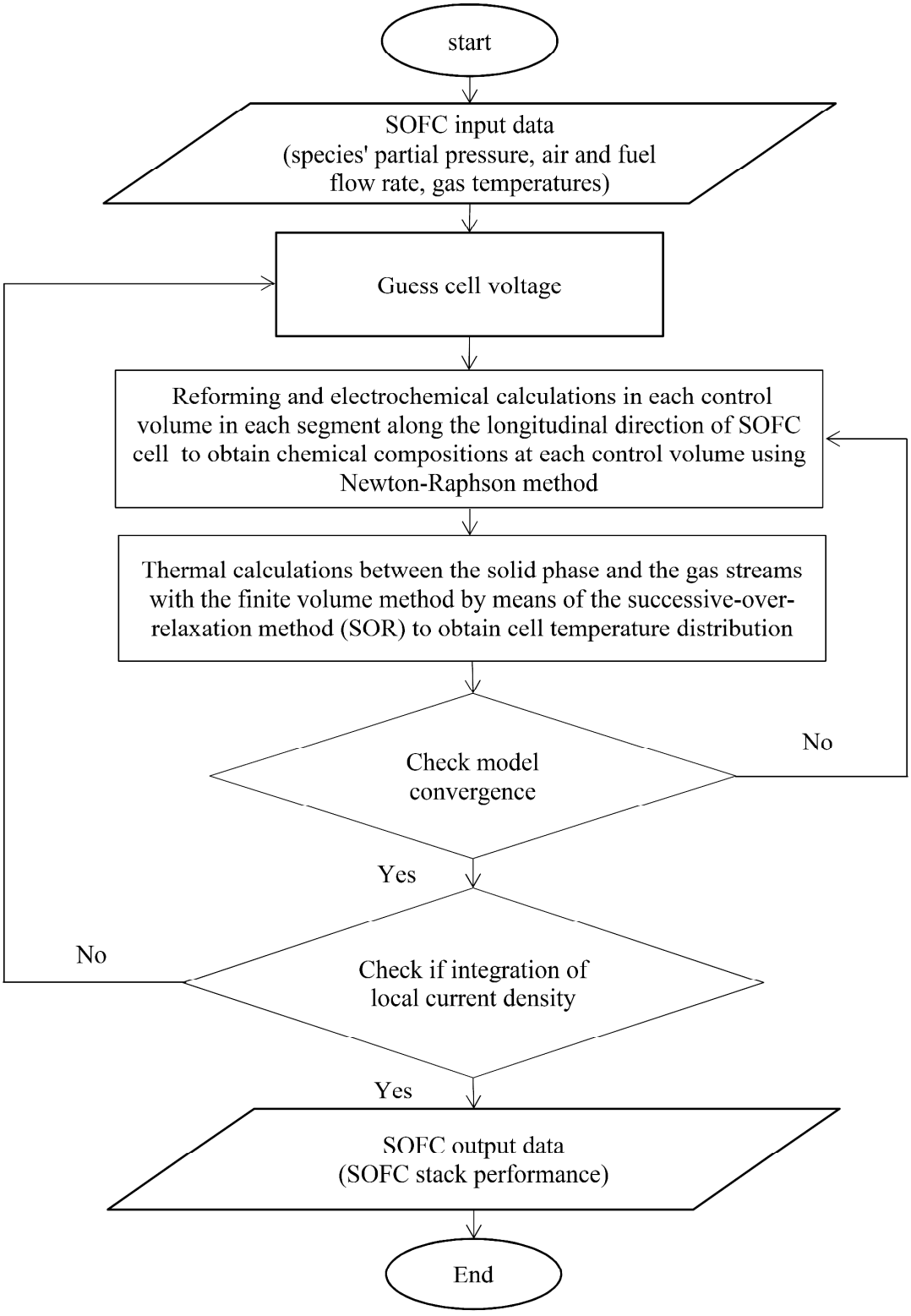

Fig. 3-6: Computational flowchart of SOFC modeling.

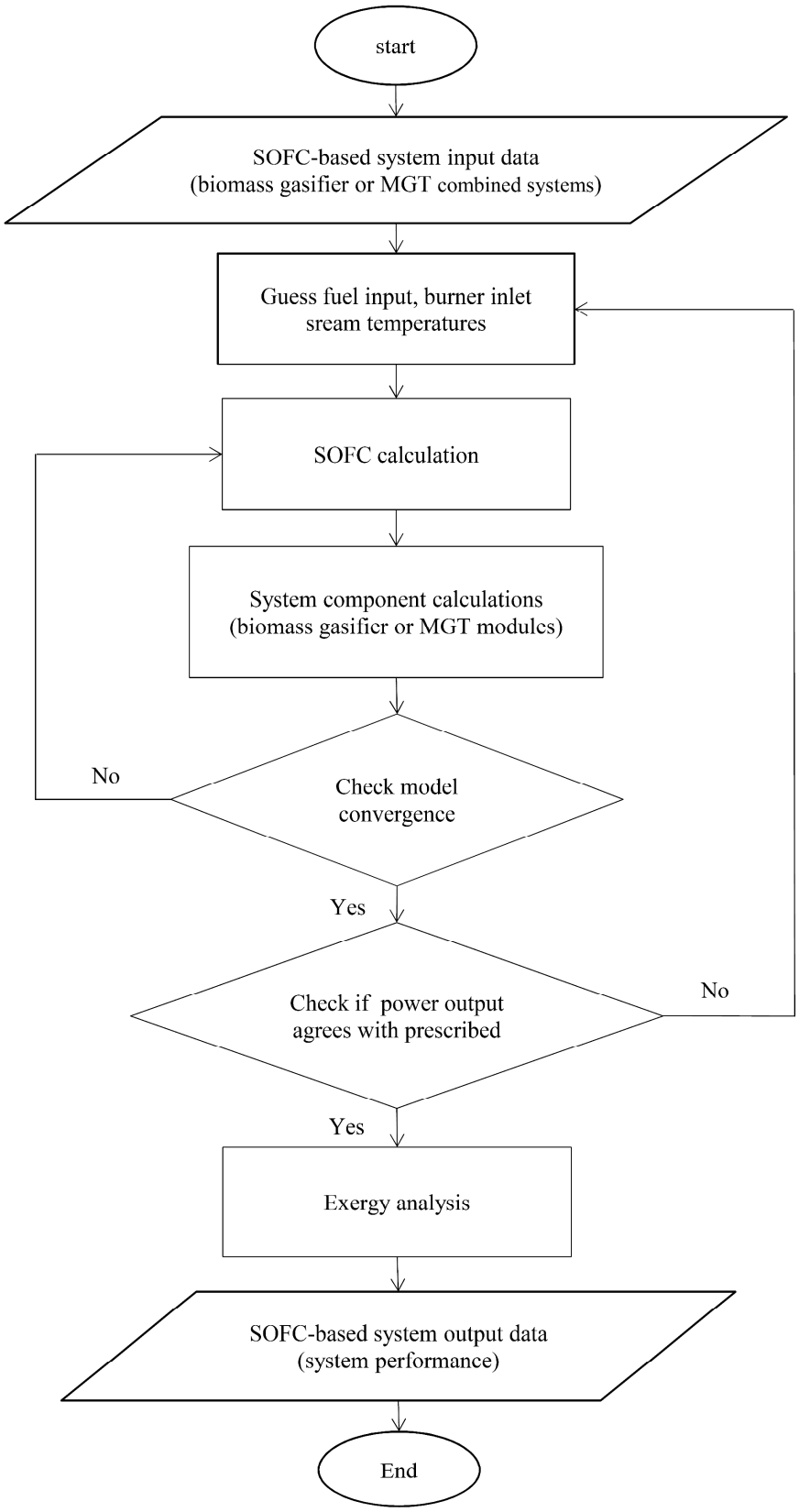

Fig. 3-7: Computational flowchart of SOFC-based system modeling.

Chapter 4

Selection of suitable operating conditions for planar anode-supported direct internal reforming-solid oxide fuel cell (DIR-SOFC)

4.1 Introduction

In this chapter, the numerical model developed and validated in Section 3.1 is used to clarify suitable operating parameters for co- and counter-flow operations considering both the efficiency and material constraints of an anode-supported planer DIR-SOFC. A comparative performance study between co- and counter-flow planar anode-supported DIR-SOFCs is performed under constant fuel and air utilization factors with the distribution of the temperatures, species concentrations, current density, and polarization losses. Since changing inlet temperatures can have either a beneficial or an undesirable impact on performance and life span of the cell, effects of the current density and inlet temperatures under co- and counter-flow operations are investigated by energy and exergy methods to clarify the maximum cell performance with lowest risk of thermal failure.

4.2 Fundamental characteristics of DIR-SOFC

The model described in Section 3.1 is applied to a planar DIR-SOFC to find its fundamental characteristics and to confirm the model's capability. Considering the periodic structure, it is modeled with one channel region of a single cell as illustrated in Fig. 3-1. The cell is a typical anode-supported structure with material properties described in Tables 3-1 to 3-5. The same geometry of one channel region is used for both co- and counter-flow cases. For the sake of consistency and simplicity, the inlet gas composition is chosen as a typical CH_4 syngas composition with steam to carbon

ratio of 2 [64]. The fuel flows from left to right in the following figures while the air stream direction is varied corresponding to the co-flow and counter-flow configurations. The fixed operating parameters are summarized in Table 4-1. Particular attention is paid to temperature profiles of the PEN layer, since the cell stack temperature gradient and maximum local cell temperature are the most important constraints due to material limitations.

Table 4-1: Operational parameter values for SOFC modeling.

Parameters		Value
Fuel inlet pressure (bar)		1.013
Air inlet pressure (bar)		1.013
Fuel utilization factor U_f (-)		0.80
Air utilization factor U_a (-)		0.30
Voltage (V)		0.80
Fuel inlet temperature (K)		1073
Air inlet temperature (K)		1073
Inlet gas composition	Fuel:	17.10% CH_4, 2.94 % CO, 4.36 % CO_2, 26.26% H_2 and 49.34% H_2O
	Air:	21% O_2 and 79% N_2

4.2.1 Co-flow operation

Strong endothermic reaction of methane reforming proceeds near the inlet. It results in a rapid change of the fuel gas compositions and temperature dip as can be seen in Fig. 4-1 and Fig. 4-2. The steep gradients of the methane and steam molar fractions observed in Fig. 4-1 show their quick consumptions resulting in the prominent increase of the hydrogen molar fraction. Because of the heat consumption associated with the reforming reaction, a local minimum temperature is observed near the fuel inlet as shown in Fig. 4-2. After methane depleted approximately 47 mm from the fuel inlet, the electrochemical oxidation of H_2 in parallel with the shift reaction are the major reactions proceed in the fuel passage and release reaction heat. It raises the local temperatures of the gasses and the cell resulting in the maximum cell temperature ($T_{solid,max}$) at the end of the channel (1118 K). The maximum cell temperature gradient $(\partial T_{solid}/\partial x)_{max}$ is 1.25 K mm^{-1} observed at the middle of the cell. It is also noted in Fig. 4-2 that the fuel flow

temperature is almost same as the cell temperature because of the small heat capacity of the fuel gas and flow rate. Near the inlet, the air temperature is higher than the fuel temperature. The air flow actually serves as a heat source for the reforming reaction, not as a coolant, in this region under the present condition. The air flow works as a coolant only after $x > 20$ mm where the air temperature is always less than the cell temperature.

Figure 4-3 presents the distributions of the open-circuit voltage, polarization terms and local current density under the same operation condition. The average current density was 2779A m^{-2} in this case. It shows that both the open-circuit voltage and the local current density have maximum values in the middle of the cell but their positions do not coincide. Their distributions are affected by the local temperature and local gas composition. The open-circuit voltage is the highest around $x = 15$ mm where the value of the activation polarization is also high because of the locally reduced temperature. On the other hand, although the activation polarization is the lowest near the exit, the open-circuit voltage is also low in this region because most of the fuel (hydrogen) has already been used up. Consequently the electrochemical reaction is most prominent at the middle of the cell. The figure also shows that the activation polarization is the major loss whereas the ohmic loss and the concentration polarization are relatively low and uniform.

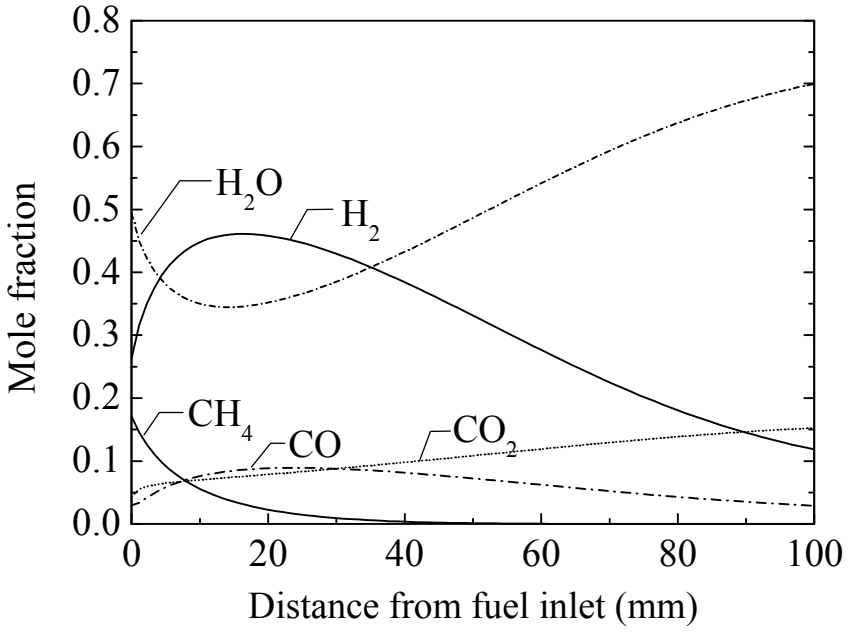

Fig. 4-1: Fuel channel molar fractions along the cell length, co-flow operation.

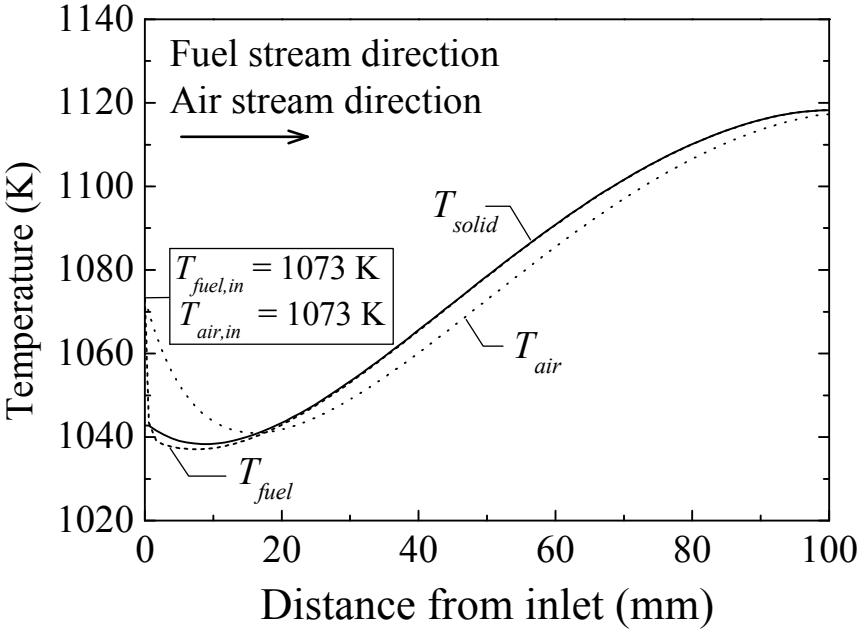

Fig. 4-2: Temperature distributions, co-flow operation.

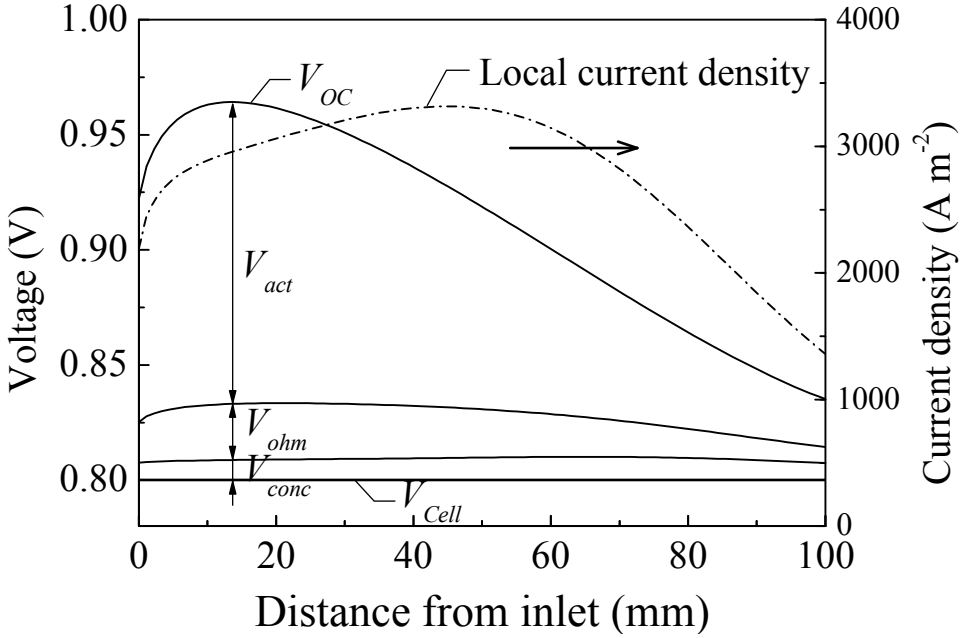

Fig. 4-3: Open-circuit voltage, polarization terms and local current density distributions, co-flow operation.

4.2.2 Counter-flow operation

Figure 4-4 shows the distributions of the molar fractions in the fuel stream for counter-flow case. Comparing Fig. 4-4 to Fig. 4-1, it is noted that the reforming reaction proceeds more rapidly in the counter-flow case and methane it is depleted approximately 33 mm from the fuel entrance. This is caused by the elevated cell temperature compared to the co-flow case. The higher the temperature is, the faster the steam reforming proceeds. The main difference between the two cases is the air temperature approaching to the fuel entrance region, $0 < x < 20$ mm, where the reforming reaction is active. While the air flow is directly supplied to the active reforming region in the co-flow case, it goes through the air passage of the cell in the counter-flow case accumulating heat generated in the cell. Consequently, as shown in Fig. 4-5, the air temperature approaching the active reforming region becomes much higher in the counter-flow case compared to the co-flow case even though the inlet temperatures are the same. This is an effective heat recovery process of a DIR-SOFC. However from the viewpoint of the temperature distribution, the counter-flow configuration needs to be examined carefully. The local cell temperature reaches its maximum value of 1194 K at 30 mm from the fuel entrance and the maximum cell temperature gradient $(\partial T_{solid}/\partial x)_{max}$ is 5.10 K mm^{-1} located at 8 mm from the fuel entrance. Comparing to the co-flow configuration, the maximum local cell temperature is increased 76 K and the maximum cell temperature gradient is increased 8 times. It should be noted that a large temperature gradient causes excessively high stress in the cell resulting in thermal cracking and cell failure. Therefore, the co-flow case is superior to the counter-flow case in term of material point of view and the cell temperature profile must be carefully monitored.

The open-circuit voltage, polarization terms and local current density distributions are shown in Fig. 4-6. The average current density was 4394 A m^{-2} in this case. The figure shows that the non-uniformity of the local current density distribution is considerably reinforced in the counter-flow configuration compared to that of the co-flow configuration shown in Fig. 4-3. The ohmic and concentration polarizations exhibit distributions that track the local current density distribution, whereas raising temperature results in the reduction of activation polarization.

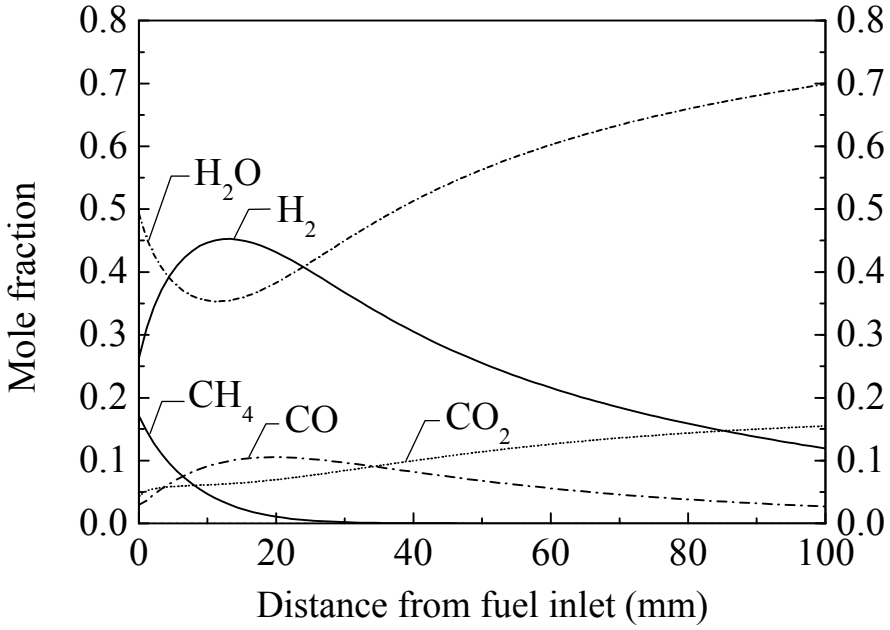

Fig. 4-4: Fuel channel molar fractions along the cell length, counter-flow operation.

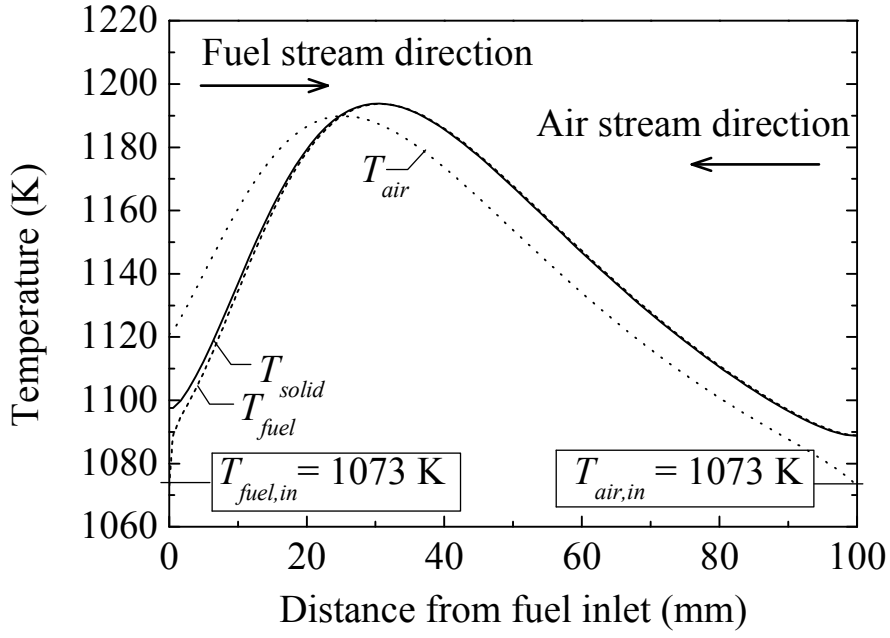

Fig. 4-5: Temperature distributions, counter-flow operation.

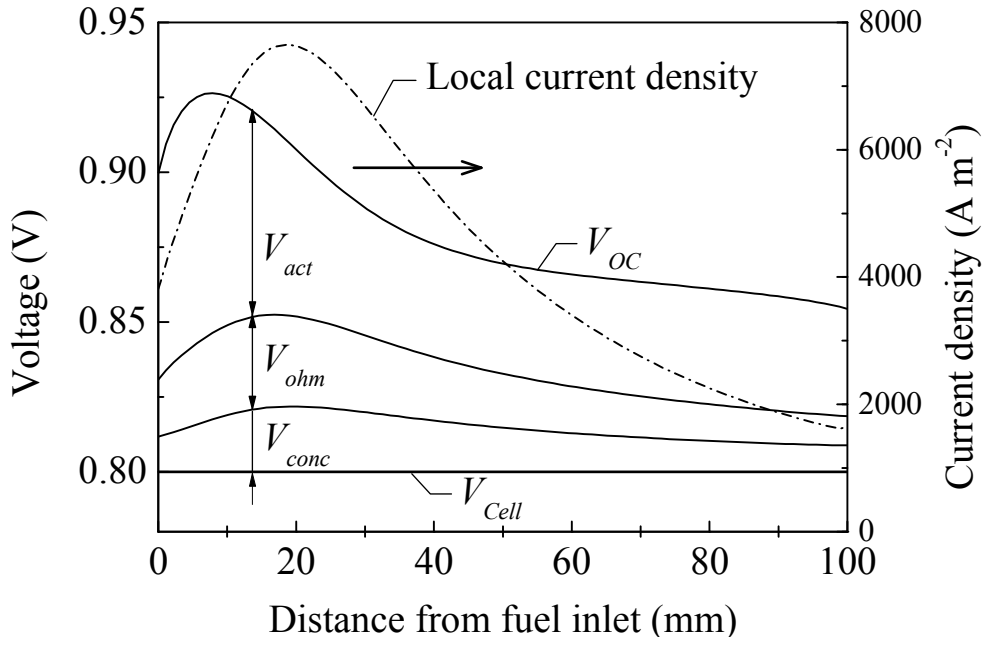

Fig. 4-6: Open-circuit voltage, polarization terms and local current density distributions, counter-flow operation.

4.3 Influence of current density

To compare the performance of the two configurations, Fig. 4-7 illustrates the predicted cell efficiencies and power density as a function of current density with cell voltage variation from 0.60 to 0.80 V. All other parameters are fixed at their standard values in Table 4-1. It can be seen that, the performance of the cell is hindered with an increase of current density. At 1000 A m^{-2}, the power density and efficiencies under the two configurations are very close to each other. The rational efficiency is much higher than the energetic efficiency, the main exergy losses owing to internal consumptions and the main energy losses associated with waste heat. It shows that there is a considerable potential in SOFC application to generate additional electric or heat power from the outlet streams. As current density increases, the power density difference between co- and counter-flow cases becomes more pronounced. The energetic efficiencies (η_{SOFC}) vary from 60.7 to 46.9% and from 61.6 to 54.0%; rational efficiencies (ψ_{SOFC}) vary from 83.8 to 66.1% and from 84.6 to 75.3%, for co-flow and counter-flow cases, respectively. The increase of the difference in the efficiencies between the co- and counter-flow cases is ascribed to the cell temperature difference. Because the fuel and air utilization factors are kept constant as shown in Table 4-1, the flow rates are tuned as the average current density is varied. At a high average current density, the flow rates are increased and the

amount of heat absorption by the reforming reaction becomes large as well as the heat generation in the cell associated with the electrochemical reaction and other irreversible losses. While the enthalpy of the inlet air flow is immediately supplied to the reforming reaction near the entrance region in the co-flow configuration, the air temperature first increases in the counter-flow configuration accumulating the heat generated in the cell. It results in a difference of the cell temperature, even though the sum of heat generation and absorption in a cell is expected to be similar in the two configurations. The difference of the average cell temperature between two configurations becomes larger as the average current density is increased. Figure 4-7 also shows that the energetic and rational efficiencies exhibit similar declining trends. This implies that the increases of the differences between exergy contents of inlet and outlet streams of the cell under co- and counter-flow operations are proportional to the increases of energy in fuel inputs. The decrease of cell performance with increasing the average current density is mainly associated with the increase of the activation polarizations. Figure 4-7 and the discussion in the previous sections lead to some considerations: (i) the increase of losses caused by the increased average current density results in the decline of energetic and rational efficiencies; (ii) co-flow operation is favourable for operation at a low current density mode due to the high efficiency and smaller temperature gradient. The analysis of Fig. 4-7 shows the advantages of using the present 1-D model in a system analysis. Unlike a lump model that takes only the energy balance into account, the present model considers heat transfer phenomena in the cell and can capture the performance difference caused by the temperature non-uniformity.

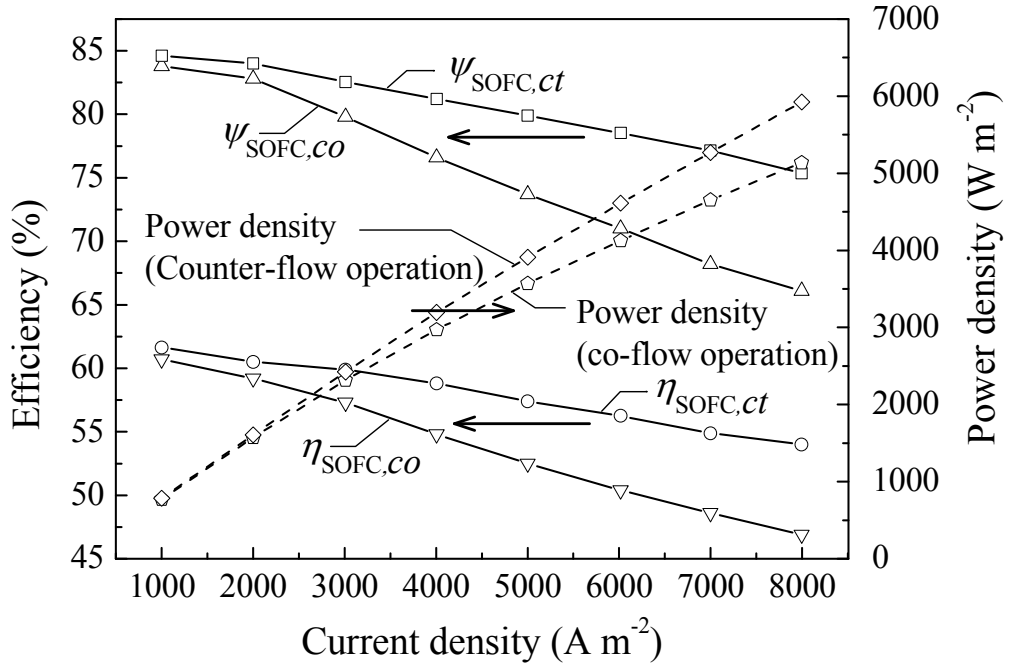

Fig. 4-7: Comparison of efficiencies and power density versus average current density for co- and counter-flow operation.

4.4 Influence of inlet temperatures

The inlet temperatures of the fuel and air flows are design parameters of a system. It affects the temperature distribution through heat transfer phenomena in the SOFC and eventually affects its performance as explained in the previous sections. A performance comparison was made with co- and counter-flow cell configurations operated at different air and fuel inlet temperature cases as listed in Table 4-2. Case I is the base case having the inlet fuel and air temperatures shown in Table 4-1. In Case II, only the inlet air temperature is reduced by 100 K from the base case and kept at 973 K, while both the fuel and air inlet temperatures are set at 973 K in Case III. The average current density is fixed at 4000 A m^{-2} for all cases.The cell terminal voltage and various losses are shown in Fig. 4-8 and 4-9, for the co- and counter-flow configurations, respectively. Although the open circuit voltage increases with decreasing operating temperature, the cell terminal voltage shows the opposite trend accounting of the increase of both ohmic and activation losses. In particular, the increase of the activation polarizations is significant among the three types of losses. The concentration polarizations can be considered as minor importance and are not significantly affected by the inlet temperatures.

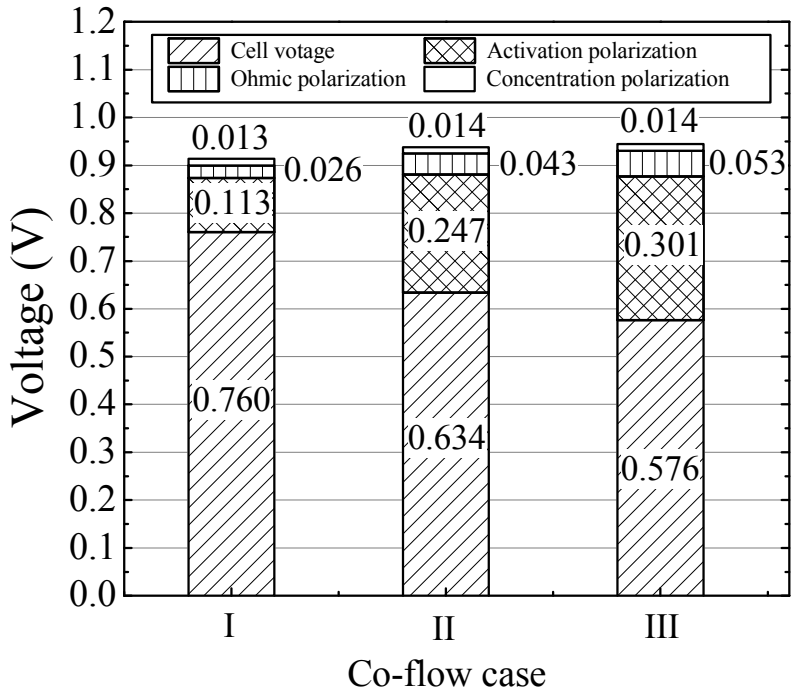

Fig. 4-8: Cell voltage and polarizations, co-flow operation.

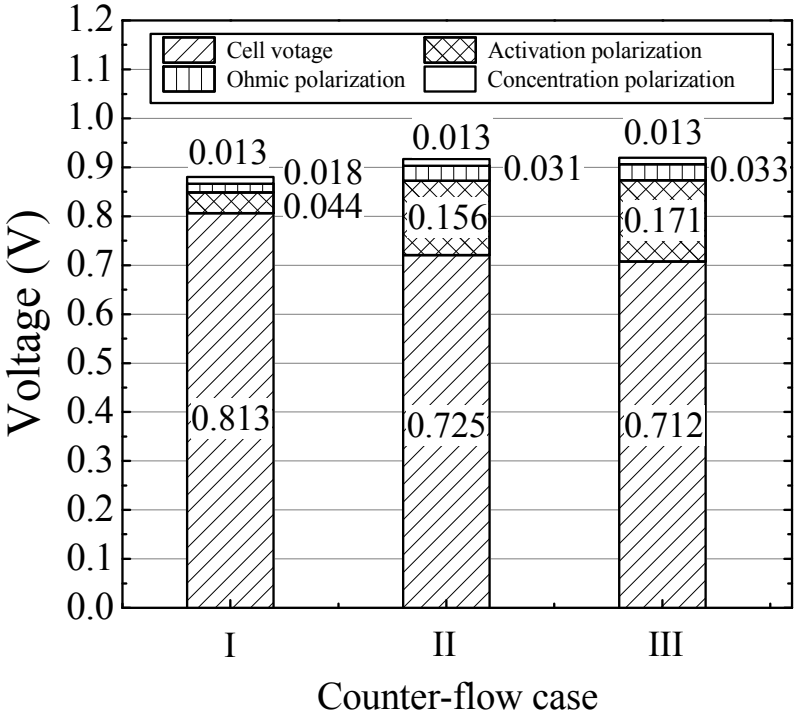

Fig. 4-9: Cell voltage and polarizations, counter-flow operation.

The cell temperature distributions of the three cases for the co-flow configuration are shown in Fig. 4-10. The cell temperature generally decreases when the inlet flow temperature is reduced. The cooling effect of the air temperature is more prominent compared to that of the fuel flow mainly because of its higher flow rate. The distribution profile is generally similar each other but the temperature gradient near the fuel entrance seems to be larger in Case II than other cases. Figure 4-11 shows the temperature distributions for the counter-flow configuration. Cooling effects by the reduced inlet temperature are obvious in the figure. As can been seen in Fig. 4-11, the Case II shows the most uniform temperature distribution among the three cases.

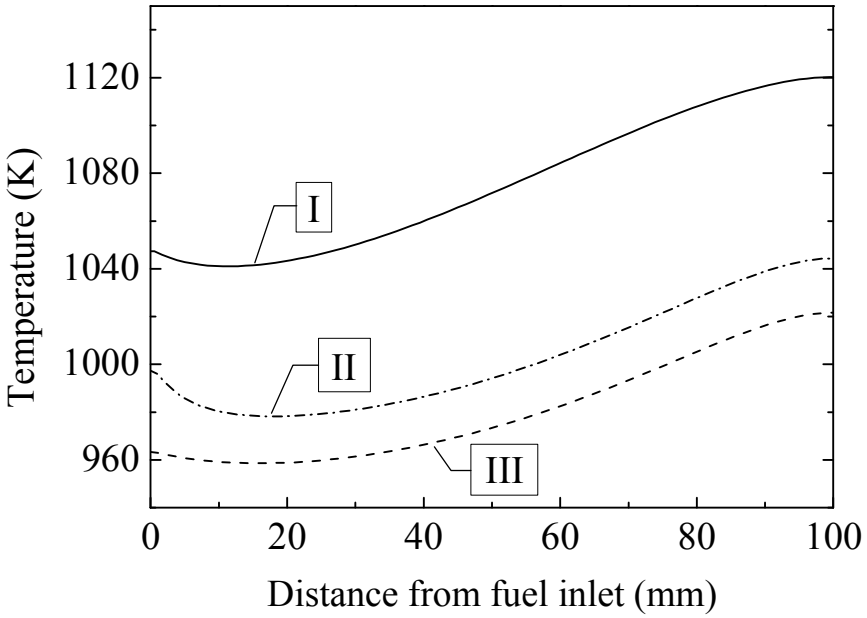

Fig. 4-10: Comparison of cell temperature distributions based on case studies, co-flow operation.

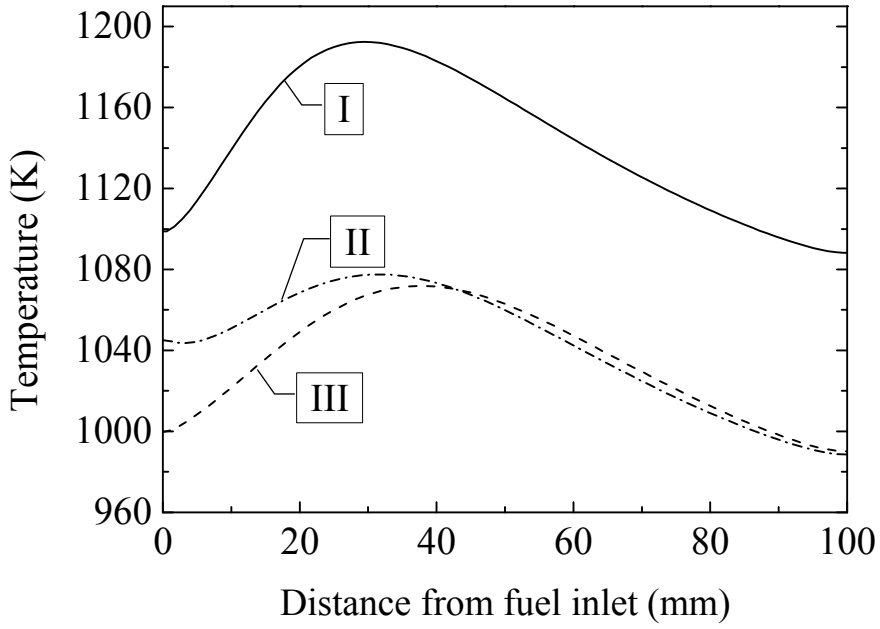

Fig. 4-11: Comparison of cell temperature distributions based on case studies, counter-flow operation.

Table 4-2: Summary of SOFC performance based on case study.

Inlet Stream Temp.			Co-flow				Counter-flow			
Case	$T_{fuel,in}$ (K)	$T_{air,in}$ (K)	$T_{solid,max}$(K)	$(\partial T_{solid}/\partial x)_{max}$ (K mm^{-1})	η_{SOFC}	ψ_{SOFC}	$T_{solid,max}$(K)	$(\partial T_{solid}/\partial x)_{max}$ (K mm^{-1})	η_{SOFC}	ψ_{SOFC}
I	1073	1073	1120	1.28	54.7	76.7	1192	5.17	58.6	81.3
II	1073	973	1044	3.24	45.6	64.0	1077	1.86	52.0	72.8
III	973	973	1021	1.20	41.7	57.6	1071	2.87	51.5	70.5

The performance comparison results along with the maximum local cell temperatures ($T_{solid,max}$) and the maximum cell temperature gradients $(\partial T_{solid}/\partial x)_{max}$,well known as the most important operational constraints for the planar SOFC, are listed in Table 4-2. It shows that the cell performance can be improved by setting the inlet temperatures high because the entire cell is maintained at high temperature as shown in Fig. 4-10 and 4-11. From the view point of a safe operation, cell temperatures (T_{solid}) and cell temperature gradients ($\partial T_{solid}/\partial x$) must be monitored with caution. A steep temperature gradient and high cell temperature can cause a severe adverse effect on the life span of the fuel cell. Their allowable values depend on materials, cell structure and manufacturing process. In this study, the values of the maximum allowable temperature gradient and the

maximum allowable cell temperature are set at 1300K and 5 K mm^{-1} [4], respectively, to consider the viability of SOFC. The maximum local cell temperatures presented in Table 4-2 do not seem to pose any problem to the cell while the maximum temperature gradient exceeds the allowable criteria in one case. In case II under co-flow operation, the maximum temperature gradient of 3.24 K mm^{-1} occurs near the fuel entrance, while the efficiencies are between those of the case I and III. While, case I under counter-flow operation is incompatible with the operational constraints. Although case I under counter-flow operation has the highest efficiencies, it is not a preferable operating condition due to the considerably large maximum cell temperature gradient of 5.17 K mm^{-1}, a critical operating condition for the cell. By reducing air stream inlet temperature, case II under counter-flow operation, the maximum cell temperature gradient and maximum local cell temperature are brought down to 1.86 K mm^{-1} and 1077 K, respectively. The study shows that, considering the balance between the cell performance and the operation safety, the most favourable operating condition among the six cases is case I under co-flow operation with η_{SOFC} and ψ_{SOFC} of 54.7, and 76.7%, respectively, at moderate maximum cell temperature gradient and moderate maximum local cell temperature of 1.28 K mm^{-1} and 1120 K. For all these results, the performance of DIR-SOFC under co-flow operation has a good potential to be further enhanced by simultaneously increasing inlet fuel and air temperatures until maximum cell temperature and cell temperature gradient approaching the material constraints.

In order to show the importance to consider material constraints more clearly, results of additional simulations of DIR-SOFC with a thick anode are presented. In this simulation, the anode thickness is doubled from its standard size, 500 μm, to 1000 μm. Other geometric and computational conditions are unchanged from the standard cases discussed above. The performance of the SOFC with thick anode is summarized in Table 4-3. A comparison with Table 4-2 shows that the effect of the anode thickness on η_{SOFC} and ψ_{SOFC} is minor. The efficiencies of the thick anode cells are 1 – 2% smaller than those of the standard cells. The drop of efficiency is mainly attributed to the increase of ohmic loss and concentration overpotential. The effect of the anode thickness on the temperature field, on the other hand, is significant. The maximum temperature and temperature gradient are reduced in the thick anode cells compared to those of the standard cells. This is caused by the reduction of the thermal resistance of the cell in the directions parallel to the cell surface. In all calculation listed in Table 4-3, the maximum temperature and maximum temperature gradient are lower than the allowable limits, 1300K and 5 K mm^{-1}. Increasing anode thickness allows counter-flow

cell configuration to operate within a safe operational condition. In Table 4-3, considering the balance between the cell performance and the operation safety, the most favourable operating condition among the six cases is case I under counter-flow operation.

Table 4-3: Performance of SOFC with thick anode (anode thickness = 1000 μm).

Inlet Stream Temp.			Co-flow				Counter-flow			
Case	$T_{fuel,in}$ (K)	$T_{air,in}$ (K)	$T_{solid,max}$(K)	$(\partial T_{solid}/\partial x)_{max}$ (K mm^{-1})	η_{SOFC}	ψ_{SOFC}	$T_{solid,max}$(K)	$(\partial T_{solid}/\partial x)_{max}$ (K mm^{-1})	η_{SOFC}	ψ_{SOFC}
I	1073	1073	1116	1.23	54.2	75.9	1168	3.39	57.6	79.3
II	1073	973	1041	1.99	45.3	63.4	1062	1.40	51.0	70.8
III	973	973	1017	1.05	41.4	57.0	1052	1.93	49.7	67.7

The above discussion based on Tables 4-2 and 4-3 shows that a preferred flow configuration can be changed depending on the cell geometry and operation conditions, if the material constraints are considered. This is a result that can never be obtained if the discussion is based only on the energetic efficiency. The energetic efficiency of a counter-flow case shown in Tables 4-2 and 4-3 is always higher than its counterpart co-flow case.

4.5 Influence of air utilization factor (U_a)

As mentioned earlier, counter-flow operation inherently provides highly efficient high efficiencies but prone to steep temperature gradient due to cooling effect. In this section, the effects of air utilization factor variation on counter-flow cell configuration of the standard cell (anode thickness of 500 μm) operated at fuel and air inlet temperatures of 1073 K are studied. The comparison of air utilization factors of 0.30, 0.20 and 0.10 is shown in Fig. 4-12. As fuel consumption rate is fixed due to constant fuel utilization factor, lowering air utilization factor reflects higher the amount of air supplied in excess at cathode. Since air flow is primary source of cooling, a reduce air utilization factor mitigates uneven temperature distribution by allowing higher cooling rate. In Table 4-4, maximum cell temperature gradients, maximum local cell temperatures, energetic and rational efficiencies corresponding to the variation of air utilization factor are presented. The critical maximum temperature gradient of 5.17 K mm^{-1} operated at air utilization factor of 0.30 can be lessened to safe operating level of 3.53 and 2.16 K mm^{-1} by varying air utilization factor to 0.20 and 0.10, respectively without significant efficiency

degradation. The simulation shows that increasing amount of excess air 3 times by reducing air utilization factor from 0.30 to 0.10 the energetic and rational efficiencies drop from 58.6 and 81.3% to 57.5 and 79.1%, respectively. However, it should be noted that lowering air utilization factor requires an increase in heat transfer to preheat the incoming air, resulting in higher parasitic losses as well as higher operating costs for bigger heat exchanger.

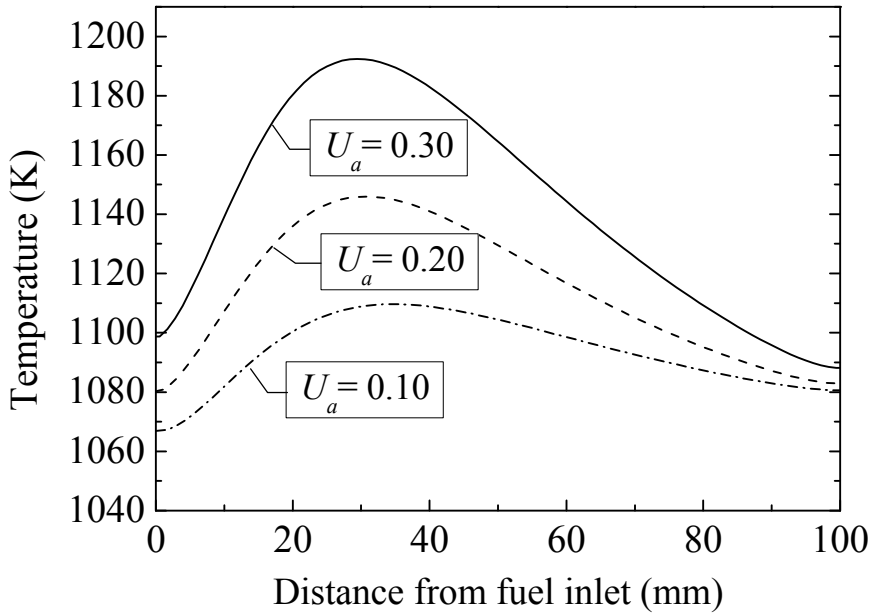

Fig. 4-12: Comparison of cell temperature distributions with air utilization factor variation, fuel and air inlet temperatures of 1073 K under counter-flow operation.

Table 4-4: Summary of counter-flow cell configuration SOFC performance with air utilization factor variation, fuel and air inlet temperatures of 1073 K.

U_a	$T_{solid,max}$(K)	$(\partial T_{solid}/\partial x)_{max}$ (K mm^{-1})	η_{SOFC}	ψ_{SOFC}
0.30	1192	5.17	58.6	81.3
0.20	1146	3.53	57.8	80.7
0.10	1109	2.16	57.5	79.1

4.6 Summary

A 1-D numerical model for a planar anode-supported DIR-SOFC with co- and counter-flow configurations was developed and validated. The calculations were carried out varying the average current density (1000 – 8000 A m^{-2}) and the gas inlet temperatures (973 – 1073 K) while keeping the fuel and air utilization factors constant at 0.80 and 0.30, respectively. The two configurations were evaluated through energy and exergy concepts with a consideration for the material constraints. Careful attention is paid to the maximum local temperature and the maximum temperature gradient of the cell. From the analysis, the following conclusions are made:

1. The significant difference is observed between the rational efficiency and the energetic efficiency in both configurations. It shows potential for additional power generation utilizing the exergy in outlet streams.
2. As the average current density is increased, the efficiencies naturally decrease but the tendency is more prominent in the co-flow configuration. The difference of the efficiencies between the co- and counter-flow configurations is very small at low current density but becomes more pronounced at high current density. The dependency of the energy and rational efficiencies on the flow configurations is successfully captured by applying the 1-D simulation.
3. As a result of the combined effects of heat generation, heat absorption and heat transfer in the cell, non-uniform temperature distribution is formed. The flow configuration affects the convective heat transport and plays a crucial role in supplying heat to the reforming reaction near the fuel entrance. The counter-flow configuration generally achieves high efficiencies but unfavourable in terms of strong temperature gradient. A preferred flow configuration can be changed depending on the cell geometry and operation conditions, if the material constraints are considered.
4. To evaluate the performance of SOFC, the material constraints need to be considered as well as the energy and rational efficiencies. The developed 1-D model based on the energy and exergy concepts can capture the temperature distribution affected by the control parameters of the system, such as the gas inlet temperatures, gas flow rates and the average current density. It is a useful tool for system analysis work to improve the system design and reliability.

Chapter 5
Performance evaluation of an integrated small-scale SOFC-biomass gasification power generation system

5.1 Introduction

In this chapter, the integration of a biomass gasification and 5kW-class SOFC power system is evaluated through numerical models presented in Chapter 3. The biomass fuel considered in this study is represented by ash-free typical wood fuel formula of $CH_{1.4}O_{0.59}N_{0.0017}$[22]. A sensitivity analysis was carried out to achieve a better understanding of the influence of key parameters e.g. steam to biomass ratio (STBR), SOFC inlet stream temperatures, fuel utilization factor (U_f) and anode off-gas recycle ratio (AGR) on the performance of key system components. By performing energy and exergy analysis, the causes of exergy losses were revealed to identify the areas of improvement of the combined system. Due to the fact that SOFC stack is accounted for the most expensive part of the initial investment cost, the number of cells required for SOFC stack is also taken into consideration as well.

5.2 System configuration and description

The schematic of the integrated SOFC-biomass gasification power generation system in this study is shown in Fig. 5-1. A DIR-SOFC, capable of internal reforming of the methane in the syngas into hydrogen, was developed in Section 3.1. While, biomass gasifier model was developed and validated in Section 3.2. The other peripheral components include three gas-to-gas heat exchangers (HX1, HX2 and HX3), heat recovery steam generator (HRSG), burner, pump, fuel and air compressors are thermodynamically modeled under steady state operational conditions.

In the integrated system, depleted fuel and air from the cell stack were combusted in the burner and supplied heat to wet biomass drying process to upgrade the heating value of the produced gas called “syngas”. The steam from drying process is mixed with additional steam and air and then directed to gasification process. The syngas produced by gasification generally contains some amount of tar, sulfur and other contaminants that may lead degradation of SOFCs. Consequently, a hot gas clean up is facilitated. After syngas is cleaned through hot gas cleaning unit, the fuel stream is cooled down in HX1 by preheating the air, then entering a fuel compressor served as suction blower to overcome pressure drops in the gasifier and SOFC systems. To prevent the carbon deposition in the SOFC, before clean syngas entering the cell, the steam-to-carbon ratio is set at 2 [64] by adjusting the external steam from HRSG and anode off-gas recycle ratio (AGR). The SOFC air and fuel streams are preheated by the cathode and anode off-gas in HX2 and HX3 and are heated up to 973 K. An inverter is also used in the system to convert the DC power output of the SOFC stack into AC power output. The HRSG uses the heat from the flue gas to generate steam for the gasification and SOFC anode gas moistening. The flue gas is released to the environment at atmospheric pressure and cooled down to 373 K. For all of the HXs and the HRSG, 2% heat losses of heat transferred are assumed. Possible variations in pressure drops across each unit operation are assumed 2%, except in SOFC is assumed 3%.

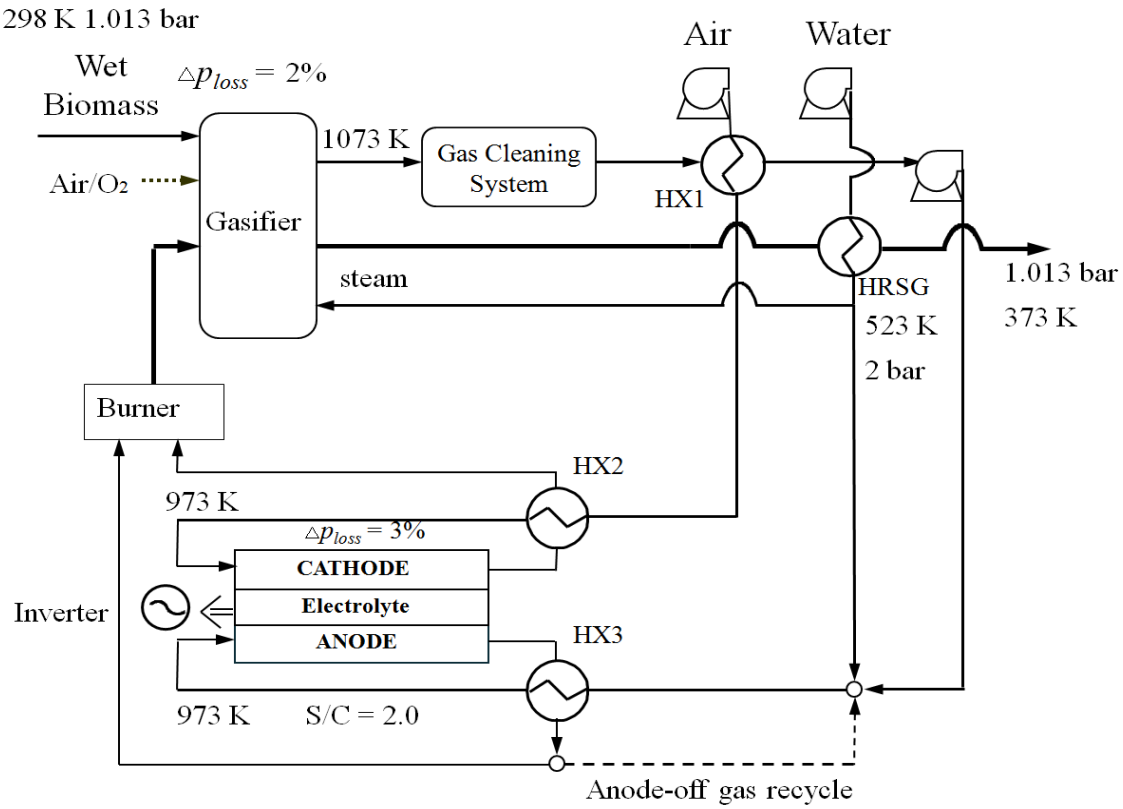

Fig. 5-1: Schematic flow diagram of an integrated SOFC-biomass gasification power generation systems.

5.3 Computational condition

To understand the operational scenarios of the integrated SOFC-biomass gasification power generation system, an independent parameter analysis of a single component is not enough to assess the whole system because each component in the system affects one another. In this study, sensitivity analysis is used to quantify the effects of STBR, SOFC inlet stream temperatures, U_f and AGR on SOFC, gasifier and system performances as well as the size of SOFC stack. The input operational parameter values, as presented in Table 5-1, are used as constant throughout the study unless mentioned specifically.

Table 5-1: Operational parameter values for the base case system.

Parameters	Value
Biomass fuel data	
Biomass composition (dry, ash-free basis)	$CH_{1.4}O_{0.59}N_{0.0017}$
Moisture content (-)	0.2
$LHV_{biomass}$ (kJ kg^{-1}, wet basis)	15455
Gasifier input data	
Gasifier operational temperature (K)	1073
Steam to biomass ratio (- , wet basis)	1.5
Air inlet temperature to gasifier (K)	298
Steam input temperature (K)	523
System input data	
Total electrical net output power (kW)	5
Anode off-gas recycle ratio AGR (-)	0
Fuel utilization factor U_f (-)	0.75
Air utilization factor U_a (-)	0.35
Exhaust gas temperature (K)	373
Pump isentropic efficiency η_{pump} (-)	0.95
Air compressor isentropic efficiency $\eta_{air,c}$ (-)	0.75
Fuel compressor isentropic efficiency $\eta_{fuel,c}$ (-)	0.75
Pump mechanical efficiency $\eta_{pump,me}$ (-)	0.98
Air compressor mechanical efficiency $\eta_{air,c,me}$ (-)	0.98
Fuel compressor mechanical efficiency $\eta_{fuel,c,me}$ (-)	0.98
Inverter efficiency η_{inv} (-)	0.95
Stack input data	
Average current density ($A\ m^{-2}$)	4000
Number of channel per SOFC cell	20
Air inlet temperature to the SOFC $T_{air,in}$ (K)	973
Fuel inlet temperature to the SOFC $T_{fuel,in}$ (K)	973
Steam-to-carbon ratio STBR (-)	2.0
Cell length (mm)	100.0
Channel width (mm)	5.0
Air channel height (mm)	1.5
Fuel channel height (mm)	0.4
Anode thickness (μm)	500.0

Cathode thickness (mm)	50.0
Electrolyte thickness (μm)	10.0

In order to determine how much each component contributes to the total irreversibility of the plant, exergy analysis in every branch of the plant is performed and the results corresponding to the base case system in Table 5-1 are shown in Fig. 5-2. The results show that the largest exergy destruction rate occurring in the gasifier is 4.20 kW or 44.0% of the total exergy destruction rates mainly caused by intrinsic irreversibility. The SOFC is also responsible for large exergy destruction, which is 2.63 kW mainly due to irreversibilities associated with the electrochemical reactions. Figure 5-2 shows that the burner, HRSG, HX1 and HX3 are responsible for 13.6, 8.5, 2.5 and 2.1% of the total exergy destruction rate, respectively, and those of the other system components account for less than 1% of the total exergy destruction rate. This implies that the exergy losses in gasifier and SOFC are two central units with larger exergy losses than the other sections. Therefore, the SOFC and gasifier are key elements to the improvement of system efficiency.

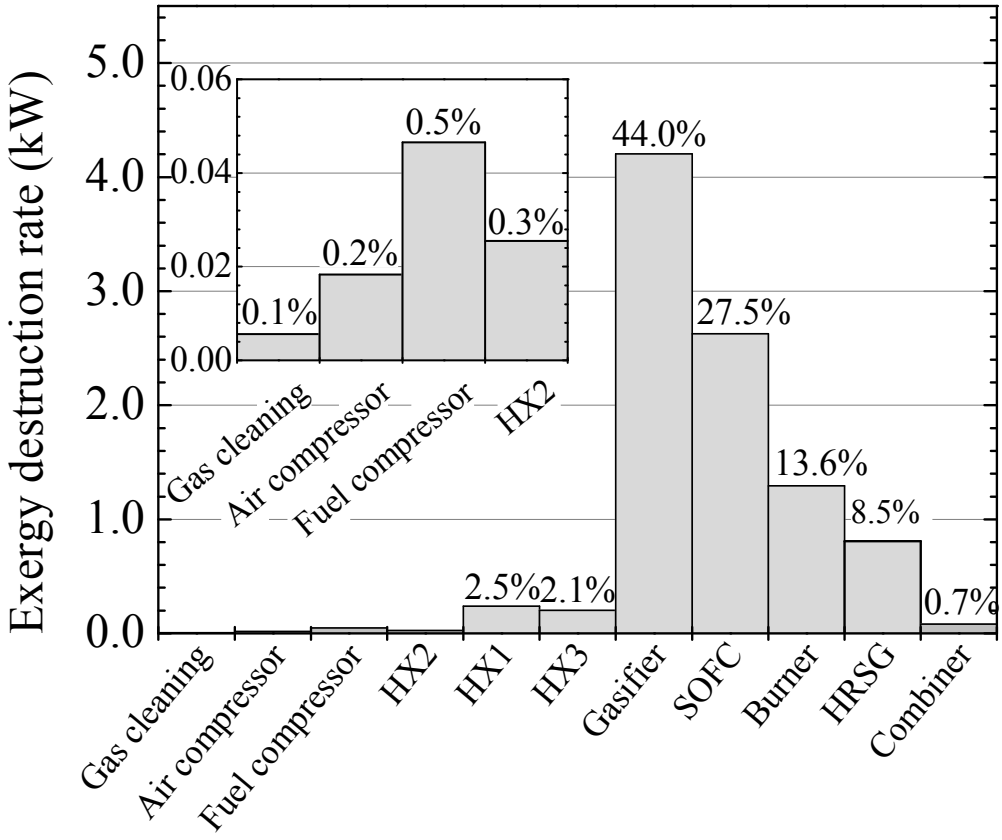

Fig. 5-2: Local exergy destruction rates of the base case system.

5.4 Influence of steam-to-biomass ratio (STBR)

The gasifier operating temperature is kept constant at 1073 K in all of the case studies, while the small portion of air is adjusted to maintain the set gasification temperature. Among various gasification agents, steam gasification is the most energy demanding process. In this study, steam and air are added, while exhaust gas supplies direct heat for biomass drying to achieve a high thermodynamic efficiency. As shown in Fig. 3-4, the syngas produced in four STBR study cases (0.5, 1.0, 1.5 and 2.0) locate below the carbon boundary to avoid carbon deposition. Modeling results summarized in Table 5-2 show that addition of steam yields steam-rich syngas, thus lowering the LHV of species and the cold gas efficiency. The increase of STBR results in a rapid decrease of CO concentration in the produced syngas due to shift reaction. It should be noted that the increasing steam content in syngas also reduces in the amount of external steam used for raising steam-to-carbon ratio in the SOFC feed gas to 2 [64]. To illustrate how STBR affects SOFC, gasifier and system performances and the number of cells, Fig. 5-3 is plotted and shows their sensitivity to STBR with the variation from 0.5 to 2.0. As can be seen in Fig. 5-3(a), the SOFC energetic and rational efficiencies change from 39.9 to 43.1% and 55.6 to 67.0%, respectively. The optimized STBR is 1.5 when SOFC energetic and rational efficiencies are the maximum of 43.5 and 67.3%, respectively. As shown in Fig. 5-3(b), increasing STBR deteriorates cold gas efficiency from 80.8 to 73.4% mainly due to steam dilution of the produced syngas, while gasifier rational efficiency shows insignificant change. The gasifier rational efficiencies are approximately 77%. The effects of STBR to overall system performance is shown in Fig. 5-3(c) that with increasing STBR, overall system and rational efficiencies varies from 35.1 to 37.9% and 33.9 to 36.8%, respectively. However, the difference of the system performance between STBR of 1.5 and 2.0 is negligibly small. Since the required number of cell corresponds to overall system efficiency, as shown in Fig. 5-3(d), the smallest required number of cell of 173 was found at STBR of 1.5 when the overall system efficiency was maximized.

Table 5-2: Gas compositions after the gas cleaning system for different steam to biomass ratios and heating values.

Syngas compositions (vol %, wet basis) @ 1073 K				
STBR	**0.5**	**1.0**	**1.5**	**2.0**
ER	**0.089**	**0.088**	**0.096**	**0.095**
H_2	0.355	0.332	0.291	0.263
CO	0.263	0.162	0.106	0.076
CO_2	0.107	0.135	0.141	0.136
CH_4	0.008	0.009	0.008	0.008
H_2O	0.132	0.255	0.357	0.434
N_2	0.135	0.108	0.098	0.084
LHV (MJ Nm^{-3})	8.576	7.960	7.414	7.203

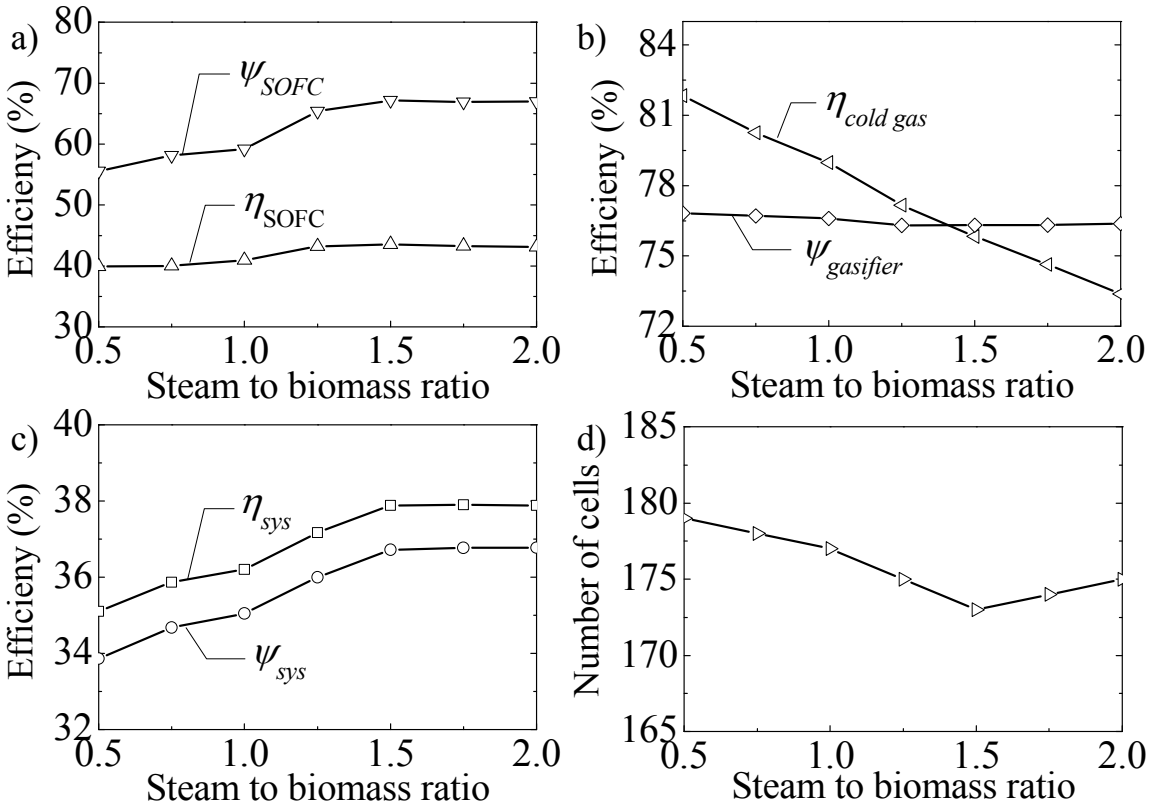

Fig. 5-3: Influence of steam-to-biomass ratios on (a) SOFC energetic and rational efficiencies, (b) cold gas and gasifier rational efficiencies, (c) overall system and system rational efficiencies, and (d) the required number of SOFC cells.

5.5 Influence of SOFC inlet stream temperatures

The SOFC inlet stream temperatures are key design parameters of a system, because they affect the temperature distribution through heat transfer phenomena in the SOFC and eventually affect its performance [4]. To safely operate SOFC system and to obtain high system efficiency, the SOFC cell temperature distributions should be monitored to avoid severe operating condition. SOFC performance under co-flow operation is chosen in this study, because it generally has more uniform temperature distribution than other flow configurations [65]. The cell temperature distributions of the four cases are shown in Fig. 5-4. The four stream inlet temperatures are 923, 973, 1023, and 1073 K. In this study, the maximum allowable temperature gradient and the maximum allowable cell temperature, well known as the most important operational constraints for the planar SOFC, are set at 1400 K and 5 K/mm, respectively, following Stiller et al. [4]. The SOFC cell temperature profiles for the four different SOFC inlet stream temperature cases are depicted in Fig. 5-4. The electrochemical oxidation of H_2 and the shift reaction are the major reactions proceed in the fuel passage and release reaction heat resulting in the cell temperature rising near the gas inlets. Fig. 5-4 shows that the peaks of the cell temperature profiles move toward channel inlets as the stream inlet temperatures increase. The maximum cell temperatures ($T_{solid,max}$) and the maximum cell temperature gradients $(\partial T_{solid}/\partial x)_{max}$ corresponding to Fig. 5-4 are listed in Table 5-3. Although, in Table 5-3, all case studies operate safely under the material constraints, the most favorable SOFC operating condition is at SOFC inlet stream temperatures of 973 K when maximum temperature gradient is the smallest. Figure 5-5 shows the influence of SOFC inlet stream temperatures on SOFC, gasifier and system performance and the number of cells. As shown in Fig. 5-5(a), with the increase of SOFC inlet temperature from 923 to 1073 K, the SOFC energetic efficiency increases from 42.5 to 44.3%, while SOFC rational efficiency drops from 67.4 to 64.6%. On the other hand, in Fig. 5-5(b), the increase of SOFC inlet stream temperatures decreases cold gas and gasifier rational efficiencies from 77.4 to 74.4% and from 76.5 to 74.5%, respectively. This reduction in gasifier performance is accounted for by the decrease of exhaust heat, which is partially used for air and fuel pre-heaters in order to raise inlet stream temperatures of the stack. In Fig. 5-5(c), as the SOFC inlet stream temperatures increase, the overall system and system rational efficiencies decrease monotonously from 38.2 to 36.2% and from 37.1 to 35.0%, respectively, owing to prominent losses in gasifier. The study also shows in Fig. 5-5(d) the highest system performance at SOFC inlet stream temperatures of 923 K required the highest number of cell of 179, when the smallest number of cells is 169 at

the highest SOFC inlet temperature.

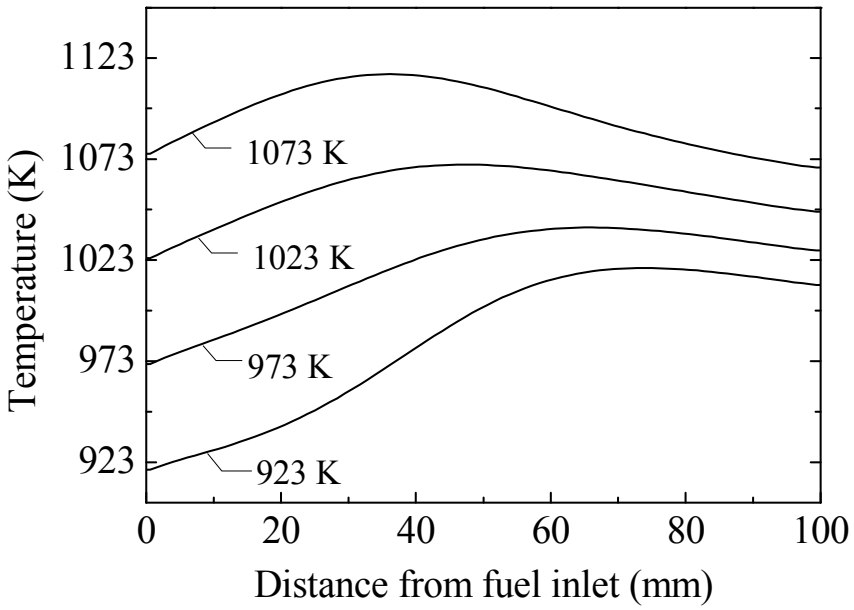

Fig. 5-4: The SOFC cell temperature profiles for different SOFC inlet stream temperatures.

Table 5-3: SOFC performance comparison on SOFC inlet temperature effects.

$T_{fuel,in}$ (K)	$T_{air,in}$ (K)	$T_{solid,max}$ (K)	$(\partial T_{solid}/\partial x)_{max}$ (K mm^{-1})
923	923	1392	2.22
973	973	1312	1.41
1023	1023	1293	1.62
1073	1073	1388	1.76

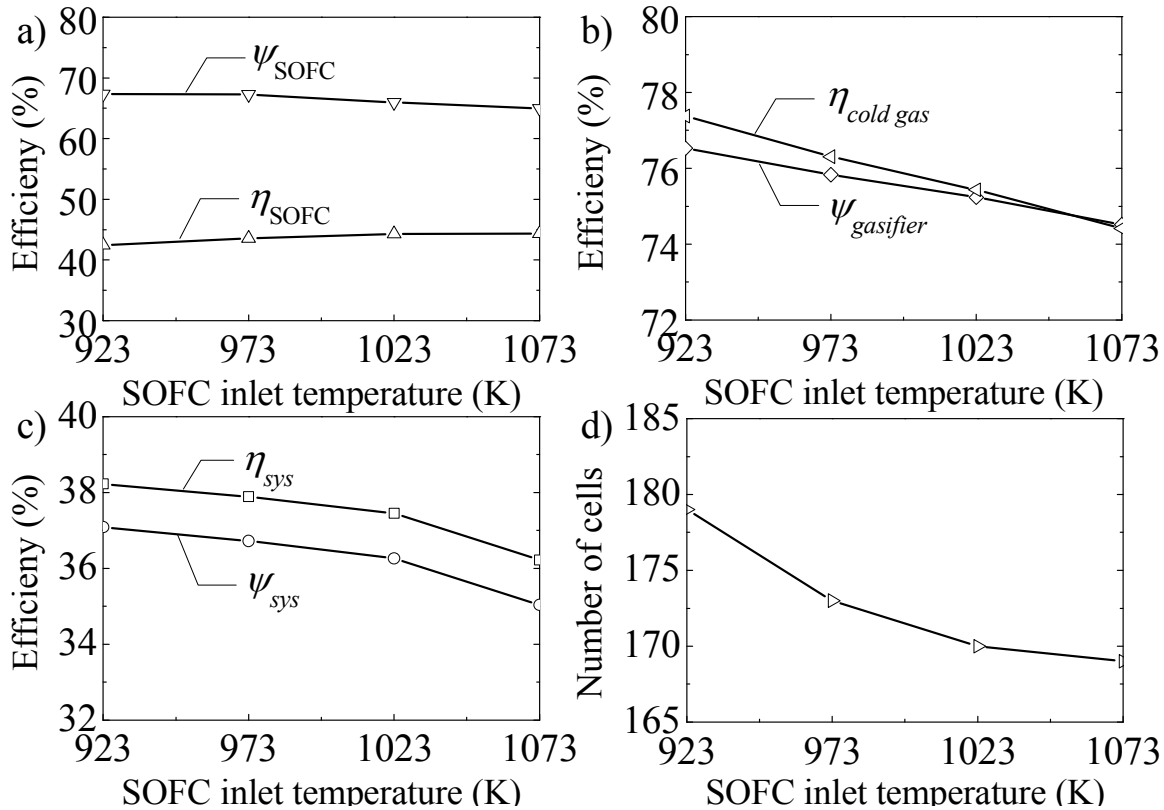

Fig. 5-5: Influence of SOFC inlet stream temperatures STBR on (a) SOFC energetic and rational efficiencies, (b) cold gas and gasifier rational efficiencies, (c) overall system and system rational efficiencies, and (d) the required number of SOFC cells.

5.6 Influence of fuel utilization factor (U_f)

The fuel utilization factor (U_f) is an important parameter, which is closely related to the performance of SOFC and exhaust heat reflecting the gasifier performance. The proper amount of exhaust heat and unreacted fuel from electricity conversion process results in the efficient thermochemical conversion of biomass. The influence of U_f on SOFC, gasifier and system performance and the number of cells is shown in Fig. 5-6. As shown in Fig. 5-6(a), SOFC energetic efficiency increases monotonously from 32.5 to 48.8%, with the increase of U_f from 0.65 to 0.90. This is due to the fact that as the U_f is enhanced, electrochemical reaction rates increase, thus raising the electrical power output per cell. However, by considering exergy in the outgoing streams, SOFC rational efficiency is the maximum of 67.3% at the fuel utilization factor of 0.75. As can be seen in Fig. 5-6(b), with increasing U_f from 0.65 to 0.90, cold gas and gasifier rational efficiencies decrease monotonously from 83.2 to 71.5% and 79.7 to 72.3%, respectively. When the fuel utilization factor increases the heat generation in burner decreases and

consequently the exhaust heat utilized in the gasifer becomes lower leading to dilution of syngas by N_2. The reductions of gasifier efficiencies are mainly due to poor quality syngas generated. The optimum fuel utilization factor of 0.75 for the system performance is shown in Fig. 5-6(c), where the overall system and system rational efficiencies are the highest at 37.9 and 36.7%, respectively. As can be seen in Fig. 5-6(d), at the fuel utilization factor of 0.75, the number of cells is the lowest of 173 among the cases studied. This is mainly due to the compensation between quality of syngas and SOFC efficiencies.

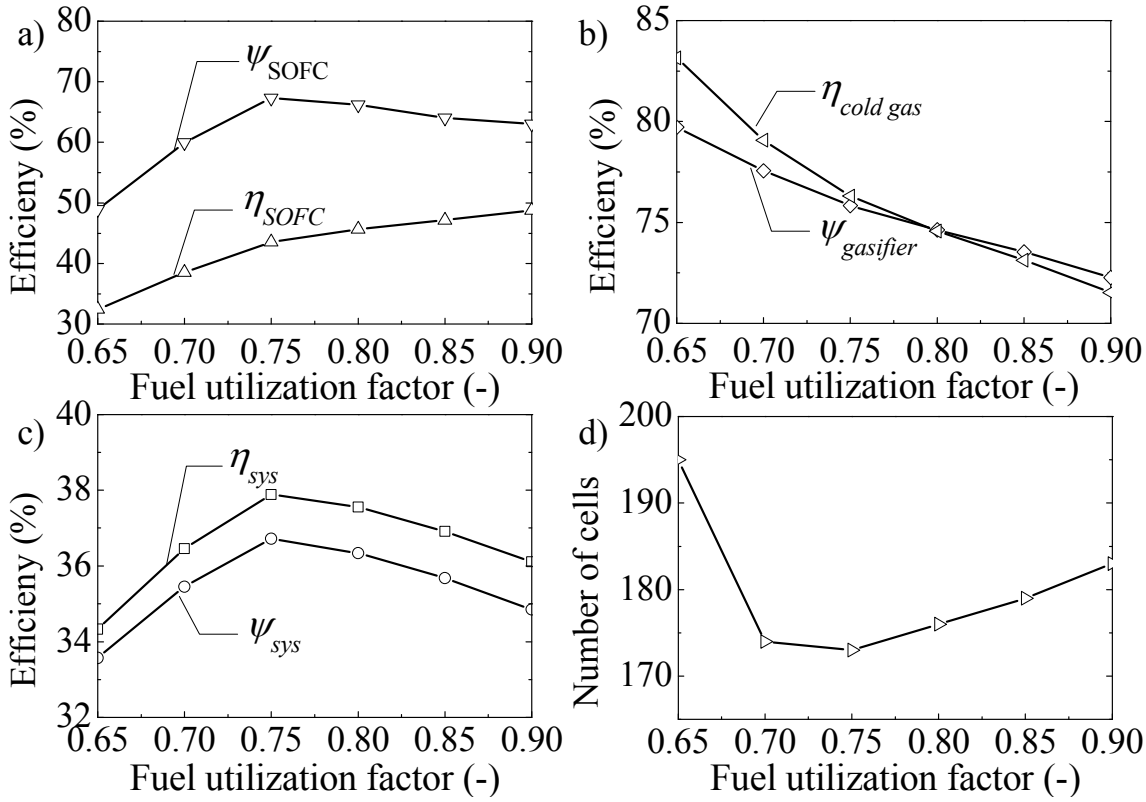

Fig. 5-6: Influence of fuel utilization factor on (a) SOFC energetic and rational efficiencies, (b) cold gas and gasifier rational efficiencies, (c) overall system and system rational efficiencies, and (d) the required number of SOFC cells.

5.7 Influence of anode off-gas recycle ratio (AGR)

Anode off-gas recycle is functioned to recirculate steam from anode off-gas to reduce the amount of external steam and also to bring up the SOFC fuel inlet temperature. By reducing the amount of external steam, more heat can be used to dry and preheat a wet feedstock before entering gasifier, resulting in increased gasifier efficiency. Figure 5-7

demonstrates the modeling results of the influence of AGR on SOFC, gasifier, system performance and the number of cells. As can be seen in Fig. 5-7(a), with the variation of AGR from 0 to 0.8, the energetic efficiency of SOFC slightly decreases from 43.5 to 41.3% due to dilution effect of the hydrogen content in fuel stream, while variation in rational efficiency of SOFC is very insignificant approximately 67.3%. In Fig. 5-7(b), when AGR increases from 0 to 0.8, the cold gas and gasifier rational efficiencies increase from 75.8 to 77.2% and 75.3 to 78.4%, respectively. The optimum performance for the combined system (η_{sys} = 38.9%, ψ_{sys} = 37.4%) is achieved at AGR of 0.6. Form an economic point of views, increasing AGR leads to increasing capital cost. Figure 5-7(d) shows the number of cells increasing from 173 to 182 cells by implementing AGR of 0.8, mainly due to the decrease in SOFC energetic efficiency.

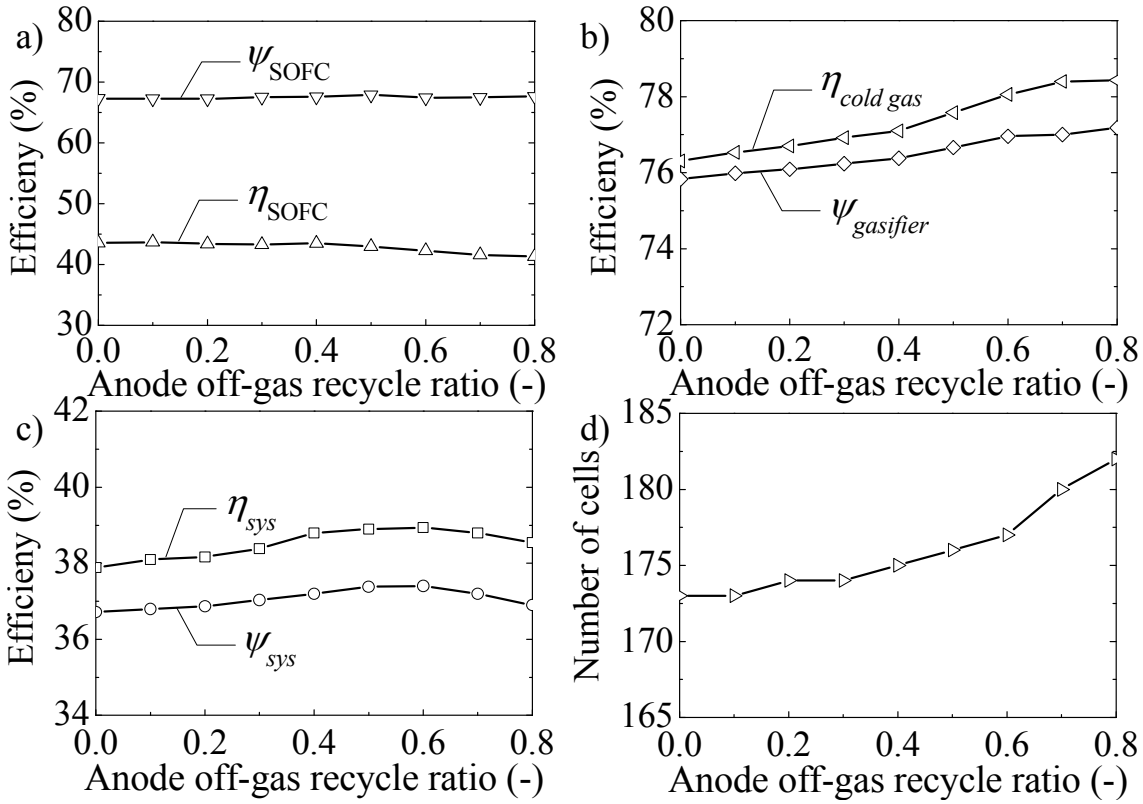

Fig. 5-7: Influence of anode off-gas recycle ratio on (a) SOFC energetic and rational efficiencies, (b) cold gas and gasifier rational efficiencies, (c) overall system and system rational efficiencies, and (d) the required number of SOFC cells.

5.8 Summary

In this chapter, an integrated 5kW SOFC-biomass gasification power generation system has been investigated. In order to achieve reliable results, the SOFC and gasifier model were validated against published data. Sensitivity analyses were carried out in order to give insight into the influence of the main variables on the system. The main parameters concerning the integration of SOFC technology and thermal process of biomass gasification are STBR, SOFC inlet stream temperatures, U_f and AGR. Their effects on SOFC, gasifier and system performances are investigated. In order to assure economically competitive of the combined system, the number of cells required for SOFC stack is also taken into consideration. From the analysis, the following conclusions are made:

1. The increase of STBR shows positive effect of the performance of SOFC and the system while at STBR higher than 1.5 the effect becomes adverse. With the minimum number of SOFC cell and the highest system performance, the STBR was optimized at 1.5.
2. Increasing SOFC inlet stream temperatures reduce to the amount of exhaust heat used for biomass gasification process leading to rapid decline of gasfier efficiencies.
3. In the system studied, the fuel utilization factor of 0.75 is the optimum, when the number of cells is the lowest and the system efficiencies are the highest due to the optimal balance of the plant condition.
4. Anode-off gas recycle can boot the combine system performance, but at the same time the higher the AGR also requires bigger SOFC stack. The optimal performance of the combined system (η_{sys} = 38.9%, ψ_{sys} = 37.4%) is achieved at AGR of 0.6

Chapter 6
Performance evaluation of a direct-biogas solid oxide fuel cell-micro gas turbine (SOFC-MGT) hybrid combined heat and power (CHP) system

6.1 Introduction

In this chapter, results and discussion of a direct-biogas SOFC-micro gas turbine (MGT) hybrid CHP system with an electrical power output of 200 kW_e are presented. Energy and exergy analyses were used to determine the causes of exergy losses and identify areas in need of improvement while adhering to material thermal constraints. Attention was paid to the influence of air-steam mixtures as reforming agents on the direct internally reformed SOFC stack as well as on the SOFC-MGT hybrid CHP plant. The other key operating parameters considered in this study were fuel utilization factor (U_f), turbine inlet temperature (TIT), and compression ratio. The influence of variation in operating parameters on plant performance was evaluated for the overall system and SOFC efficiencies as well as the thermal energy to electric power ratio (TER) and the power ratio of MGT to SOFC (P_{MGT}/P_{SOFC}). Because of the fact that the SOFC stack is the most expensive part in the initial investment cost, the number of cells required in the SOFC stack was also taken into consideration.

6.2 System configuration and description

A schematic of the direct-biogas SOFC-MGT hybrid CHP system used in this study is shown in Fig. 6-1. In the integrated system, because the SOFC does not operate at 100% fuel utilization, a burner is needed to combust excess and additional fuel to elevate the TIT to a specified range for optimum system performance. Then, the products of the burner expand in the turbine and the exhausted gas is further utilized by HX1 and HRSG. Before the flue gas is released into the environment at atmospheric pressure, it is cooled to 373 K, producing useful heat. The SOFC air and fuel streams are preheated by the cathode and anode off-gases in HX2 and HX3 and are heated up to 1073 K. An inverter is also used in the system to convert the DC power output of the SOFC stack into AC power output. To prevent carbon deposition in the SOFC, biogas is mixed with air and/or steam before it enters the cell. An HRSG is integrated at the MGT exhaust outlet, supplying a predetermined amount of steam while a small amount of air from an air pump is mixed with the fuel. For all of the HXs and the HRSG, 2% heat losses of heat transferred are assumed. Possible variation in pressure drop across each component is assumed to be 2%, except in the SOFC, where it is assumed to be 3%.

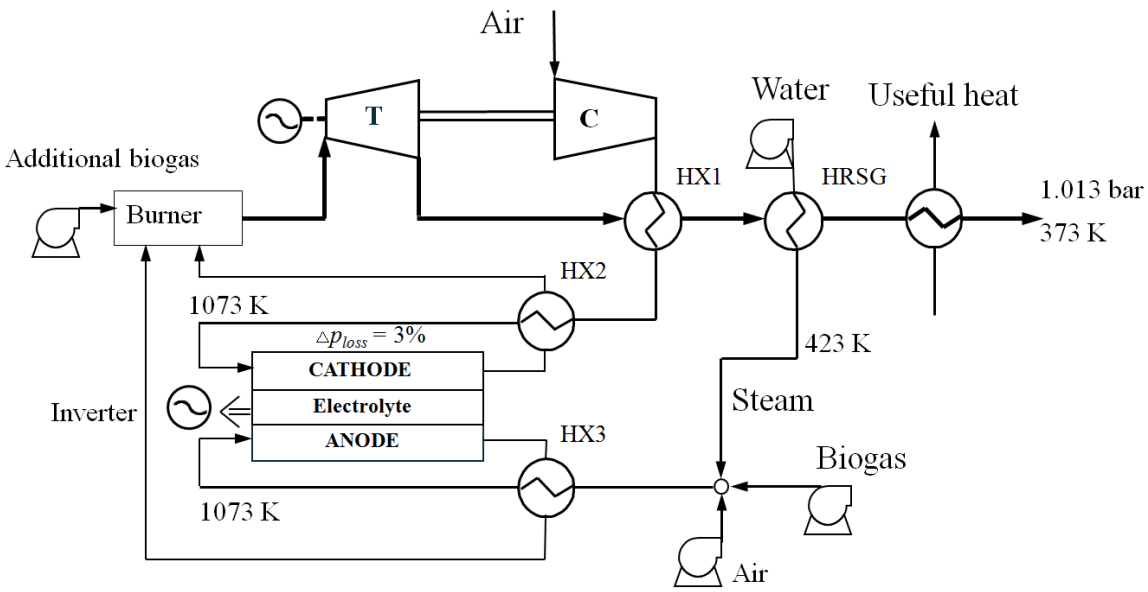

Fig. 6-1: Schematic flow diagram of the direct-biogas SOFC-MGT hybrid CHP system.

6.3 Computational condition

Because the SOFC stack is considered the central part of the hybrid system, the simulation results are presented in two parts. First, the performance of the biogas-fed SOFC operated at atmospheric pressure utilizing different reforming agents (steam and combined air/steam) was investigated via thermodynamic analysis to determine the most suitable feed, using the operational parameter values listed in Table 6-1. SOFC performance under co-flow operation was also analyzed because it generally has a more uniform temperature distribution than other flow configurations [65]. These results are discussed first. The second part presents the sensitivity analysis of the direct-biogas SOFC-MGT hybrid CHP system shown schematically in Fig. 6-1. To understand the operational scenarios of the hybrid CHP system, an independent parameter analysis of a single component is not enough to assess the whole system, because all components in the system affect one another. The input operational parameter values for the SOFC and the other system components presented in Tables 6-1 and 6-2 were used as constants throughout the study, unless indicated otherwise.

Table 6-1: Operational parameter values for the SOFC simulation.

Parameters	Value
Biogas	CH_4 60% : CO_2 40%
Stack input data	
Fuel utilization factor U_f (-)	0.75
Air utilization factor U_a (-)	0.25
Average current density (A m^{-2})	4000
Number of channels per SOFC cell	20
Air inlet temperature to the SOFC $T_{air,in}$ (K)	1073
Fuel inlet temperature to the SOFC $T_{fuel,in}$ (K)	1073
Cell length (mm)	100.0
Width covered by one channel (mm)	5.0
Air channel height (mm)	1.5
Fuel channel height (mm)	0.4
Anode thickness (μm)	500
Cathode thickness (μm)	50
Electrolyte thickness (μm)	10

Table 6-2: Operational parameter values for system simulation.

Parameters	Value
Total electrical net output power (kW_e)	200
Steam-to-carbon ratio (-)	2
Compression ratio (-)	8
Turbine inlet temperature TIT (K)	1073
Exhaust gas temperature (K)	373
Pump isentropic efficiency η_{pump} (-)	0.95
Air compressor isentropic efficiency $\eta_{air,c}$ (-)	0.75
Fuel compressor isentropic efficiency $\eta_{fuel,c}$ (-)	0.75
Turbine isentropic efficiency η_t (-)	0.85
Pump mechanical efficiency $\eta_{pump,me}$ (-)	0.98
Air compressor mechanical efficiency $\eta_{air,c,me}$ (-)	0.98
Fuel compressor mechanical efficiency (-)	0.98
Turbine mechanical efficiency (-)	0.98
Inverter efficiency η_{inv} (-)	0.95

The inlet gas compositions are determined by considering the carbon-hydrogen-oxygen (C-H-O) ternary diagrams shown in Fig. 6-2. In principle, it is feasible to directly feed biogas containing the natural reforming agent, CO_2, into a high-temperature SOFC without an additional reforming agent. However, in regard to the most common form of biogas considered in this work (represented by 60% CH_4 and 40% CO_2 in volume), biogas lies above the carbon deposition boundary curves, indicating that solid carbon exists in heterogeneous equilibrium. The location of biogas may be moved below the carbon deposition boundary by adding steam or oxygen. As clearly shown in Fig. 6-2, an increase in steam or oxygen as a reforming agent for methane in biogas can minimize the risk of carbon deposition. In this study, six different inlet gas compositions were examined. Cases I and VI are shown in Fig. 6-2; the others (cases II–V) are not shown in the figure but are located somewhere between these two points. Detailed gas compositions are explained in the next section.

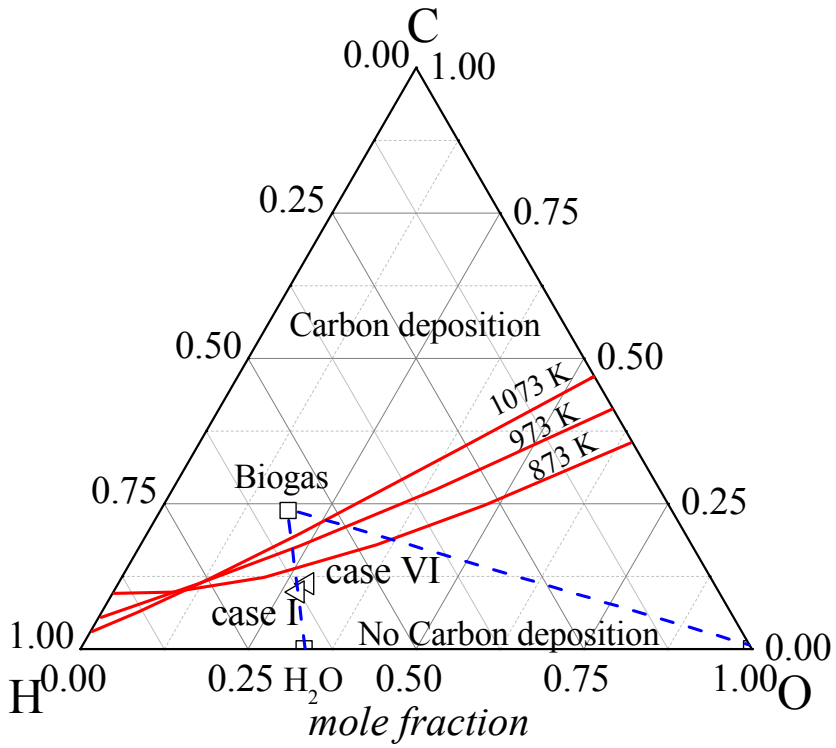

Fig. 6-2: C-H-O ternary diagram with a carbon deposition boundary at 1073, 973, and 873 K and 1 atm.

6.4 Direct-biogas SOFC simulation

A strong endothermic reaction due to the presence of steam can lead to local temperature gradients, especially near the entrance of the stack, resulting in mechanical failure due to thermally induced stress. In this study, the maximum allowable temperature gradient and the maximum allowable cell temperature, which are the most important operational constraints for a planar SOFC, were set to 1300 K and 5 K mm^{-1}, respectively, following Stiller et al. [4]. Table 6-3 presents the sensitivity of the system to different ratios of air and steam to fuel for cases I–VI, illustrating how reforming agents may affect SOFC performance. As mentioned in the previous section, anode feed gases were located below the carbon deposition boundary in all cases. As shown in Table 6-3, an increase in air input into the anode deteriorated the SOFC energetic and rational efficiencies from 50.8% to 47.4% and from 72.3% to 70.0%, respectively, mainly due to partial oxidation. The SOFC cell temperature profiles for the six different ratios of air and steam to fuel are depicted in Fig. 6-3. The presence of oxygen caused the cell temperature near the channel inlets to rise, and consequently accelerated the

strong endothermic reactions that take place during the steam reformation of methane. As the steam-reforming reaction rate increases, the cell temperature drops more rapidly and the cell temperature gradient becomes steeper near the channel inlets. The maximum cell temperatures ($T_{solid,max}$) and the maximum cell temperature gradients $(\partial T_{solid}/\partial x)_{max}$ corresponding to Fig. 6-3 are listed in Table 6-3. According to the table, only cases I–IV led to safe operation of the system under the material constraints. The most favorable operating conditions were in case I, which had the lowest maximum temperature gradient and the highest energetic (η_{SOFC}) and rational efficiencies (ψ_{SOFC}). It should be noted, however, that a high exhaust gas temperature is favorable for hybrid operation. The effects of reforming agents on the hybrid CHP system are discussed later in this report.

Table 6-3: Summary of SOFC performance at atmospheric pressure based on different SOFC reforming agents.

Case	biogas:steam:air	η_{SOFC} (%)	ψ_{SOFC} (%)	$T_{solid,\ max}$ (K)	$(\partial T_{solid}/\partial x)_{max}$ (K mm^{-1})
I	1:2.0:0.0	50.8	72.3	1077.1	1.6
II	1:1.9:0.1	50.2	71.9	1081.5	2.4
III	1:1.8:0.2	49.6	71.5	1086.3	3.3
IV	1:1.7:0.3	48.9	71.2	1091.1	4.3
V	1:1.6:0.4	48.0	70.7	1096.2	**5.4**
VI	1:1.5:0.5	47.4	70.0	1101.7	**6.5**

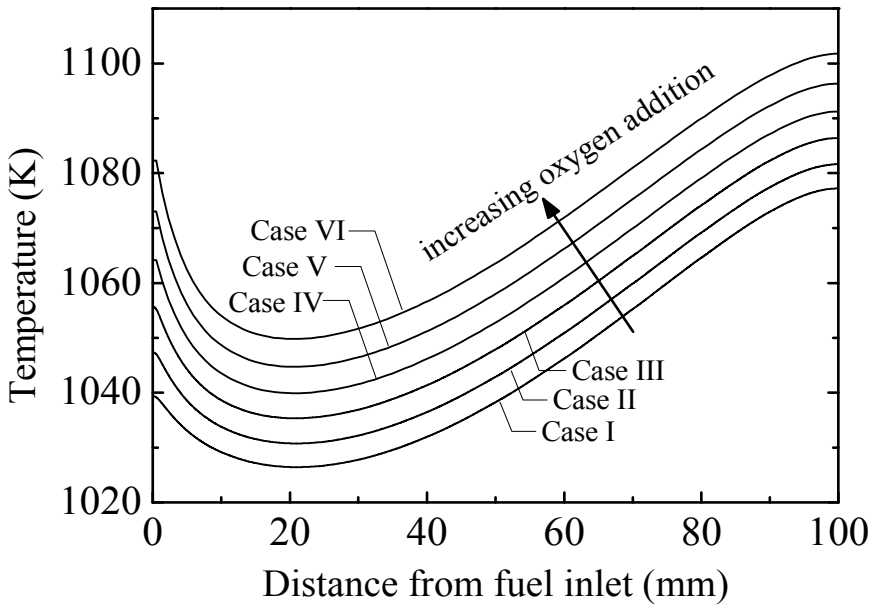

Fig. 6-3: SOFC cell temperature profiles for different air-steam mixtures as SOFC reforming agents.

6.5 System simulation

A sensitivity analysis was used to quantify the effects of air-steam mixtures as reforming agents, U_f, TIT, and the compression ratio on system performance and the size of the SOFC stack.

6.5.1 Influence of air-steam mixtures as reforming agents

The efficiencies of the direct-biogas SOFC-MGT hybrid CHP system under various air-steam mixtures as reforming agents (anode feed gas compositions of cases I–V in Table 3) are depicted in Fig. 6-4. As the amount of air input increased, both the energetic (η_{SOFC}) and the rational efficiencies (ψ_{SOFC}) decreased, while the exhaust heat from the SOFC increased. This compensated for the drop in electrical power produced by the SOFC stack. These results suggest that air-steam mixtures have only slight effects on system electrical efficiency ($\eta_{ele,syn}$), system CHP efficiency (η_{CHP}), and rational CHP efficiency (ψ_{CHP}). The effects of air-steam mixtures as reforming agents on the required number of SOFC cells, the output power ratio of MGT to SOFC (P_{MGT}/P_{SOFC}), and the TER of the direct-biogas SOFC in the hybrid CHP system are shown in Fig. 6-5. At an air to biogas ratio of 0.4, the required number of cells decreased by approximately 4%, whereas P_{MGT}/P_{SOFC} increased from 0.37 to 0.40. As more air was added, TER increased from 0.38 to 0.41 owing to more heat energy in the

SOFC off-gases going to the MGT system, leading to a reduction in the fuel fed to the burner. It should be noted that only the anode feed gas composition of case I was used for the rest of the system evaluation.

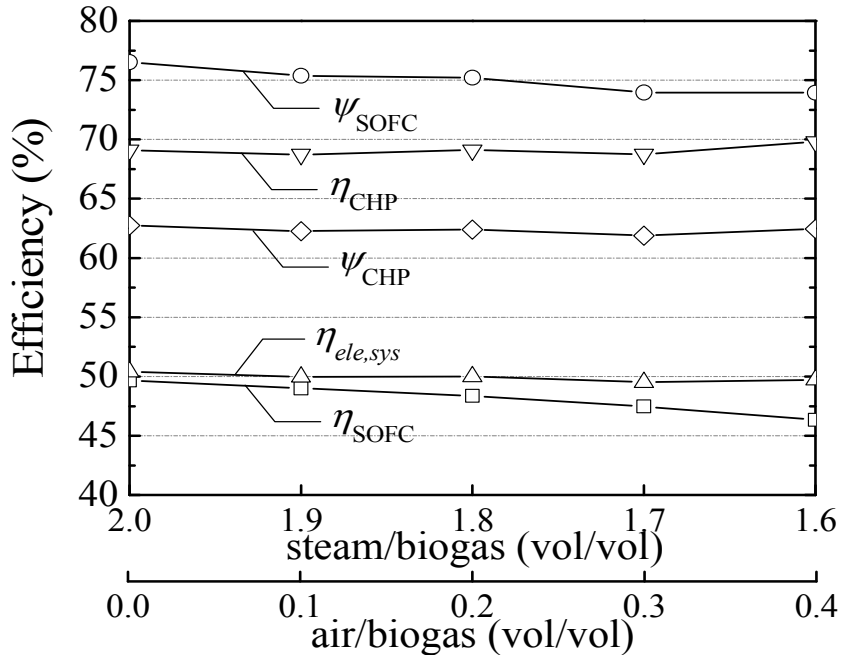

Fig. 6-4: Influence of air-steam mixtures as reforming agents on SOFC and system efficiencies.

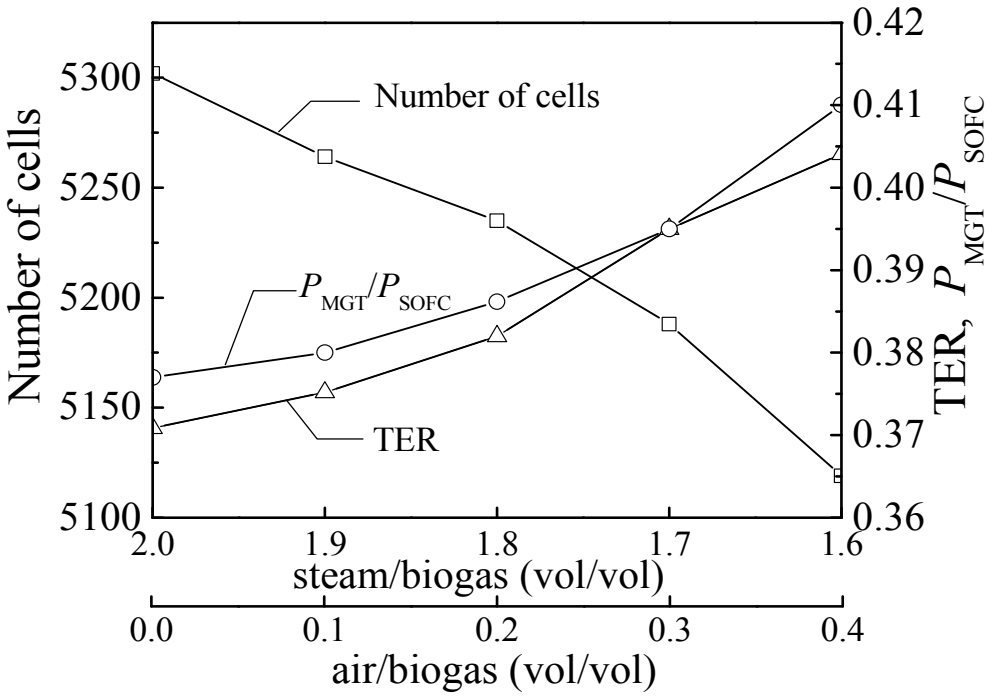

Fig. 6-5: Influence of air-steam mixtures as reforming agents on P_{MGT}/P_{SOFC}, TER, and the required number of SOFC cells.

6.5.2 Influence of fuel utilization factors (U_f)

The U_f of a commercial SOFC is 75–85% [66]. The fuel utilization factor is an important parameter, which is closely related to the performance of SOFCs and exhaust heat, reflecting the performance of hybrid CHP systems. The proper amounts of exhaust heat and unreacted fuel from the electricity conversion process result in an efficient GT cycle. The influence of U_f on SOFC and system performance is shown in Fig. 6-6. As U_f increased from 0.65 to 0.90, SOFC energetic efficiency (η_{SOFC}) increased from 42.3% to 59.8%. This is due to the fact that as U_f is enhanced, electrochemical reaction rates increase, thus raising the electrical power output produced by the SOFC stack. However, when considering exergy in the outgoing streams, the SOFC rational efficiency peaked at 76.7% when U_f was 0.75. The influence of U_f on the required number of SOFC cells, P_{MGT}/P_{SOFC}, and TER is presented in Fig. 6-7. At a U_f of 0.75, the required number of cells was lowest (5,277) among all of the cases studied. This is mainly due to compensation between the electrical power produced by the MGT and the SOFC. As U_f changed from 0.65 to 0.90, P_{MGT}/P_{SOFC} dropped from 0.41 to 0.36, owing to a considerable increase in the SOFC efficiency. When U_f increases, it results in less unused fuel in the anode exhaust, and consequently, more additional fuel is needed to maintain the set TIT. At the same time, TER increased from 0.34 to 0.40, because the amount of heat in flue gas increased as the amount of additional fuel fed to the burner increased.

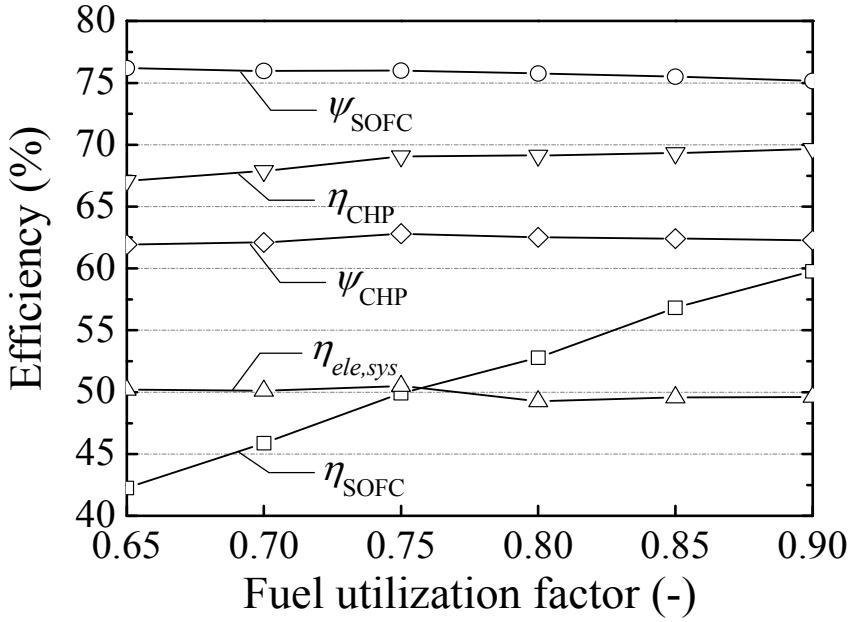

Fig. 6-6: Influence of the fuel utilization factor on SOFC and system efficiencies.

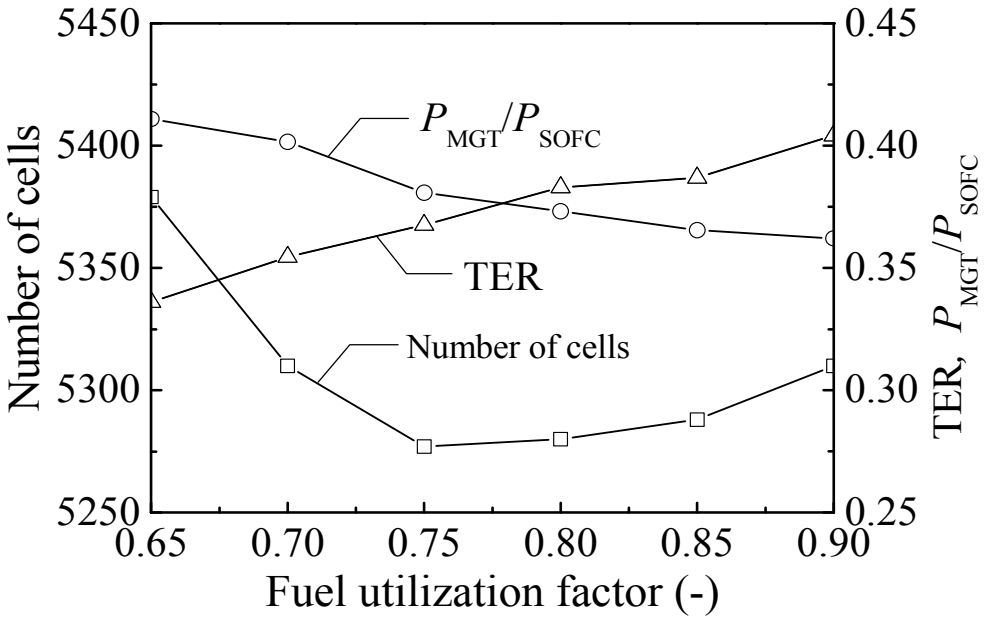

Fig. 6-7: Influence of the fuel utilization factor on P_{MGT}/P_{SOFC}, TER, and the required number of SOFC cells.

6.5.3 Influence of compression ratio and turbine inlet temperature (TIT)

The compression ratio and TIT are key design parameters of an MGT-SOFC hybrid system, because they considerably affect the heat balance between the MGT and SOFC units. In the present study, the compression ratio and TIT were varied from 2 to 12 and 973 to 1273 K, respectively. In Fig. 6-8, the effects of compression ratio and TIT on the CHP energetic efficiency (η_{CHP}) and CHP rational efficiency (ψ_{CHP}) of the system are plotted. It should be noted that when the compression ratio is set at 12 with an input operational U_f of 0.75, TIT exceeds 973 K. Therefore, no data point for this case is shown in the figures. As can be seen in Fig 6-8, at a compression ratio between 2 and 3, the deviation of η_{CHP} was not significant. However, when the ratio was increased from 3 to 12, η_{CHP} decreased linearly. This is because increasing the compression ratio reduces the amount of useful heat available, resulting in a decrease in η_{CHP}. On the other hand, when considering exergy in exhaust gas, ψ_{CHP} increased with an increase in the compression ratio, and the optimum ψ_{CHP} was achieved at a compression ratio in the range of 9 to 11. In addition, increasing TIT considerably improved the η_{CHP} and ψ_{CHP} of the system. This is because the production of byproduct heat is significantly boosted with increasing TIT. However, as TIT increases, more additional fuel is supplied to the

burner, leading to an increase in the system fuel consumption rate. This also results in lower net system electrical efficiency. Indeed, as can be seen in Fig. 6-9, increasing TIT in the present study had a negative impact on system electrical efficiency ($\eta_{ele,sys}$) due to an increase in fuel feed. In addition, increasing the compression ratio from 2 to 12 enhanced $\eta_{ele,sys}$ by approximately 18% (see in Fig. 6-9). The system electrical efficiency increased more rapidly at a low compression ratio. As shown in Fig. 6-10, the TER increased with an increase in TIT, as more useful heat was produced. Nevertheless, the TER decreased with an increase in compression ratio, because the MGT gains efficiency as electricity is generated. Variation in P_{MGT}/P_{SOFC} according to compression ratio and TIT is shown in Fig. 6-11. The P_{MGT}/P_{SOFC} reached a maximum value at a compression ratio between 5 to 10 when TIT ranged from 973 to 1273 K. The maximum value of P_{MGT}/P_{SOFC} shifts toward a higher compression ratio as TIT increases. As can be seen in Fig. 6-12, at lower compression ratios, the required number of SOFC cells decreased significantly and reached a minimum value at a compression ratio in the vicinity of 8. In addition, increasing TIT reduced the required number of SOFC cells. This is mainly because the portion of electrical power generated by MGT increases as TIT increases, leading to a reduction in the required number of SOFC cells.

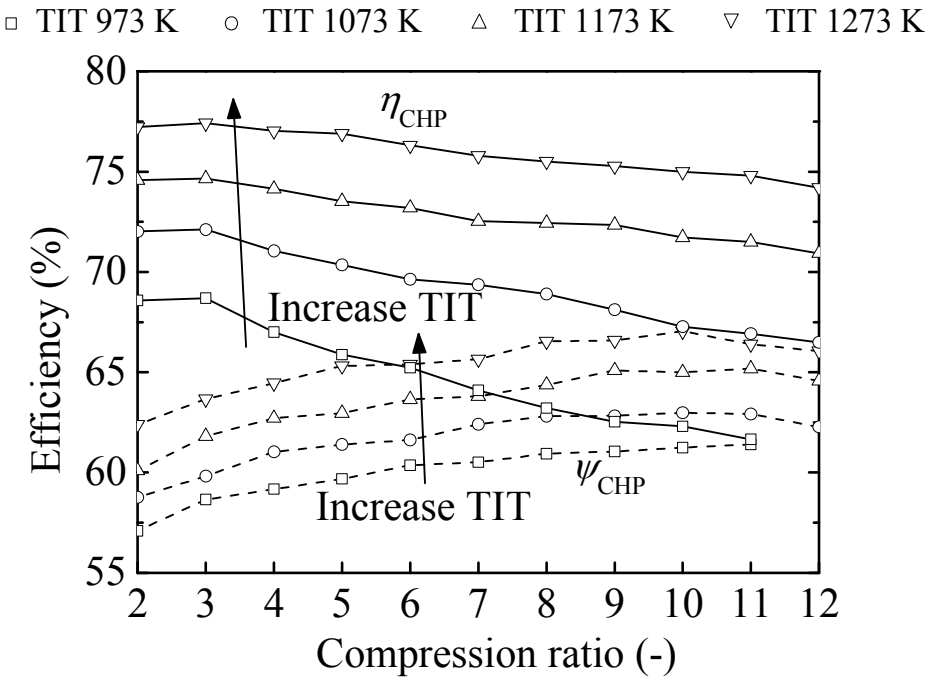

Fig. 6-8: η_{CHP} and ψ_{CHP} versus compression ratio and TER.

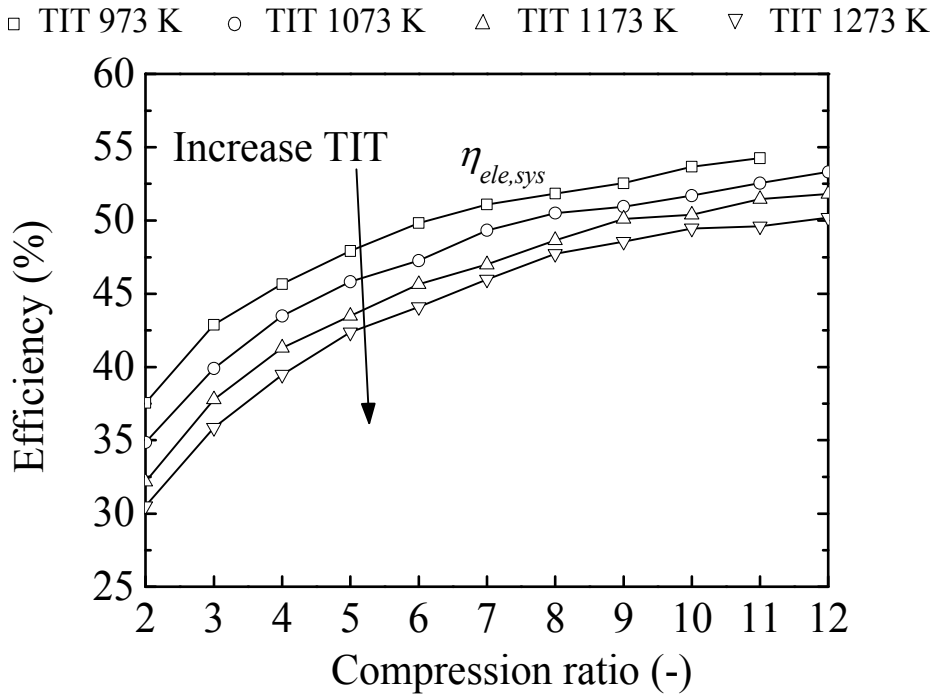

Fig. 6-9: Influence of compression ratio and TIT on system electrical efficiency.

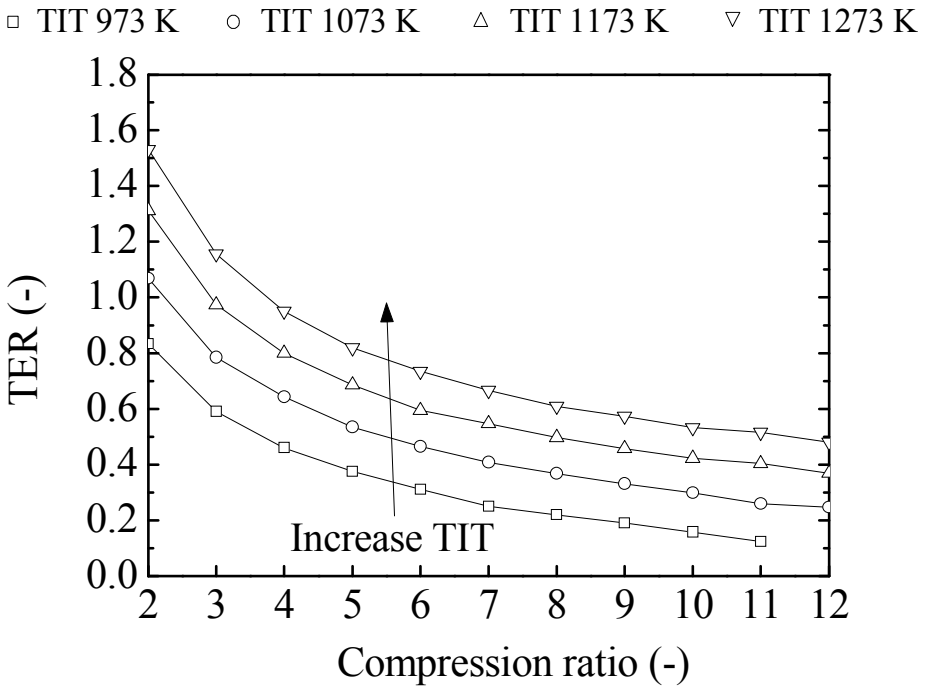

Fig. 6-10: Influence of compression ratio and TIT on TER.

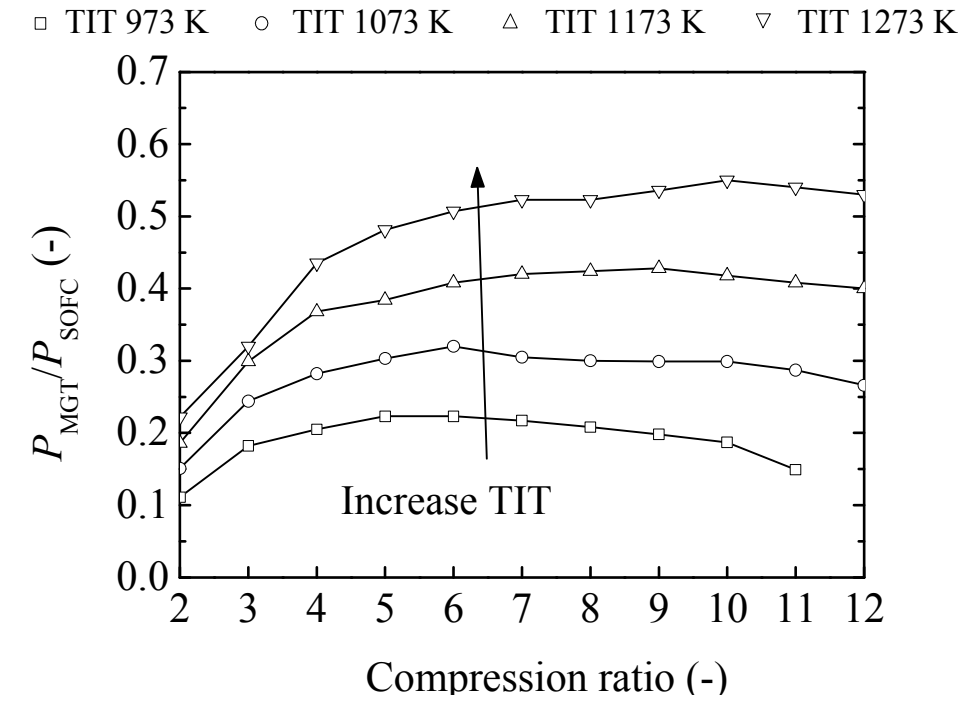

Fig. 6-11: Influence of compression ratio and TIT on P_{MGT}/P_{SOFC}.

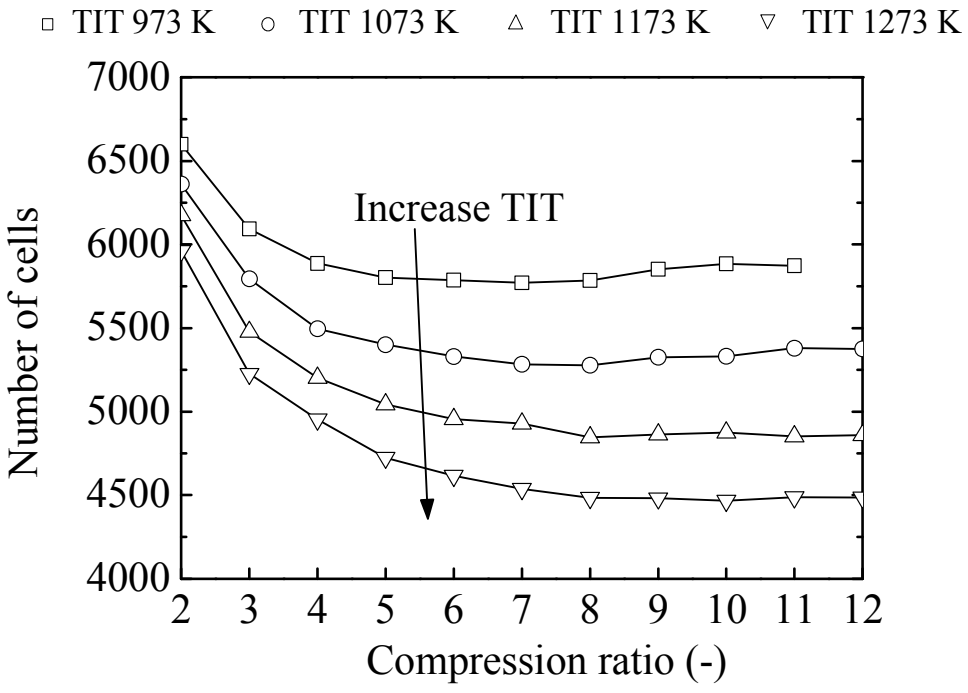

Fig. 6-12: Influence of compression ratio and TIT on the required number of SOFC cells.

6.6 Summary

Performance evaluations of a direct-biogas SOFC-MGT hybrid CHP system were conducted. It is important to closely monitor the operational performance of SOFCs to minimize SOFC degradation due to thermal constraints and carbon deposition on Ni-based anodes. Sensitivity analysis was carried out to investigate the influences of the main variables on the system. The main parameters considered were air-steam mixtures as reforming agents, U_f, TIT, and the compression ratio. Based on the results of our simulations, the following conclusions can be made:

1. Considering individual direct-biogas SOFC operation, as the average cell operating temperature increases as more air is added to the biogas, carbon deposition is less likely to form in the anode channels. Nevertheless, the presence of oxygen has a negative impact on SOFC performance and also causes temperature stress near the stack inlet due to partial oxidation.
2. The addition of a small amount of air to biogas does not have a significant effect on $\eta_{ele,syn}$, η_{CHP}, or ψ_{CHP} of the direct-biogas SOFC in the hybrid CHP system. However, it raises the stack operating temperature and leads to an increase in useful heat output as well as electrical power production by the MGT, which in turn reduces the number of SOFC cells required.
3. In the system studied, the electrical power output produced by the SOFC stack was directly proportional to U_f; however, $\eta_{ele,sys}$ was not significantly affected by variation in U_f. The smallest number of cells was achieved at a U_f of 0.75, whereas the TER increases with an increase in U_f.
4. Increasing the compression ratio improves $\eta_{ele,sys}$ but reduces TER, whereas increasing TIT has the opposite outcomes. However, increasing the compression ratio and TIT has the same influence on ψ_{CHP}, P_{MGT}/P_{SOFC}, and the required number of SOFC cells.

Chapter 7
Conclusions

7.1 Conclusions

The aims of this work were to study a direct internal reforming (DIR) planar solid oxide fuel cell (SOFC), and also to investigate two conceptual SOFC-based plant designs for sustainable power generation by combining the merits of renewable energy and hydrogen energy system. One scenario was an integration of biomass gasification and SOFC, another was an SOFC-micro gas turbine (MGT) system fueled by biogas.

A numerical model was implemented to analyze the thermodynamic performance of a DIR-SOFC. The DIR-SOFC model, validated by comparing with experimental and simulated results in chapter 3, is capable of capturing the detailed distribution of the local temperatures, species concentrations, current density, and polarization losses in streamwise direction. In chapter 4, energy and exergy concepts were used to evaluate the DIR-SOFC performance under co- and counter-flow operations. The study indicates the energetic and rational efficiencies of DIR-SOFC performance under co-flow operation are more sensitive to the increase of current density than that under counter-flow operation. Particular attention was paid to cell temperature profiles to avoid mechanical failure due to high thermal stresses. The result shows that the material constraints need to be considered as well as the energy and rational efficiencies in evaluating the performance of SOFC. With a close attention to material constraints, the preferred flow configuration can be changed depending on the cell geometry and operation conditions.

In chapter 5, the integrated small-scale SOFC-biomass gasification power generation system was investigated. In order to provide insights into the studied system, plant simulation was performed under diverse operating conditions. A DIR-SOFC model under co-flow operation and a thermodynamic equilibrium for biomass gasification

model were developed and verified by reliable experimental and simulation data in chapter 3. The other peripheral components include three gas-to-gas heat exchangers (HXs), heat recovery steam generator (HRSG), burner, fuel and air compressors. To determine safe operating conditions with high system efficiency, energy and exergy analysis was performed to investigate the influence through detailed sensitivity analysis of four key parameters, e.g. steam-to-biomass ratio (STBR), SOFC inlet stream temperatures, SOFC air utilization factor (U_a), SOFC fuel utilization factor (U_f) and anode off-gas recycle ratio (AGR) on system performance. Due to the fact that SOFC stack was accounted for the most expensive part of the initial investment cost, the number of cells required for SOFC stack was economically optimized as well. Through the detailed sensitivity analysis, it shows that the increase of STBR positively affects SOFC while gasifier performance drops. The most preferable operating STBR is 1.5 when the highest system efficiencies and the smallest number of cells. The increase in SOFC inlet temperature shows negative impact on system and gasifier performances while SOFC efficiencies are slightly increased. The number of cells required for SOFC is reduced with the increase of SOFC inlet temperature. The system performance is optimized for U_f of 0.75 while SOFC and system efficiencies are the highest with the smallest number of cells. The result also shows the optimal anode off-gas recycle ratio of 0.6. Regarding with the increase of AGR, there is a trade-off between overall efficiencies and the number of SOFC cells.

In chapter 6, the SOFC-micro gas turbine (MGT) system scenario shows great potential as a decentralized combined heat and power (CHP) system. To evaluate the potential use of biogas as the main source of energy for a direct-biogas SOFC-MGT hybrid CHP system, a sensitivity analysis was conducted under diverse operating conditions to investigate the influence of key operating parameters of the hybrid CHP system with the consideration of operational constraints. The key parameters in this study were SOFC reforming agent, U_f, turbine inlet temperature (TIT), and compression ratio. The influence of variation in operating parameters on plant performance was evaluated for the overall system and SOFC efficiencies as well as the thermal energy to electric power ratio (TER), the power ratio of MGT to SOFC (P_{MGT}/P_{SOFC}), and the size of the SOFC stack. As a reforming agent for direct-biogas SOFC, steam is more preferable than a traditional air-steam mixture in terms of material limitations and SOFC efficiencies; however, an air-steam mixture with a small amount of air boosts the useful heat output and electricity generated by an MGT without significantly affecting overall system efficiency. The increase in U_f improves the electrical power output produced by the

SOFC stack, but also requires more fuel to be fed to the burner, resulting in an increase in useful heat energy. Increasing the compression ratio improves the system's electrical efficiency but lowers useful heat generation; nevertheless, increasing TIT decreases the system's electrical efficiency but improves the efficiency of the CHP system. To achieve the optimum operating conditions of the hybrid CHP system, the operating parameters should be determined based on the desired energy outcomes.

7.2 Suggestions for the future works

As demand grows for more environmentally conscious energy systems, SOFC-based systems will increasingly be called upon to deliver on this promise. The models developed in this study provide tools in developing better control methods and refining hybrid design. In turn, this work can assist fuel cell developers in creating viable hybrid power generation systems, leading to their commercialization and acceptance as reliable suppliers of efficient electrical power. This study of SOFC can be expanded upon in many ways. In this study, the control volume was selected as the repeat element in the center channel of the center cell of the SOFC stack with adiabatic boundary conditions. It was assumed that all the cells in the stack have the same characteristics. The model can be further improved considering the heat interactions between the adjacent cells in stack level. One of more beneficial directions to which this work could lead would be the study of SOFC degradation.

For future work, it is also suggested that the presented model can lead to further enhancement of the SOFC model to investigate the dynamic response of the start-up, load change or shut-down behaviors, important issues when comparing performance. The SOFC-based system study in this work can also be utilized in dynamic studies. An extension of the present work could include operation over a larger load range as well as load change between part-load operation points.

Another key area in which this work can be expanded is model refinement of the key system components, MGT and gasifier. This work used a zero-dimensional gasifier, whereas a specific type of gasifier could be used to which a zonal analysis could be applied. In this way a higher efficient and more accurate model of a gasifier could be developed, and the most inefficient zones of the gasifier could be determined. In the study of SOFC-MGT hybrid system, two-shaft turbines can be included for more reliability in an extended analysis.

References

[1] International Energy Agency, Renewables in Global Energy Supply: An IEA Fact Sheet, OECD (2007).

[2] C.P. Mitchell, A.V. Bridgwater, D.J. Stevens, A.J. Toft, M.P. Watters, "Technoeconomic assessment of biomass to energy" , Biomass and Bioenergy 9 (1995) 205-226.

[3] J.J. Stevens, "Review and analysis of the 1980-1989 biomass thermochemical conversion program.", NREL/TP-421-7501, US (1989).

[4] C. Stiller, B.Thorud, S. Seljebø, Ø. Mathisen and H. Karoliussen, "Finite-volume modeling and hybrid-cycle performance of planar and turbular solid oxide fuel cells", Journal of Power Sources 141 (2005) 227-240.

[5] B. Zhu, X.Y. Bai, G.X. Chen, W.M. Yi and M. Bursell, "Fundamental study on biomass-fuelled ceramic fuel cell", International Journal of Energy Research 26 (2002) 57-66.

[6] S. Baron, N. Brandon, A. Atkinson, B. Steele, and R. Rudkin, "The impact of wood-derived gasification gases on Ni–CGO anodes in intermediate temperature solid oxide fuel cells", Journal of Power Sources 126 (2004) 58-66.

[7] P.V. Aravind, J.P. Ouweltjes, E. de Heer, N. Woudstra, and G. Rietveld, "Impact of Biomass-Derived Contaminants on SOFCs with Ni/Gadolinia-Doped Ceria Anodes." Electrochemical and Solid-State Letters 11 (2) (2008) B24-28.

[8] J. Mermelstein, M. Millan, and N. Brandon, "The impact of steam and current density on carbon formation from biomass gasification tar on Ni/YSZ, and Ni/CGO solid oxide fuel cell anodes", Journal Power Sources 195 (2010) 1657-1666.

[9] J. Staniforth, K. Kendall, "Cannock landfill gas powering a small tubular solid oxide fuel cell – a case study", Journal Power Sources 86 (2000) 401–403.

[10] Y. Shiratori, T. Oshima, K. Sasaki, "Feasibility of direct-biogas SOFC", International Journal of Hydrogen Energy 33 (2008) 6316–6321.

[11] K. Girona, J. Laurencin, M. Petitjean, J. Fouletier, F. Lefebvre-Joud, "SOFC running on biogas: identification and experimental validation of "safe" operating conditions", ECS Transactions 25 (2) (2009) 1041–1050.

[12] A. Lanzini, P. Leone, "Experimental investigation of direct internal reforming of biogas in solid oxide fuel cells", International Journal of Hydrogen Energy

35 (2010) 2463–2476.

[13] P. Leone, A. Lanzini, M. Santarelli, M. Cali, F. Sagnelli, A. Boulanger, A. Scaletta, P. Zitella, “Methane-free biogas for direct feeding of solid oxide fuel cells”, Journal of Power Sources 195 (2010) 239–248.

[14] Y. Shiratori, T. Ijichi, T. Oshima, K. Sasaki, “Internal reforming SOFC running on biogas”, International Journal of Hydrogen Energy 35 (2010) 7905-7912.

[15] J.H. Hirschenhofer, D.B. Stauffer, R.R. Englemen, and M.G. Klett, “Fuel Cell Handbook”, Forth edition (1998).

[16] S.E. Veyo, L.A. Shockling, J.T. Dederer, J.E. Gillett, W.L. Lundberg. “Tubular solid oxide fuel cell/gas turbine hybrid cycle power systems: Status”, Journal of Engineering for Gas Turbines and Power 124 (2002) 845-849.

[17] S.E. Veyo, S.D. Vora, K.P. Litzinger, W.L. Lundberg, “Status of pressurized SOFC/GAS turbine power system development at Siemens Westinghouse”, In Proceedings of the ASME Turbo Expo, Amsterdam, Netherlands (2002).

[18] K.P. Litzinger, “Comparative evaluation of SOFC gas turbine hybrid options” In Proceedings of the ASME Turbo Expo Conference, Reno, NV, USA (2005).

[19] D.G.D. Agnew, “The design and integration of the rolls royce fuel cell systems 1MW SOFC”, In Proceedings of the ASME Turbo Expo Conference, Reno, NV, USA (2005).

[20] A. Traverso, M. Pascenti, M.L. Ferrari, R. Bertone, L. Magistri, “Hyrbid simulation facility based on commercial 100 kWe micro gas turbine”, In Proceedings of the ASME Fuel Cell Conference, Irvine, CA, USA (2007).

[21] http://www.mhi.co.jp/en/news/sec1/200608041128.html (May 1,2008).

[22] R. Desrosiers, “Thermodynamics of gas-char reactions”, T.B. Reed editor, A survey of biomass gasification, Solar Energy Research Institute, Colorado, USA (1979).

[23] S.V. Loo, J. Koppejan, “The handbook of biomass combustion and co-firing”, Earthscan, London (2008).

[24] S. Yokoyama, “The Asian Biomass Handbook: A guide for biomass production and utilization.” , The Japan Institute of Energy,. Tokyo, Japan (2008)

[25] J.G. Brammer, A.V. Bridgwater, “Drying technologies for an integrated gasification bio-energy plant”, Renewable and Sustainable Energy Reviews 3 (4) (1999) 243-289.

[26] A.V. Bridgwater, “Renewable fuels and chemicals by thermal processing of biomass”, Chemical Engineering Journal 91 (2003) 87-102.

[27] R.L. Bain, “Biomass gasification overview”, Technical report, National Renewable Energy Laboratory, US Department of Energy (2004).

[28] D.J Stevens, “Hot gas conditioning: Recent progress with larger-scale biomass gasification systems”, NREL-SR-510-29952, National Renewable Research Laboratory, Golden, CO, USA (2001).

[29] M.M.G. Cuenca, “Novel Anode Materials For Solid Oxide Fuel Cells”, Ph.D. dissertation, University of Twente, Enschede, Netherlands (2002)

[30] S.C. Singhal and K. Kendall, “High Temperature Solid Oxide Fuel Cells: Fundamentals, Design and Applications”, Elsevier, Oxford (2003).

[31] J.W. Fergus, “Lanthanum chromite-based materials for solid oxide fuel cell interconnects”, Solid State Ionics 171 (2004) 1–15.

[32] W. Lehnert, J. Meusinger, and F. Thom, “Modelling of gas transport phenomena in SOFC anodes”, Journal of Power Sources 87 (2000) 57-63.

[33] R.A. Gaggioli and P.J. Petit, “Use the second law, first”. Chemtech 7 (1977) 496-506.

[34] M.A. Khaleel, Z. Lin, P. Singh, W. Surdoval, and D. Collin, “A finite element analysis modeling tool for solid oxide fuel cell development: coupled electrochemistry, thermal and flow analysis in MARC®”, Journal of Power Sources 130 (2004) 136-148.

[35] T. Hibino, S. Wang, S. Kakimoto, M. Sano, “Single Chamber Solid Oxide Fuel Cell Constructed from an Yttria-Stabilized Zirconia Electrolyte ”, Electrochemical and Solid-State Letters 2 (7) (1999) 317–319.

[36] T. Hibino, A. Hashimoto, T. Inoue, J. Tokuno, S. Yoshida, M. Sano, “Single-chamber solid oxide fuel cells at intermediate temperatures with various hydrocarbon-air mixtures”, Journal of the Electrochemical Society 147 (2000) 2888–2892.

[37] B.E. Buergler, A.N. Grundy, L.J. Gauckler, “Thermodynamic equilibrium of single-chamber SOFC relevant methane-air mixtures”, Journal of the Electrochemical Society 153 (2006) A1378–A1385.

[38] C.R.H. de Smet, M.H.J.M. de Croon, R.J. Berger, G.B. Marin, and J.C. Schouten, “Design of adiabatic fixed-bed reactors for the partial oxidation of methane to synthesis gas: Application to production of methanol and hydrogen-for-fuel cells”, Chemical Engineering Science 56 (2001) 4849-4861.

[39] E. Achenbach, “Three-dimensional and time-dependent simulation of a planar solid oxide fuel cell stack”, Journal of Power Sources 49 (1994) 333-348

[40] M.V. Twigg, “Catalyst handbook”, second edition, Wolfe Publishing Ltd., London (1989).

[41] R.H. Perry, “Perry’s chemical engineers’ handbook”, seventh edition, McGraw-Hill, New York (1997).

[42] C.R. Wilke, “Diffusional Properties of Multicomponent Gases”, Chemical Engineering Progress 46 (1950) 95-104.

[43] F. Zhao and A.V. Virkar, “Dependence of polarization in anode-supported solid oxide fuel cells on various cell parameters”, Journal of Power Sources 141 (1) (2005) 79–95.

[44] P. Aguiar, C.S. Adjiman, and N.P. Brandon, “Anode-supported intermediate temperature direct internal reforming solid oxide fuel cell. I: model-based steady-state performance”, Journal of Power Sources 138 (2004) 120-136.

[45] B.A. Haberman and J.B. Young, “A detailed three-dimensional simulation of an IP-SOFC stack”, Transactions of the ASME Journal of Engineering for Gas Turbines and Power 127 (2008) 109-120.

[46] K.D. Panopoulos, L. Fryda, J. Karl, S. Poulou, and E. Kakaras, “High temperature solid oxide fuel cell intregrated with novel allothermal biomass gasification Part I: Modelling and feasibility study”, Journal of Power Sources 159 (2006) 570-585.

[47] N. Bessette, “Modeling and simulation for solid oxide fuel cell power systems”, Ph.D. dissertation, Georgia Institute of Technology, U.S. (1994).

[48] K.J. Daun, S.B. Beale, F. Liu, and G.J. Smallwood, “Radiation Heat Transfer in. Planar SOFC Electrolytes”, Journal of Power Sources 157 (2006) 302–310.

[49] D.L. Damm and A.G. Federov, “Radiation heat transfer in SOFC materials and components”, Journal of Power Sources 143 (2005) 158–165.

[50] D.L. Damm and A.G. Federov, “Spectral radiative heat transfer analysis of the planar SOFC”, Journal of Fuel Cell Science and Technology 4 (2005) 258–262.

[51] J.D.J. VanderSteen and J.G. Pharoah, “Modeling Radiation Heat Transfer with Participating Media in Solid Oxide Fuel Cells”, Journal of Fuel Cell Science and Technology 3 (2006) 62–67.

[52] F.P. Incropera and D.P. Dewitt, “Fundamentals of Heat and Mass Transfer”, fifth edition, John Wiley & Son, New York (2002)

[53] S. Nagata, A. Momma, T. Kato, Y. Kasuga, “Numerical analysis of output characteristics of tubular SOFC with internal reformer”, Journal of Power Sources 101 (2001) 60–71.

[54] T.X. Ho, P. Kosinski, A.C. Hoffmann and Vik A., “Numerical analysis of a planar anode-supported SOFC with composite electrodes”, International Journal of Hydrogen Energy 34 (8) (2009) 3488–3499.

[55] F. Zhao and A.V. Virkar, “Dependence of polarization in anode-supported solid oxide fuel cells on various cell parameters”, Journal of Power Sources 141 (1) (2005) 79–95.

[56] J. Herguido, J. Corella, and J. Gonzalez-Saiz, “Steam gasification of lignocellulosic residues in a fluidized bed at a small pilot scale. Effect of the type of feedstock”, Industrial & Engineering Chemistry Research 31 (1992) 1274-1282.

[57] S. Jarungthammachote and A. Dutta, “Thermodynamic equilibrium model and second law analysis of a downdraft waste gasifier”, Energy 32 (2007) 1660-1669.

[58] A. Melgar, J. F. Pérez, H. Laget, A. Horrillo., “Thermochemical equilibrium modelling of a gasifying process”, Energy Conversion and Management 48 (2007) 59-67.

[59] C.R. Altafini, P.R. Wander and R.M. Barreto, “Prediction of the working parameters of a wood waste gasifier through an equilibrium model”, Energy Conversion and Management 44 (2003) 2763-2777.

[60] Z.A. Zainal, R. Ali, C.H. Lean and K.N. Seetharamu, “Prediction of performance of a downdraft gasifier using equilibrium modeling for different biomass materials”, Energy Conversion and Management 42 (2001) 1499-1515.

[61] C. Cunnel, M.G. Pangalis, R.F. Martinez-Botas, “Integration of solid-oxide fuel-cells into gas-turbine power generation cycles, part 2: hybrid model for various integration schemes”, Proceedings of the Institution of Mechanical Engineers, Part A: Journal of Power and Energy 216 (2002) 145–154.

[62] Kays, W.M. and London, A.L., “Compact Heat Exchangers”, third edition, McGraw-Hill Book Company, New York (1984)

[63] T.J Kotas, “The Exergy Method of Thermal Plant Analysis”, second edition, Krieger Publishing Company, Florida (1995).

[64] E. Achenbach, “SOFC stack modeling, final report of Activity A2, Annex II: Modeling and evaluation of advanced solid oxide fuel cell”, IEA report, International Energy Agency, Germany (1996).

[65] S. Wongchanapai, H. Iwai, M. Saito and H. Yoshida, Selection of suitable operating conditions for Planar Anode-supported Direct-internal-reforming Solid-Oxide Fuel Cell. J. Power Sources 204(2012), pp 14–24.

[66] R.J. Braun, “Optimal Design and Operation of Solid Oxide Fuel Cell Systems for Small-scale Stationary Applications”, Ph.D. dissertation, University of Wisconsin-Madison, U.S. (2002).

Nomenclature

A	cell active area, m^2
A_c	cross section area, m^2
AGR	anode off-gas recycle ratio
C	heat capacity, kW K^{-1}
C_P	specific heat at constant pressure, kJ $kg^{-1}K^{-1}$
d	diameter
D_i	diffusivities of the gas species i
E	activation energy, kJ $kmol^{-1}$
ex	specific exergy flow, kJ kg^{-1}
Ex	exergy flow rate, kW
ER	equivalence ratio
F	faraday constant, 96487 C mol^{-1}
h	convective heat transfer coefficient, W $m^{-2}K^{-1}$
HRSG	heat recovery steam generator
HX	heat exchanger
I	current, A
i_c	current density, A m^{-2}
K	equilibrium constants
K_i^{OX}	adsorption constant for component i in combustion reaction
k_{shift}	rate constant of forward shift reaction, mol $m^{-3}Pa^{-2}s^{-1}$
HHV	higher heating value, MJ Nm^{-3}
LHV	lower heating value, MJ Nm^{-3}
M_i	molecular weight of species i, kg mol^{-1}
m	mass flow rate, kg s^{-1}
n_e	number of electrons participating in the electrochemical reaction
n_i	molar flow rate of gas species i, kmol s^{-1}
P	electrical power, kW
P	total pressure, kPa
p_i	partial pressure of gas species i, kPa
Q	heat transfer rate, kW
R	universal gas constant, 8.31434 J mol^{-1} K^{-1}
r	reaction rate, kmol s^{-1}
STBR	steam to biomass ratio

T	temperature, K
TER	thermal energy to electric power ratio
TIT	turbine inlet temperature, K
U_a	air utilization factor
U_f	fuel utilization factor
V	voltage, V
x_i	molar fraction of gas species *i*

Greek letters

ΔG^0	change of standard Gibbs free energy, kJ mol^{-1}
ΔH	enthalpy change, kJ mol^{-1}
η	energetic efficiency
η_{cg}	cold gas efficiency
γ	specific heat ratio
λ	heat conduction coefficient, W $m^{-1}K^{-1}$
ρ	density, kg m^{-3}
ρ	specific electrical resistance, Ω m
ψ	rational efficiency

Subscripts

0	properties of the environment
act	activation polarization
air	air, air channel
an	anode
c, C	compressor
cat	cathode
ch	chemical
CHP	combined heat and power overall system
conc	concentration polarization
co	co-flow cell configuration
ct	counter -flow cell configuration
ele	electrical
FOX	methane full oxidation
fuel	gas mixture at the fuel channel, fuel channel

in	inlet value
inv	inverter
MGT	micro gas turbine
OC	open-circuit
ohm	ohmic polarization
out	outlet value
ph	physical
react	anode reaction
shift	shift reaction
SOFC	solid oxide fuel cell stack
solid	SOFC cell
SR	steam reforming
syn	synthesis gas
sys	overall system
t, T	turbine
TPB	three phase boundary at the anode–electrolyte interface